SYNTHESIS OF HIGHLY FLUORESCENT N,S CO-DOPED CARBON QUANTUM DOTS AND THEIR APPLICATION IN FLUOROMETRIC DETECTION OF G-QUADRUPLEX FORMING HER2 PROMOTER REGION

A THESIS SUBMITTED TO
THE GRADUATE SCHOOL OF NATURAL AND APPLIED SCIENCES
OF
MIDDLE EAST TECHNICAL UNIVERSITY

BY

ZEYNEP İREM BULUT

IN PARTIAL FULFILLMENT OF THE REQUIREMENTS
FOR
THE DEGREE OF MASTER OF SCIENCE
IN
CHEMISTRY

AUGUST 2022

Approval of the thesis:

SYNTHESIS OF HIGHLY FLUORESCENT N,S CO-DOPED CARBON QUANTUM DOTS AND THEIR APPLICATION IN FLUOROMETRIC DETECTION OF G-QUADRUPLEX FORMING HER2 PROMOTER REGION

submitted by **ZEYNEP İREM BULUT** in partial fulfillment of the requirements for the degree of **Master of Science** i**n Chemistry, Middle East Technical University** by,

Prof. Dr. Halil Kalıpçılar
Dean, Graduate School of **Natural and Applied Sciences** _____

Prof. Dr. Özdemir Doğan
Head of the Department, **Chemistry** _____

Assoc. Prof. Dr. Özgül Persil Çetinkol
Supervisor, **Chemistry, METU** _____

Examining Committee Members:

Prof. Dr. Ayşen Yılmaz
Chemistry, METU _____

Assoc. Prof. Dr. Özgül Persil Çetinkol
Chemistry, METU _____

Assist. Prof. Dr. Demet Asil Alptekin
Chemistry, METU _____

Assoc. Prof. Dr. Görkem Günbaş
Chemistry, METU _____

Assoc. Prof. Dr. Sevinç Kurbanoğlu
Faculty of Pharmacy, Ankara University _____

Date: 31.08.2022

I hereby declare that all information in this document has been obtained and presented in accordance with academic rules and ethical conduct. I also declare that, as required by these rules and conduct, I have fully cited and referenced all material and results that are not original to this work.

Name Last name : Zeynep İrem Bulut

Signature :

ABSTRACT

SYNTHESIS OF HIGHLY FLUORESCENT N, S CO-DOPED CARBON QUANTUM DOTS AND THEIR APPLICATION IN FLUOROMETRIC DETECTION OF G-QUADRUPLEX FORMING HER2 PROMOTER REGION

Bulut, Zeynep İrem
Master of Science, Chemistry
Supervisor: Assoc. Prof. Dr. Özgül Persil Çetinkol

August 2022, 117 pages

The human epidermal growth factor receptor 2 (HER2) is a member of HER family which are known to be involved in cell development and differentiation. The overexpression of HER2 is linked to aggressive forms of breast cancer. It has been reported that the formation of a stable parallel G-quadruplex (G4) in the HER2 promoter region was playing a role in the regulation of HER2 expression in MCF-7 cells. Consequently, we hypothesized that the detection of HER2 G4 structure could be used in investigating HER2 expression. Within this thesis, first Nitrogen and Sulfur Co-doped carbon quantum dots (N,S-CQDs) were synthesized using citric acid and L-cysteine and characterized by TEM, DLS, XRD and XPS. Next, fluorescent Thioflavin T (ThT) dye was used as the quencher of N,S-CQDs and N,S-CQDs/ThT mixture was used as a probe to detect HER2 G4 structure. The developed probe was found to exhibit a remarkable sensitivity towards HER2 G4 with LOD of 0.22 μM, and LDR of 0.27 μM to 6.0 μM. The probe was also selective towards HER2 G4 among other single-stranded (Poly A, dA_{32}, dT_{32}), double-stranded ($dA_{32}dT_{32}$), and G4 structures (RB, Pu22, C-MYC, VEGF, BCL-2, and K-RAS) under the optimized conditions. The structure of HER2 G4 and its interactions with N,S-CQDs and ThT were further characterized via Circular Dichroism spectroscopy.

To the best of our knowledge, this is the first platform developed for HER2 G4 detection, and we believe it could open up new avenues in fast and routine detection of HER2 G4 structure.

Keywords: Carbon dots, Thioflavin T, Optical properties, Fluorescence detection, HER2 G-quadruplex.

ÖZ

YÜKSEK FLUORSANLI N,S ORTAK KATKILI KARBON KUANTUM NOKTALARININ SENTEZİ VE G-DÖRTLÜ YAPISI OLUŞTURAN HER2 PROMOTER BÖLGESİNİN FLOROMETRİK TESPİTİNDE UYGULAMASI

Bulut, Zeynep İrem
Yüksek Lisans, Kimya
Tez Yöneticisi: Doç. Dr. Özgül Persil Çetinkol

Ağustos 2022, 117 sayfa

İnsan epidermal büyüme faktörü reseptörü 2 (HER2), hücre gelişimi ve farklılaşmasında yer aldığı bilinen HER ailesinin bir üyesidir. HER2 geninin yüksek düzeyde ekspresyonu özellikle agresif meme kanseri formlarıyla bağlantılıdır. HER2 promotör bölgesinin stabil G-dörtlü (G4) yapısı oluşturduğu ve de HER2 ekspresyonunun düzenlenmesinde rol oynadığı MCF-7 hücreleri kullanılarak kanıtlanmıştır. Bu kapsamda, HER2 G4 yapısının tespitinin HER2 ekspresyonunun anlaşılmasında kullanılabileceği tezi ortaya çıkmıştır. Bu tez kapsamında sitrik asit ve L-sistein kullanılarak Azot ve Kükürt ortak katkılı karbon kuantum noktaları (N,S-CQD'ler) sentezlenmiş ve TEM, DLS, XRD ve XPS yöntemleri ile karakterize edilmiştir. Floresan boya olan Thioflavin T (ThT), N,S-CQD'lerin emisyonunu azaltmak için, N,S-CQD/ThT karışımı ise HER2 G4 yapısını tespit etmek için kullanılmıştır. Önerilen sensör platformunun HER2 G4 yapısına karşı yüksek hassasiyet sergilediği, tespit sınırının 0.22 μM ve lineer dinamik aralığının 0.27 μM ile 6.0 μM olduğu belirlenmiştir. Ayrıca, geliştirilen platformun, optimize edilmiş koşullar altında, diğer tek sarmallı (Poli A, dA_{32}, dT_{32}), çift sarmallı ($dA_{32}dT_{32}$) ve G4 yapıları (RB, Pu22, C-MYC, VEGF, BCL-2 ve K-RAS) arasında HER2 G4'e karşı yüksek seçicilik gösterdiği tespit edilmiştir. HER2 G4'ün yapısı, N,S-CQDs ve ThT ile etkileşimleri dairesel dikroizm spektoskopi ile karakterize edilmiştir.

Bildiğimiz kadarıyla geliştirdiğimiz platform HER2 G4 tespiti için geliştirilmiş ilk platformdur ve HER2 G4 yapısının hızlı ve rutin ve tespitinde kullanılabileceğini düşünüyoruz.

Anahtar Kelimeler: Karbon Kuantum Noktaları, Thioflavin T, Optik Özellikler, Floresans Tespit Platformu, HER2 G-dörtlüsü.

To my loved ones…

ACKNOWLEDGMENTS

Firstly, I would like to express my sincere thanks to my supervisor, Assoc. Prof. Dr. Özgül Persil Çetinkol for the opportunity to work with her and further gratitude for her continuous support, motivation, patience, knowledge, and attention to details.

I would also like to express my sincere thanks to Dr. Mehrdad Forough for that friendly and warm work environment, continuous support, patience, understanding, and helping me with this project.

I also would like to thank my friend Selin Küçükerenköy for her vital support and encouragement. Without her help, it would not have been possible to complete this project properly.

Besides, I would like to express my gratitude to my parents for their unlimited support, for believing in me, and for encouraging me to achieve all my goals.

I would like to thank my committee members, Prof. Dr. Ayşen Yılmaz, Assist. Prof. Dr. Demet Asil Alptekin, Assoc. Prof. Dr. Görkem Günbaş, and Assoc. Prof. Dr. Sevinç Kurbanoğlu for their valuable presence at my thesis defense.

I would like to thank Prof. Dr. Ayşen Yılmaz and her research group for letting us to use their infrastructure during the synthesis of N,S-CQDs and Assoc. Prof. Dr. Salih Özçubukçu and his research group for letting us to use their freeze-drying instrument during the purification of the synthesized N,S-CQDs.

I would like to thank METU Central Laboratory for their TEM and XPS analyses.

Finally, my gratitude goes to the Department of Chemistry and staff members for the infrastructure, giving me the opportunity to conduct research and their kind support during the project.

TABLE OF CONTENTS

ABSTRACT v

ÖZ vii

ACKNOWLEDGMENTS x

TABLE OF CONTENTS xi

LIST OF TABLES xiv

LIST OF FIGURES xv

LIST OF SCHEMES xix

LIST OF ABBREVIATIONS xx

CHAPTERS

1 INTRODUCTION 1

1.1 Nanotechnology 1

1.2 Nanostructures 2

1.2.1 Semiconductor Nanostructure 3

1.2.2 Quantum Dots 4

1.3 Applications of Carbon Quantum Dots 13

1.3.1 Use of CQDs in Bioimaging 14

1.3.2 Use of CQDs in Drug Delivery 15

1.3.3 Use of CQDs in Photocatalytic Applications 16

1.3.4 Use of CQDs in Electrocatalysis Applications 16

1.3.5 Use of CQDs in Energy Storage Applications 17

1.3.6 Use of CQDs in Chemical Sensing 18

1.4 Human Epidermal Growth Factor Receptor (HER2) 19

1.5 Nucleic Acid Detection 23

1.6 HER2 Detection Techniques 30
1.7 Aim of the Study 36
2 MATERIALS AND METHODS 39
2.1 Materials and Chemicals 39
2.2 Instrumentation 41
2.3 Synthesis of N, S-CQDs 42
2.4 Preparation of the Probe and Analyte 43
2.5 Optimization Studies 44
3 RESULTS AND DISCUSSION 47
3.1 Characterizations of N,S-CQDs 47
3.2 Quantum Yield Measurements of Synthesized N, S-CQDs 50
3.3 Fluorometric Detection of HER2 G-Quadruplex Using Conjugated N,S-CQDs and Probe 52
3.4 Optimization of N,S-CQDs Concentration 55
3.4.1 Optimization of ThT Concentration 58
3.4.2 pH optimization of the Probe 61
3.4.3 Response Time of the Proposed Probe to HER2 G-Quadruplex 62
3.4.4 The Effect of Temperature 64
3.4.5 The Selectivity of the Proposed Probe 67
3.4.6 The Sensitivity of the Proposed Probe 69
3.4.7 Characterization of the Proposed Platform via Circular Dichroism (CD) Spectroscopy 71
3.4.8 Characterization of Proposed System 72
3.4.9 Possible Sensing Mechanism 73
4 CONCLUSION 75

REFERENCES 77

A. Preparation of Buffer and Stock Solutions 107

B. DLS Experimet Analysis Report 111

C. Quantum Yield Experiments.....112

D. Fluorometry Experiments 114

LIST OF TABLES

TABLES

Table 1. Summary of previously reported methods for the detection of various HER2. 32
Table 2. The used chemicals/materials and reagents..... 39
Table 3. The sequences of oligonucleotides, examined in this study..... 40
Table 4. Particle size analysis results for the synthesized N,S-CQDs. “d” represents particle distribution %. 111

LIST OF FIGURES

FIGURES

Figure 1. The electronic band structure of insulators, semiconductors, and conductors (metals). 3
Figure 2. Schematic representation of core/shell structure of QDs. 5
Figure 3. Schematic representation of the classification of carbon-based quantum dots: GQDs, CQDs, and CNDs 6
Figure 4. Schematic representation of the chemical structure of CQDs. 8
Figure 5. Schematic representation of the experimental setup and apparatus for the synthesis of CQDs by using "Top-down" and "Bottom-up" synthesis strategies... 13
Figure 6. HER2 extracellular domain where colored sections represent subdomains 20
Figure 7. Representation of side view of HER2 G-quadruplex structure. 23
Figure 8. Particle size distribution measurement of synthesized N,S-CQDs..... 48
Figure 9. XRD analysis of synthesized N,S-CQDs 48
Figure 10. (a) XPS and (b) high-resolution XPS analysis of synthesized N,S-CQDs. 49
Figure 11. HR-TEM micrographs of the synthesized N,S-CQDs (a and b at different magnifications. 50
Figure 12. Fluorescence intensity spectra of N,S-CQDs excited at varying excitation wavelengths. 51
Figure 13. Integrated fluorescence intensity vs. Absorbance graph of standard sample and N,S-CQDs. The lines equations were calculated as y = 9441.4x - 6020.1 and y = 6118.4x - 6258.3 for standard sample and N,S-CQDs, respectively. 52
Figure 14. (a) Step-by step fluorescence response of the developed probe towards the target analyte (HER2 G4): black and gray traces represent 2.5 ppm N,S-CQDs and the same sample upon addition of ThT, respectively under the optimized conditions (40.98 μM), recorded after 5-minutes of mixing. The red trace represents the developed probe 1-minute after the addition of the target analyte, HER2 G4, at the optimized conditions. The corresponding step-by-step digital photographs of the

probe captured under day light (b) and UV illumination at 365 nm (c) upon addition of the sensing ingredients under the optimized conditions at room temperature. Cuvettes from 1 to 6 contains N,S-CQDs, N,S-CQDs/ThT, N,S-CQDs/ThT/HER2, N,S-CQDs, N,S-CQDs/ThT, N,S-CQDs/ThT/HER2, respectively. 55
Figure 15. Fluorescence spectra of 2500 µL (a) 2.5 ppm N, S-CQDs (b) 5.0 ppm N, S-CQDs (c) 10.0 ppm N, S-CQDs upon the titration with the increasing volumes of ThT under ambient temperature after 5 minutes of mixing. 57
Figure 16. Fluorescence spectra of 2.5 ppm 2500 µL of N,S-CQDs titrated with varying concentrations of ThT (a) 500 µM (b) 1000 µM and (c) 4000 µM under ambient temperature, after 5 minutes of mixing. 60
Figure 17. Modified Stern-Volmer plot of $F_0/(F_0-F)$ vs. 1/[Q]. The error bars indicate SD (n=3). 61
Figure 18. Fluorescence emission spectra of 2.5 ppm N, S-CQD solution at different pH values in the absence and presence of 500 µM 250.0 µL ThT. Under ambient temperature after 5 minute mixing. 62
Figure 19. Fluorescence spectra of N,S-CQDs (2.5 ppm, black spectrum), 2.5 ppm N,S-CQDs/ThT (final concentration 40.98 µM, gray spectrum) and N,S-CQDs/ThT probe after the addition of HER2 G4 stock solution (75 µM) at 1, 3, 5, 10, 15, 20, 30, 45 (orange spectra), and 60 minutes (red spectrum). The inset represents the corresponding plot of $F_1/(F_0-F_2)$ vs. time (min). Under ambient temperature without mixing. The error bars indicate SD (n=3). 63
Figure 20. The effect of temperature on the response of the probe upon the addition of HER2 G4 under the optimized conditions at (a) 406 nm and (b) 494 nm. The error bars indicate the SD (n=3). 66
Figure 21. Selectivity studies for the N,S-CQDs/ThT probe based on addition of 300 µL of 100 µM of each nucleic acid structure except HER2 (1) which is based on the addition of 300 µL of 75 µM of G4 structure under ambient temperature (a) fluorescence response (b) bar graph of $F_1/(F_0-F_2)$ vs. Nucleic Acid Structures. The error bars indicate SD (n=3). 69
Figure 22. (a) Fluorescence spectra of 2.5 ppm N, S-CQDs/ThT (final concentration 40.98 µM) probe upon the addition of different volumes (10 – 300 µL) of HER2 G4

stock solution (75 μM). (b) Plot of $F_1/(F_0-F_2)$ vs. HER2 G4 concentration under ambient temperature. The error bars indicate SD (n=3). 71
Figure 23. CD spectra of HER2 G4 (3.0 μM), HER2 G4/ThT (3.0 μM/3.0 μM), N,S-CQDs/ThT/HER2 G4 (2.5 ppm/3.0 μM/3.0 μM) and N,S-CQDs/ThT (2.5 ppm/3.0 μM) samples recorded at optimized conditions. 72
Figure 24. HR-TEM micrographs of the synthesized N,S-CQDs upon addition of ThT under the optimized conditions (a and b) and the probe system (N,S-CQDs/ThT) after the addition of the target analyte (c and d), at different magnifications..... 73
Figure 25. Absorbance spectra of standard sample (quinine sulfate) at different values (0.00, 0.02, 0.04, 0.06, 0.08 and 0.10 Abs) at 350 nm. 112
Figure 26. Fluorescence spectra of standard sample (quinine sulfate) at different absorbance values (0.00, 0.02, 0.04, 0.06, 0.08 and 0.10) for quantum yield calculation. 112
Figure 27. Absorbance spectra of N,S-CQDs at different absorbance values (0.00, 0.02, 0.04, 0.06, 0.08 and 0.10) at 350 nm 113
Figure 28. Fluorescence spectra of N,S-CQDs at different absorbance values (0.00, 0.02, 0.04, 0.06, 0.08 and 0.10) for quantum yield calculation. 113
Figure 29. Fluorescence spectra of N,S-CQDs/ThT in the absence (final concentration 40.98 μM) and the presence of HER2 G4 (final concentration 7.38μM). 114
Figure 30. Fluorescence spectra of 2.5 ppm N,S-CQDs/ThT (final concentration 40.98 μM) probe upon the addition of different volumes (10.0 – 300.0 μL) of HER2 G4 stock solution (75 μM)..... 115
Figure 31. Fluorescence spectra of 2.5 ppm N,S-CQDs titrated with increasing volumes (10.0 – 250.0 μL) of $5.0x10^2$ μM ThT solution (1^{st} replication)..... 115
Figure 32. Fluorescence spectra of 2.5 ppm N,S-CQDs titrated with increasing volumes (10.0 – 250.0 μL) of $5.0x10^2$ μM ThT solution (2^{nd} replication). 116
Figure 33. Fluorescence spectra of 2.5 ppm N,S-CQDs titrated with increasing volumes (10.0 – 250.0 μL) of $5.0x10^2$ μM ThT solution (3^{rd} replication)..... 116

Figure 34. Fluorescence Intensity vs. Temperature (°C) graph of N,S-CQDs (2.5 ppm), at the emission wavelength of 406 nm. 117
Figure 35. Fluorescence Intensity vs Temperature (°C) graph of N,S-CQDs (2.5 ppm), at the emission wavelength of 494 nm. 117

LIST OF SCHEMES

SCHEMES

Scheme 1. Schematic illustration of the synthesis procedure of N,S-CQDs. 43
Scheme 2. Schematic representation of possible mechanism of the developed probe for the detection of HER2 G4 structure. 74

LIST OF ABBREVIATIONS

ABBREVIATIONS	
0D	0-Dimensional
1D	1-Dimensional
2D	2-Dimensional
3D	3-Dimensional
AgNPs	Silver Nanoparticles
AuNPs	Gold Nanoparticles
BCL2	B-Cell Lymphoma 2
C-MYC	Cellular MYC (Myelocytomatosis)
CD	Circular Dichroism
CDs	Carbon Dots
CNDs	Carbon Nanodots
CQDs	Carbon Quantum Dots
DLS	Dynamic Light Scattering
DNA	Deoxyribonucleic Acid
dsDNA	Double Stranded Deoxyribonucleic Acid
FRET	Förster Resonance Energy Transfer
G-quadruplex, G4	Guanine-Quadruplex
GO	Graphene Oxide
GQDs	Graphene Quantum Dots
HER2	Human Epidermal Growth Factor 2

HR-TEM	High Resolution Transmission Electron Microscopy
HR-XPS	High Resolution Photoelectron Spectroscopy
IncRNAs	Long Non-Coding RNAs
K-RAS	Kirsten Rat Sarcoma
miRNAs	*microRNAs*
MNPs	Magnetic Nano Particles
mRNAs	*Messenger RNAs*
N-CQDs	Nitrogen-Doped CQDs
N,S-CQDS	Nitrogen and Sulfur Co-Doped CQDs
NSMs	Nanostructured Materials
OER	Oxygen Evolution Reaction
PL	Photoluminescence
PSA	Prostate Specific Antigen
QDs	Quantum Dots
QY	Quantum Yield
RB	Retinoblastoma
RNA	Ribonucleic Acid
SQDs	Semiconductor Quantum Dots
ssDNA	Single Stranded Deoxyribonucleic Acid
ThT	Thioflavin T
UV-vis	Ultraviolet-Visible
VEGF	Vascular Endothelial Growth Factor

XPS	X-ray Photoelectron Spectroscopy
XRD	X-Ray Diffraction

CHAPTER 1

INTRODUCTION

1.1 Nanotechnology

Development and research that lead to the controlled investigation and manipulation of structures and devices that have dimensions ranging from 1 to 100 nanometers are referred as “Nanotechnology”. Materials at this scale differ significantly from those at the bulk scale in terms of their physical and chemical properties and functions [1]. The field of nanotechnology includes a wide range of materials: Fullerenes, nanoparticles, nanopowders, nanotubes, nanowires, nanorods, nanofibers, quantum dots, dendrimers, nanoclusters, nanocrystals, nanocomposites, and so on [2]. At the beginning of the 1980s, cluster science and the development of the scanning tunneling microscope, a potent tool for atomic-scale surface imaging, aided in starting the concepts of nanotechnology and nanoscience. The discovery of fullerenes in 1985 and carbon nanotubes a few years later were both a result of progress mainly in these areas. Another advancement was the study of semiconductor nanocrystal synthesis and characteristics, which resulted in a rapid rise in the production of metal and metal oxide nanoparticles as well as quantum dots [3]. The nanomaterials' small size, enhanced solubility, multifunctionality, and surface adaptability open many new research opportunities in several fields [4], including medicine [5], food industry [6], agriculture [7], biotechnology [8], renewable energies [9], and cancer diagnosis [10]. As an example, the rapidly growing field of nanotechnology allows researchers to design and develop multifunctional materials that can be used for the detection of biomarkers, including cancer biomarkers that play crucial roles in the treatment, diagnosis, and progression of cancer [1]. Nanomaterials offer effective, reliable biosensing with high sensitivity and selectivity [11]. For instance, in one such study, Pan and co-workers [12]

revealed that poly-L-lactide nanoparticles can be used to detect vascular endothelial growth factor (VEGF) and prostate-specific antigen (PSA) associated with prostate cancer. In another study, Ma [13] reported that the core-shell Au@Ag nanorods can detect human epidural growth factor 2 (HER2) biomarker.

1.2 Nanostructures

Nanostructures are defined as structures with at least one dimension between 1 and 100 nm [14]. Low-dimensional materials that contain submicron or nanoscale building blocks in at least one dimension and exhibit size effects are called nanostructured materials (NSMs) [15]. NSMs are classified into one of the following subclasses: 0-dimensional (0D), 1-dimensional (1D), 2-dimensional (2D), or 3-dimensional (3D), and all NSMs can be fabricated/made from basic building blocks with low dimensionality, and these dimensionalities can be 0D, 1D, and 2D. Since 3D units cannot be used to build low-dimensional nanostructures (except 3D matrix), they are not included in the list. However, when 3D structures are built from 0D, 1D, and/or 2D building blocks, they are accepted as nanostructures [15]. Their nanoscale size enables novel and significantly improved physical, biological, and chemical properties [16].

NSMs are divided into three main groups (inorganic nanomaterials, nanocomposites, and organic nanomaterials), each of which is in turn subdivided into several subgroups. One of the subgroups of inorganic nanomaterials that stood out from other nanostructures in the field of biosensing is quantum dots [17]. Quantum dots are semiconductor nanostructures with novel and unique properties [18].

1.2.1 Semiconductor Nanostructure

Semiconductors are a class of materials with conductivities between those of metals and insulators [19]. Semiconductors exhibit band gaps between conductors and insulators, where the valence band is filled with electrons and the conduction band is empty as shown in Figure 1 [20], [21].

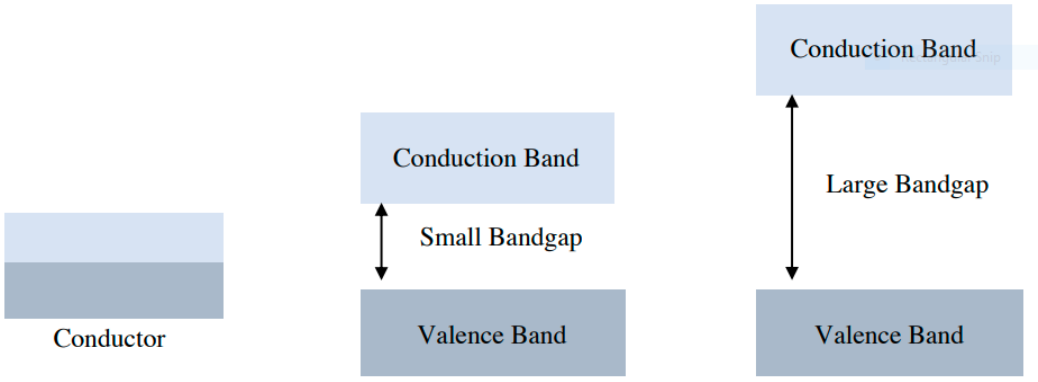

Figure 1. The electronic band structure of insulators, semiconductors, and conductors (metals). Adapted from [22].

A nanostructure is defined as a semiconductor nanostructure if the geometrical extent of a semiconductor in one, two, or three spatial dimensions is reduced below the size of the "de Broglie wavelength" of a charge carrier (~ 10 nm), in other words, if it is reduced to a few nanometers [23], [24]. In the last decade, semiconductor nanostructures have attracted considerable attention mainly for two reasons. First, since their length scales are equal to or smaller than the de Broglie wavelength, they allow the creation of artificial potentials for electrons, holes, and charge carriers in semiconductors. As a result, quantum confinement effects become crucial. Second, quantum mechanics can be applicable to practical interests as well as academic interests since additional degrees of freedom makes it achievable to design new device concepts since limitations related to material properties are shifted or lifted with the additional degrees of freedom in the structure. Quantum wells, quantum wires, and quantum dots can be given as examples of semiconductor nanostructures [25]. In particular, semiconductor nanostructures have great potential in nano- and

optoelectronics [26]. Furthermore, quantum dots are shown to play a crucial role in nanotechnology for optical imaging in vitro, in vivo, and ex vivo [27].

1.2.2 Quantum Dots

Quantum dots (QDs) are nano-sized fluorescent semiconductor particles. They are made of heavy metals or inorganic substances and range in size from 2 to 10 nm. The term "quantum dots" refers to the quantum confinement (electron or hole is confined in a potential well with a diameter comparable to the wavelength of the electron) and optical properties of particles. Since they display a set of discrete and narrow energy levels, they are also known as artificial atoms [28], [29]. QDs have the form of a crystal core and a shell that can be modified easily. Based on their core material, they can be categorized as nonmetallic QDs (silicon (Si) and carbon (C) core) or metallic QDs (indium (In) and silver (Ag) core), or composite QDs (carbon (C) core) which are based on coupling of carbon QDs with semiconductors or oxides or metal and semiconductors such as CQDs/Ti_2O, CQDs/ZnO, and CQDs/Ag/Ag_3PO_4 and etc. [30], [31]. QDs are also divided into three categories as core-type QDs, core-shell QDs, and alloyed QDs. Single-component materials with uniform internal compositions, such as selenides or sulfides, are defined as core-type QDs. The core/shell type of quantum dots have small regions of one material embedded in another material as represented in Figure 2. Finally, alloyed QDs are formed by two nanocrystal semiconductors that have different bandgap energies [32].

The development of core/shell technology through the chemical modifications and doping of semiconductor quantum dots (SQDs) have led to further practical use of QDs in a wider range of applications by overcoming the difficulties arising from the nature of QDs [33]. For example, doping QDs improves dopant emission lifetime and cytotoxicity, and surface passivation can help to increase stability, prevent oxidation, and disperse dots in various solvents [34], [35].

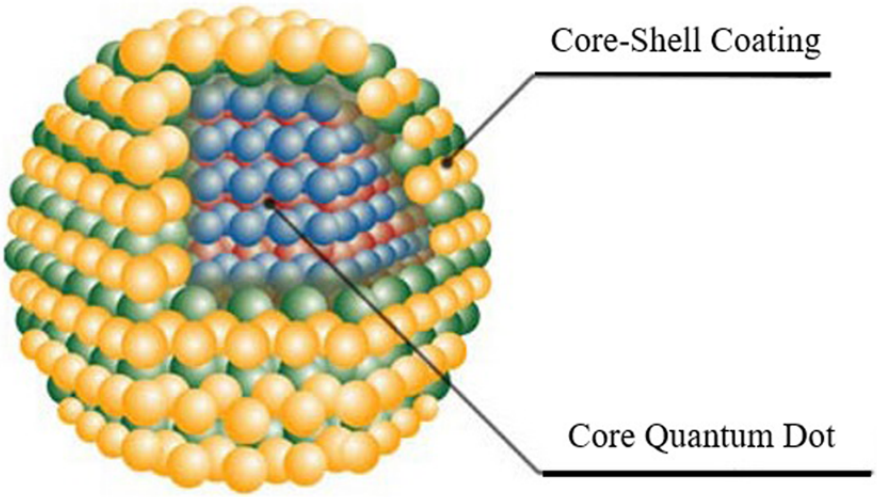

Figure 2. Schematic representation of core/shell structure of QDs. The blue and red colored spheres represent the core of the quantum dot, while the yellow and green spheres represent the core-shell coating. Adopted from [32] , reproduced with permission from Walter de Gruyter and Company.

Among quantum dots, carbon quantum dots (CQDs) have unique properties that set them apart from metallic QDs due to their comparable optical properties, low toxicity, easy and inexpensive synthesis, and better controllability over physicochemical properties through surface passivation and functionalization [36].

1.2.2.1 Carbon Quantum Dots

Carbon quantum dots are a new type of nano-carbon structures [37]. They are classified into three major groups; CQDs, graphene quantum dots (GQDs), and carbon nanodots (CNDs) [38]. While the CQDs and GQDs have quantum confinement, quantum dots without quantum confinement are referred as CNDs [39]. Figure 3 shows the schematic structures of the classification of carbon-based quantum dots. As can be seen, the GQDs have π-conjugated single sheet where CQDs have spherical structure, and CNDs have the quasi-spherical structure [39].

The CNDs usually lack polymeric features, noticeable crystal lattice structure, and quantum confinement effect, but they have a few chemical groups on the surface and high carbonization. Their photoluminescence properties are usually caused by the defect or the surface state within the graphitic core [40]. Compared to the CNDs, the GQDs are small graphene fragments composed of single or few graphene sheets with evident graphene lattices and chemical groups within the interlayer defect or on the edge, which contribute to unique features such as the edge effect and quantum confinement effect [40]. Their edge structure and conjugated π-domains contribute to distinctive luminescence characteristics [38]. The CQDs are zero-dimensional carbon particles. When compared to other carbon dots, they are less poisonous, biocompatible, and due to oxygen content, they are soluble and dispersible in water. They possess discrete optical and photoluminescence characteristics that can be modified with ease [41].

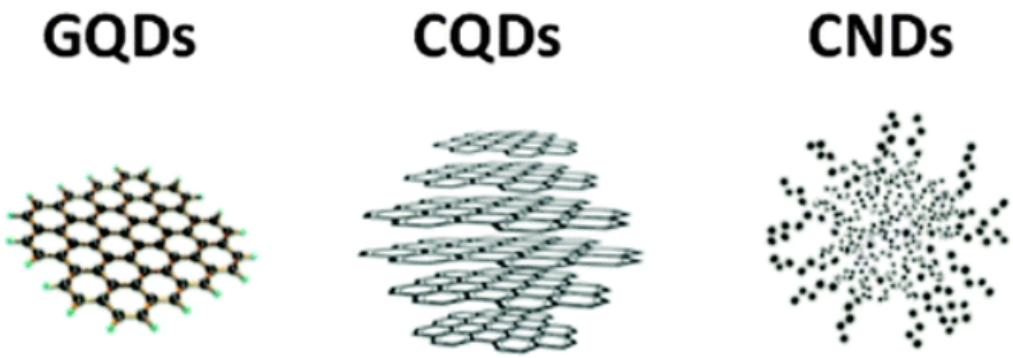

Figure 3. Schematic representation of the classification of carbon-based quantum dots: GQDs, CQDs, and CNDs. Adopted from [39], reproduced with permission from Royal Society of Chemistry.

Carbon quantum dots (CQDs) are biocompatible nanoparticles with diameters less than 10 nm with various unique optical and physical properties. In 2004, Xu et al. [42], during the purification of single-walled carbon nanotubes, discovered fluorescent carbon nanoparticles "unintentionally." Two years later, in 2006, Sun et al. [43], synthesized the first stable photoluminescent carbon nanoparticles in

different sizes and called them “carbon quantum dots”. The following year, Cao et al. [44], reported that water-soluble CQDs containing polypropionylethylenimine-co-ethylenimine can be used as surface passivating agents. Since then, various synthetic methods for the preparation of CQDs with different sizes and surface functional groups have been released [40].

Figure 4 depicts the schematic diagram of the chemical structure of CQDs. The chemical structures of CQDs derived from different carbon resources consist of sp^2/sp^3 hybrid conjugated carbons and usually nitrogen-containing/oxygen-containing/polymeric groups (e.g., C-O, C=O, C-N, -COOH, -OH) [38]. The presence of -COOH, - OH and $-NH_2$ groups on their surface gives them the ability to bind to various organic, polymeric, inorganic, or biological materials, making them efficient candidates for several applications in different fields [45]. For instance, Zhang and co-workers produced carbon quantum dot films with oxygen-containing groups on the surface to detect humidity and gas sensing [46]. CQD structures may also contain cores that are amorphous or graphitic crystalline based on the degree of the existence of sp^2 hybrids in the core. Reaction temperatures below 300°C usually result in an amorphous core unless the precursor contains sp^2/sp hybrid carbon, while reaction temperatures above 300°C usually result in significant graphitization [47]. Interestingly, it has been recently demonstrated by Galan and co-workers that the core could have crystalline and amorphous structures simultaneously [48]. The interesting features of both amorphous and crystalline structures include wavelength-dependent emission, low toxicity, high solubility, photoluminescence, biocompatibility, and ease of functionalization [49]. The use of CQDs in different fields are depicted in Section 1.3.

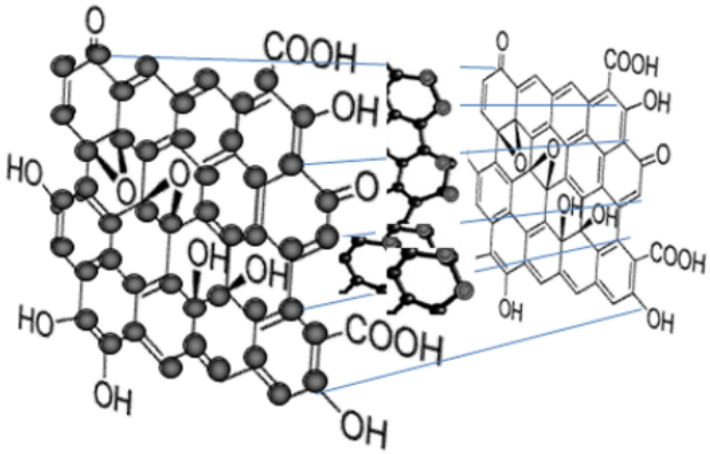

Figure 4. Schematic representation of the chemical structure of CQDs. Adopted from [50], reproduced with permission from IOP Publishing, Ltd.

1.2.2.2 Properties of Carbon Quantum Dots

In general, QDs exhibit unique optical features, including high fluorescence stability and broad excitation and emission spectra that allow them to be used in a wide range of applications. Conventional QDs are often manufactured using semiconducting elements, particularly sulfur and selenium, along with suitable second element in an organic-phase or water-phase systems. Conventional QDs especially raise concern about their toxicity and expense. However, CQDs are known to be more environmentally friendly luminescent materials with low toxicity and expenditure. They possess excellent water solubility, impeccable biocompatibility, outstanding optical properties (high fluorescence), chemical inertness, facile functionalization, and photobleaching resistance [51]. CQDs typically exhibit dominant emission in the blue range and strong UV absorption. Some CQDs exhibit excitation-dependent emission, with an emission spectrum that is always broad and extended to longer wavelengths with decreasing intensity. The optical properties (absorption, excitation, and emission) of CQDs are strongly associated with the particle size, structure, precursor type, reaction medium, and surface properties [52]. Thereby, their emission spectra can be tuned easily for different applications. In order to tailor the

physical and chemical properties of CQDs, numerous methods have been developed to create simple and practical strategies like functionalization (including surface passivation and heteroatom doping) [53]. The surface passivation method is generally considered as unfavorable due to the organic reagents or catalysts, that are used for the functionalization, being cytotoxic and environmentally hazardous, along with the process being time-consuming [53]. Additionally, surface functionalization with small organic molecules and polymers requires complicated purification steps and syntheses that can lead to low production yields. Some of the original functional positions of CQDs for analytical and sensing applications are also reported to be cytotoxic and environmentally harmful [53], [54].

Besides surface passivation, metal and non-metallic atom doping are other methods for functionalization where the resulting products are referred as heteroatom doped CQDs. The metal atoms used in doping generally have larger radii than the carbon atom, resulting in non-uniform and ineffective doping of CQDs [43]. Also, metal ions used in doping process usually results in toxicity, which is an undesirable major issue [53]. On the other hand, non-metallic heteroatom doping has been shown to positively improve the water solubility, quantum yield, fluorescence properties, and other physicochemical properties of CQDs [55]. Introducing non-metallic atoms (e.g., boron, fluorine, nitrogen, sulfur, and phosphorus) into CQDs, aims to change the electronic structures related to the energy gap of CQDs and give rise to different intrinsic properties [54]. Studies have shown that CQDs have electronic structures and electronic transitions ($\sigma \rightarrow \pi^*$, $\pi \rightarrow \pi^*$, $n \rightarrow \pi^*$, and $n \rightarrow \sigma^*$) that are closely related to their physicochemical properties, especially their optical properties like luminescence and light absorption [56]. The interactions between π- and n-states are thought to be affected when heteroatoms are bound to CQDs, due to the ability of heteroatoms to withdraw or donate electrons or to overlap orbitals [54].

Moreover, the same heteroatoms can also be used together to prepare co-doped CQDs. CQDs have different properties depending on the co-doping atom. For instance, B and N co-doped CQDs exhibit stable fluorescence emission over a broad

range of pH; F and N co-doped CQDs have an enhanced π-electron system, resulting in a red shift under excitation at 530 nm; N and P co-doped CQDs exhibit outstanding fluorescence stability throughout a wide pH range (4-11), ultra-high ion strength, and continual UV light irradiation and N and S co-doped CQDs display strong fluorescence emission, higher QY than n-doped CQDs, superior excitation-wavelength-independent photoluminescence, and distinctive optical characteristics with dual-emission (blue and yellow) under single excitation wavelength [57].

1.2.2.3 Synthesis of CQDs

Numerous methods for synthesizing CQDs that are mainly classified into two categories: Top-down and Bottom-up approaches, have been presented in the literature. The presented studies mostly focused on simplicity, cost-effectiveness, size controllability, and scaling-up for synthesizing CQDs with advanced functionality and various structures [58].

Figure 5 depicts a general representation of the experimental setup and apparatus for the synthesis of CQDs by using Top-down and Bottom-up synthesis strategies. In the Top-down synthesis, different techniques such as the electrochemical method [59], arc discharge [42], and laser ablation [60] are used to reduce the size of starting materials (to the smaller pieces) in order to obtain nanostructures. Graphite, activated carbon, nanodiamonds, and carbon nanotubes are carbon materials that have been synthesized using this approach [36]. The electrochemical oxidation method is simply based on the electrochemical carbonization of organic compounds with low molecular weight (such as alcohols) by applying direct current [61]. Although the process is low-cost, facile, and contains almost no toxic chemicals, it requires very time-consuming purification processes [62]. The arc discharge is a technique where carbon atoms that are decomposed from bulk carbon precursors are reorganized in an anodic electrode powered by gas plasma generated in a sealed reactor. To produce high-energy plasma, with an application of electric current, the reactor's temperature can reach up to 4000 K. In the cathode, CQDs are formed by the assembly of carbon

vapor [40]. The CQDs that are synthesized by this method exhibit good water dispersibility. However, disadvantages such as the lower quantum yield of CQDs, agglomeration in water, and non-uniform size distribution, as well as the difficulty of industrial synthesis due to multiple preparation steps and stringent experimental conditions, make this method impractical [63]. In the laser ablation technique, CQDs are synthesized from the carbon sources, which are the targets of the laser source that is irradiated under high pressure and temperature in the presence of water vapor under inert gas. In a typical procedure, the carbon precursor is dispersed into the selected solvent by sonication. Then, the suspension is released into a glass cell for the carbonization reaction by a laser beam. Carbon sources that are shredded by the laser beam are subjected to a centrifugation process to obtain fluorescent CQDs [64]. It is an effortless and effective technique for the synthesis of CQDs with varying sizes. Conversely, the laser ablation method requires a large amount of carbon source and the synthesized CQDs using this technique have low quantum yields, with lack of size variation and control [65].

The Bottom-up strategies are based on growing CQDs from mainly organic precursors (such as citric acid and saccharides). CQDs of the required size can be synthesized at a large scale cost-effectively by adjusting the experimental parameters [66]. The main Bottom-up approaches include thermal combustion/template-assisted/hydrothermal processes and microwave/ultrasonic-assisted approaches [67]. Bottom-up approaches have the advantage of providing good synthetic control and, as a result, good size control compared to Top-down approaches. The properties of CQDs can be significantly influenced by the origin of the carbon source used in Bottom-up approaches [68].

Microwave/ultrasonic-assisted synthesis is one of the commonly employed Bottom-up synthesis approaches. In microwave-assisted synthesis for carbonation of a wide range of precursors, microwave radiation is often used in the presence of water-soluble surfactants [69]. Ultrasonic-assisted synthesis is similar to microwave synthesis in general. However, sonication requires a longer timescale for the

synthesis of CQDs [69]. In ultrasonic-assisted synthesis, when high-power ultrasonic waves are applied to the solvent, small vapor bubbles with high temperature and pressure are temporarily formed. This process is called the cavitation process. The use of this effect to trigger chemical reactions is known as sonochemistry, and it has already been employed in the synthesis of CQDs [69]. Both methods have the advantage of being simple, inexpensive, and scalable; however, poor control over the size makes these synthesis methods unfavorable [62].

Hydrothermal/solvothermal synthesis, as one of the main Bottom-up approaches, is non-toxic, low-cost, and eco-friendly method of synthesizing CQDs from various carbon sources [64]. In this technique, organic resources are blended with water and/or organic-based solvents in a Teflon-lined sealed autoclave which is designed to resist high temperatures and pressures. The reaction mixture is allowed to react at a high temperature for a certain period of time for carbonization. After carbonization, the autoclave is allowed to cool down to room temperature, and then the products are centrifuged to separate/purify the product, followed by filtration [70]. Compared to the other synthesis techniques, the hydrothermal method possesses significant advantages. First, CQDs synthesized by this method are generally found to have lower cytotoxicity, higher fluorescence quantum yield, and good stability. Second, due to the facile and inexpensive fabrication, this approach can be considered environmentally friendly when waste or green carbon sources are used as precursors [71]. However, poor control over the sizes of the synthesized CQDs can be considered as the main drawback of this method [65].

Overall, almost all the synthesis approaches need to be optimized to overcome problems such as agglomeration, homogeneity, particle size control, and surface properties in the synthesis of CQDs [62]. Accordingly, the choice of the most appropriate synthetic route, and the application of post-synthetic processes, are the essential factors that should be taken into consideration to overcome these obstacles in the synthesis of CQDs.

Within this thesis study, we preferred to use thermal synthesis method using a Teflon-lined sealed autoclave mainly due to its availability and simplicity in the synthesis of heteroatom co-doped CQDs that are used in the detection of G4 forming oligonucleotide found in the promoter region of human epidermal growth factor 2 (HER2).

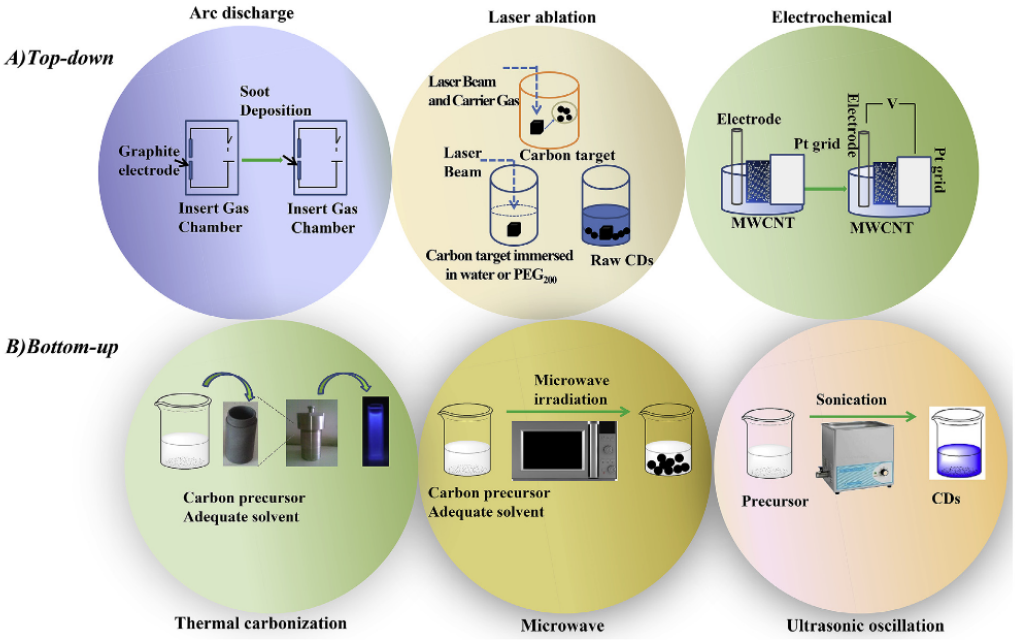

Figure 5. Schematic representation of the experimental setup and apparatus for the synthesis of CQDs by using "Top-down" and "Bottom-up" synthesis strategies. Adopted from [72], reproduced with permission from Elsevier.

1.3 Applications of Carbon Quantum Dots

The applications of CQDs have received much attention due to their non-toxicity, biocompatibility, high fluorescence, chemical inertness, easy functionalization, and resistance to photobleaching. CQDs' photoluminescence (PL) characteristics provide clear routes especially for sensing applications. Particularly, the well-known dynamics of fluorescent systems such as sensitive fluorescence spectra, fluorescence

quenching, and energy transfer properties lead to widespread uses of CQDs in chemical sensing, resulting in their use especially in the field of optical sensors [73]. Furthermore, their phosphorescence and florescence properties make them really good candidates for bioimaging and drug delivery applications [74]. The large specific surface area of CQDs which act as abundant active sites for intermediates and electrolytes, their high electrical conductivity, which increases efficient electron transfer, their surface functionalization which increases the number of active sites, leading to improved electrocatalytic performance, and their ability be doped with heteroatoms which enables the tailoring of the electronic structure of CQDs, leading to a change in electronic properties led to their relatively extensive use in the fields of electrocatalysis and energy storage [75]. CQDs are also robust and photostable, with excellent photobleaching resistance, which prevents photo corrosion upon exposure to light, and can therefore be used in photocatalytic applications [76]. Several applications exploiting the use of CQDS in different fields are given in detail below. In this study, CQDs are used as sensing elements in the development of a G4 detection platform.

1.3.1 Use of CQDs in Bioimaging

CQDs are excellent candidates for in vivo and in vitro fluorescence bioimaging applications due to their visible emission and excitation wavelengths and high fluorescence brightness. Atchudan and co-workers synthesized CQDs from banana peel waste by a hydrothermal method to image the entire body of nematodes. Since the synthesized CQDs did not contain any additional chemicals, they showed low toxicity and high biocompatibility even at high concentrations. In addition, the synthesized CQDs showed high photostability. They reported that his bioimaging technology would open up a new door for the application of CQDs in targeted drug delivery of nanomedicines [77].

As another example, Sharma and coworkers synthesized CQDs from denatured sour milk by a hydrothermal method for the imaging of U-251 MG glioblastoma cell lines

in vitro. Synthesized CQDs exhibited high stability under changing pH and excellent photostability. They also had low toxicity even at high concentrations. Without excitation, the cells showed no fluorescence emission, but with excitation, the CQDs displayed blue emission within the cells. The blue emission was observed in the cell membrane, cytoplasmic area and deep in the nucleus with strong edge glow (high marginal glow) proving that the synthesized CQDs can be used in vitro bioimaging studies [78].

1.3.2 Use of CQDs in Drug Delivery

CQDs have recently attracted increasing attention also in drug delivery applications. Su and coworkers demonstrated that cancer stem cell nucleus-permeable red-emissive CQDs (CSCNP-R-CQDs) synthesized by the solvothermal method can be loaded with doxorubicin (DOX) on the surface (CSCNP-R-CQDs/DOX). They used HeLa cells for the experiment and found that free DOX reduced the cell viability to 50%, while CSCNP-R-CQDs/DOX reduced the cell viability to 21% and decreased the proportion of cancer stem cells in vivo, leading to successful drug delivery with CQDs [79]. Hua and coworkers synthesized novel CQDs that are not captured by lysosomes or endosomes and instead can target mitochondria. Moreover, they demonstrated that the synthesized CQDs showed excellent long-term imaging in mitochondria for at least 24 h even in a culture medium, in contrast to the commercial mitochondrial imaging dye MitoTracker, which cannot achieve long-term tracking in mitochondria due to its restriction to serum-free working conditions. After modifying the CQDs with rose begal (RB), a photosensitizer, they treat the MCF -7 cells. Their results revealed that the high efficiency of photodynamic therapy could be enabled by the ability of the CQD-RB complex for efficient cell penetration and mitochondria targeting resulting in successful avoidance of the capturing of nanomissiles by lysosomes. Overall, their platform revealed the use of CQDs as great candidates for fluorescent mitochondria targeting drug delivery platform [80].

1.3.3 Use of CQDs in Photocatalytic Applications

CQDs possess unique photo-induced electron transfer property and outstanding light-harvesting/collection ability, and these properties have made them attractive for photocatalysis applications [31]. For example, Kang's group synthesized CQDs with an electrochemical ablation method using graphite which can act as a catalyst and has a high ability to generate protons by visible light in solution. They investigated the ability of CQDs to generate protons in a light-induced manner by performing a series of reactions with acid as a catalyst under 10-h irradiation w/o visible light. They discovered that the visible light could enhance the catalytic activity of CQDs in acid-catalyzed reactions [81]. On the other hand, Sun's group synthesized gold-coated CQDs to convert CO_2 to small organic acids. The experiment of CO_2 reduction via photocatalysis was performed in an aqueous solution of gold-doped CQDs. Compared to other catalysts, this led to the formation of a significant amount of acetic acid. The result revealed that the CQDs could act as effective photocatalysts [82].

1.3.4 Use of CQDs in Electrocatalysis Applications

Properties such as fast electron transfer and large surface area make CQDs ideal for energy conversion systems. Since CQDs have a significant number of functional groups on their surface, surface functionalization and preparation of multicomponent electrocatalysts can be easily carried out [83]. Li and co-workers synthesized carbon-supported Ru nanoparticles (Ru@CQDs) for hydrogen evolution reaction. The development of hydrogen evolution reaction electrocatalysts with Pt-like or even greater activity, particularly the ones that can operate in an alkaline environment, is still a difficult task to accomplish. However, electrochemical measurements performed by Li et al. have shown that Ru@CQDs exhibited excellent catalytic performance for the hydrogen evolution reaction even under strongly alkaline conditions. Under alkaline conditions, the catalytic properties of Ru@CQDs were

found to be superior to those of most noble metals, non-noble metals, and non-metallic catalysts as well as commercial Pt/C catalysts [84]. Yang and co-workers coupled N-doped carbon and NiFeOx clusters using metal nitrite salts and N-CQDs. The N-CQDs formed successive layers of N-doped carbon dots that could be coupled to the $NiFeO_x$ clusters as nitrogen-containing carbonaceous building blocks. The $NiFeO_x$©NC hybrid exhibited superior performance in oxygen evolution reaction (OER) compared to the dimensionally stable anodes and commercial RuO_2 catalyst. $NiFeO_x$©NC exhibited faster kinetics and lower overpotential, as well as outstanding long-term durability, environmental adaptability and rate capability under the conditions investigated [85]. Overall, all these studies have proven that CQDs have a great potential also in electrocatalytic studies.

1.3.5 Use of CQDs in Energy Storage Applications

Among many other applications, CQDs are also desirable for energy storage applications due to their structure, physicochemical characteristics, and good electrical conductivity. Manufacturing cells with powdered electrode materials requires binders and conductive additives, resulting in poor energy storage [86]. Balogun and co-workers found that coating the surface of intertwined VO_2 nanowires with CQDs, which are incredibly flexible in shaping the surface of the nanowires, protects not only the surface of the electrode but also improves the Li^+ and Na^+ ion storage performance of the batteries [86]. Jing and co-workers coated Mn_3O_4 nano-octahedral particles' surfaces with CQDs and obtained Mn_3O_4/C-dots composites with octahedral Mn_3O_4 which increases the electrochemical properties like long-term stability and high capacity of Li^+ ion batteries. After the synthesis and characterization were completed, it was proven that Mn_3O_4/C-dots composites outperform pure Mn_3O_4 in terms of lithium storage capacity [87].

1.3.6 Use of CQDs in Chemical Sensing

One of the dominant applications of CQDs is chemical sensing. CQDs are broadly used for this application due to their great chemical stability, high photostability, low toxicity and water solubility, and excellent optical and chemical properties [88]. CQDs are widely used in detection of heavy metal ions such as Hg^{2+} because of their hazardousness to human health and the environment. The detection platforms developed usually took advantage of the fluorescence quenching of CQDs upon addition of metal ions [88]. Zhang and Chen synthesized nitrogen-doped CQDs (N-CQDs) by the hydrothermal method for the detection of Hg^{2+}. The proposed system is based on the fluorescence quenching of CQDs upon addition of increasing concentrations of Hg^{2+} ions. They reported that the detection platform was sensitive with the detection limit of 0.23 μM. From selectivity studies, the synthesized N-CQDs were found to possess excellent selectivity toward Hg^{2+} ions. They also tested the proposed system for detection of Hg^{2+} ions in lake water and tap water samples. Their results revealed that the proposed system could be used as a chemical sensor in environmental applications [89]. In addition to direct detection of heavy metal ions, CQDs along with heavy metal ions can also be used as a probe to detect amino acids and other ions. Huang and co-workers synthesized N-doped CQDs with the solvothermal synthesis method to detect L-cysteine, a vital amino acid for human health [90]. Moreover, iodide is an essential ion for human health. Iodide deficiency and radioactivity are linked to a number of diseases [91]. Huang et al. used Hg^{2+} as a fluorescence quencher for N-CQDs and reported a detection limit of 83.5 nM for Hg^{2+}. Moreover, they reported that the addition of L-cysteine and I^- ions separately to the N-CQDs/Hg^{+2} probe could restore the fluorescence intensity, resulting in detection limits of 45.8 and 92.3 nM, respectively. They stated that the proposed probe is highly selective and sensitive to L-cysteine and I^- and the system can be applied to real samples in a future study [92]. CQDs are also used for the detection of nucleic acids. Loo and co-workers synthesized carboxylic CQDs from malic acid for the detection of single-stranded DNA (ssDNA). The proposed system is based on

fluorescence quenching of carboxylic CQDs with the addition of ssDNA with a fluorescent label. After addition of the complimentary ssDNA to the probe, the fluorescence recovery was observed due to hybridization of complimentary DNAs resulting in the formation of the double-stranded DNA (dsDNA). The limit of detection was reported as 17.4 nM and dynamic range as 0.04 – 400 nM. The proposed fluorescent detection platform was stated as a possible foundation for disease diagnosis [93]. Additionally, Kumari's group synthesized N-doped CQDs from mushroom for the detection of a G-quadruplex (G4) structure. The experiment is based on fluorescence recovery after addition of Hemin to N-doped CQDs. Vascular endothelial growth factor (VEGF) G4 structure was used for the demonstration. The team stated that the detection of G4 was in the nanomolar range, and the limit of detection was 190 nM. Moreover, the most important aspect of the experiment was declared as the ability of the system to image the G4 with a hand-held UV lamp at ambient temperature was attainable [94].

In this thesis, we preferred to use CQDs for chemical sensing application due to their high fluorescence, applicability and simplicity. The recovery of the fluorescence quenching was used as a detection method in the detection of HER2 G4 structure.

1.4 Human Epidermal Growth Factor Receptor (HER2)

Human epidermal growth factor receptors (HER) are a group of four cell surface receptors belonging to the tyrosine kinase receptor family that transmit signals governing proper cell development and differentiation [95], [96] .

HER2 is a 185-kDa transmembrane receptor in the HER receptor family that also includes HER1, HER3, and HER4. A transmembrane lipophilic segment, binding domain, and a functional intracellular tyrosine kinase domain (except HER3) are the main components of these receptors. Both heterodimerization and homodimerization of the tyrosine kinase domains are activated by specific ligands. The extracellular domain of HER2, that is demonstrated in Figure 6, unlike the extracellular domains

of the other three HER receptors, can adopt a fixed conformation resembling a ligand-activated state, allowing it to dimerize in the absence of a ligand [97]. Downstream tyrosine kinase signaling cascades are activated with homodimerization or heterodimerization of the receptors, leading to cell proliferation, migration, invasion, and survival [98].

In 2020, it was estimated that 2.26 million cancer cases were breast cancer patients, which was found to be the most common cancer worldwide. Furthermore, it is also the leading cause of cancer mortality in women [99]. The regulation of normal breast growth and development is associated with HER receptor family. Amplification of HER2 protein overexpression is closely linked to invasive breast cancer, where the HER2 gene is amplified by approximately 15–20% [100]. HER2 gene amplification resulting in the overexpression of the receptor is found to be disrupting normal control mechanisms and potentially leading to the formation of aggressive tumor cells [101].

Figure 6. HER2 extracellular domain where colored sections represent subdomains. Adopted from [102], reproduced with permission from IntechOpen.

Breast cancer cells can have the potential to reproduce indefinitely via a variety of molecular processes. Breast cancer gene HER2 and others such as hTERT, HRAS, KRAS, and c-MYC impart higher proliferative ability and each of these genes have been associated to cancer silencing via DNA secondary structure generation [103]. That secondary structure of DNA is referred as G-quadruplex that is formed within guanine rich sequences. The structure constructed from several planar layers of four guanines linked together by Hoogsteen hydrogen bonding [104]. The HER2 promoter region has a 28-bp GGA repeat sequence that can create a G4 structure which was first discovered by Scott and Ebbinghaus in 2006 [105], [106]. In 2012, Zhang and co-workers stated that the promoter region of HER2 has similar guanine rich sequence to c-MYB proto-oncogene region which can form G4 structures. The sequence of HER2 and c-MYB stated as, respectively, 5′-AGG AGA AGG AGG AGG TGG AGG AGG AGG G-3′ and 5′-GGA GGA GGA GGT CAC GGA GGA GGA GGA GAA GGA GGA GGA GGA-3. They showedthe formation of HER2 G4 via circular dichroism mainly based on the similarities to c-MYB spectrum in the control experiments [105].

In the meantime, it has been discovered that, G4s were enriched in cancer breakpoints and the transcription start sites of highly transcribed genes in human cells, particularly in cancer-related genes, using high-throughput sequencing and a machine learning approaches [107]. The formation of G4 by HER2 promoter region is found to block transcription, resulting in HER2 suppression. A luciferase reporter test in breast cancer cells showed that stabilizing the HER2 promoter G4 structure reduced HER2 expression at both the mRNA and protein levels where the upregulation of HER2 results in breast cancer [103], [108].

In this context, in 2019, Cui and co-workers found out that the G-quadruplex structure of the HER2 promoter region may be necessary for the regulation of HER2 expression. They constructed two plasmids that are Wild-type (G-quadruplex can be formed) and mutant (G-quadruplex cannot be formed) and found that the use of the wild-type plasmid decreased HER2 promoter activity by approximately 40%,

whereas the mutant plasmid upregulated activity. Additionally, the G4 structure of HER2 can be stabilized by synthetic cyclic polyamide (cβ) which has high binding affinity towards G4 over the duplex DNA. To investigate the ability of cβ to suppress HER2 proto-oncogene expression and transcription, luciferase assay, quantitative real-time reverse transcription polymerase chain reaction (Q-RT-PCR) and Western blotting experiments were performed. Luciferase assay showed that when cβ concentration raised to 800 nM, relative luciferase activity of the HER2 plasmid steadily fell to less than 20%, demonstrating that cβ was inhibiting the activity of the HER2 promoter. RT-PCR and Western blotting tests confirmed this finding. After MCF-7 cells were treated with 0-100 μM cβ, the relative expression level of HER2 mRNA steadily dropped to close to 30%, suggesting that cβ may inhibit HER2 transcription [109]. Overall, all these results clearly supported the possibility of G4 as a possible target in HER2 associated breast cancer. And, since increased HER2 expression is associated with the progression and development of aggressive breast cancer, we hypothesized that the G-quadruplex structure of the HER2 promoter region may also be a target in breast cancer detection.

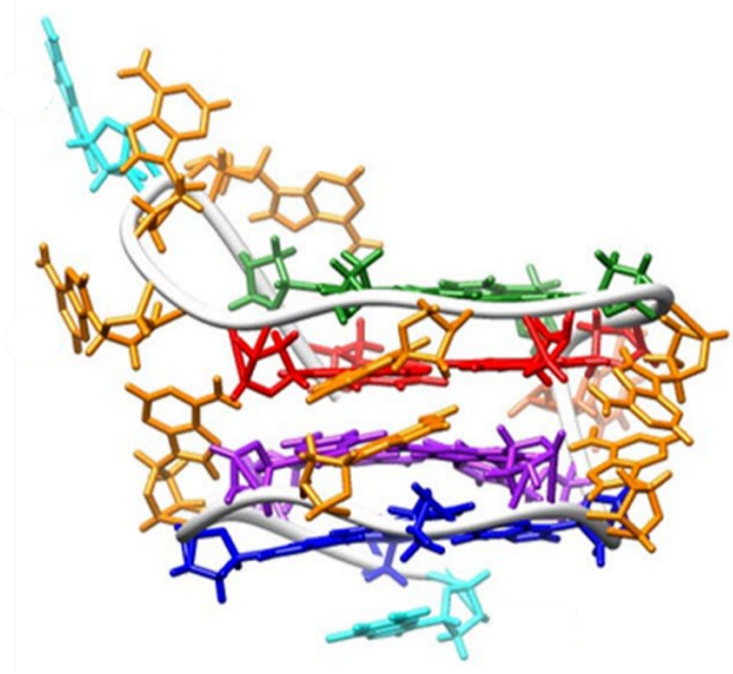

Figure 7. Representation of side view of HER2 G-quadruplex structure. Adopted from [109], reproduced with permission from Springer Nature.

1.5 Nucleic Acid Detection

Nucleic acids play a vital role in the transfer and storage of genetic information [110]. They are biological macromolecules formed by the repeating monomeric units (nucleotides) consist of a phosphate group, a pentose sugar (ribose or deoxyribose) and nitrogen-containing bases [111]. Nucleic acids are generally divided into two categories based mainly on the pentose sugars found as deoxyribonucleic acid (DNA) that exhibits a two-stranded helix structure and ribonucleic acid (RNA). DNA carries the genetic information in cells, in order to pass the genetic information to next generations, the genes on the DNA are transcribed into RNA which is consequently translated into the amino acid sequences to form proteins [112].

Accordingly, the detection of nucleic acids, the detection of specific nucleotide sequences, is an essential technique in many applications across different fields as forensic investigations [113], environmental and food analysis

[114], [115], gene therapy [116], and clinical diagnostics [117]. For instance, today nucleic acid detection, DNA profiling, is a robust screening tool in forensic investigations to solve criminal cases [118]. Nucleic acid detection is also an indispensable tool in detection of genetically modified organisms (GMOs) in food analysis. For instance, Passamano and Pighini developed a DNA-sensor (μLibra) to detect interactions between complementary nucleic acid strands with precise evaluation. It provides the opportunity to monitor hybridization in real time through the measurement of the quartz oscillation frequency fluctuation in a reaction based on the mass increase. A biotinylated DNA probe layer (representing the GMO phenotype) was used to functionalize the golden quartz surface due to its strong affinity for the previously placed streptavidin. The hybridization between the probe and the corresponding sequences were analyzed and the foreign gene's presence in food was identified [115]. Environmental analysis is another area in which nucleic acid detection is employed. Tombelli and co-workers reported a detection platform for Aeromaonas strains based on polymerase chain reaction and DNA piezoelectric biosensor. Aeromaonas strains found in fresh water, wastewater and sewage which create a wide range of extracellular toxins. These are linked to several human illnesses, including meningitis, wound infections, and septicaemia. In this study, the streptavidin-coated gold disk was used for the immobilization of biotinylated oligonucleotide probe. Streptavidin was covalently joined to the gold surface that had been thiol/carboxylated dextran modified. With the addition of the target oligonucleotide, piezoelectric biosensor detected the presence of the complementary strand [119]. In the case of gene therapy, Yu and co-workers used peptide nucleic acid (PNA)-based gene therapy for pancreatic ductal adenocarcinoma (PDAC) which is one of the deadliest malignant tumors. To hybridize the wild-type KRAS sequences, short PNAs that are complimentary to mutant region of target KRAS were developed. Briefly, the synthesized PNAs recognized the target and efficiently silenced the mutant KRAS gene [120].

Finally, nucleic acid detection is also becoming more important in clinical diagnostics. Molecular diagnostics based on nucleic acids are often used in clinics

for screening, diagnosis, risk assessment, and treatment planning in several diseases including cancer, congenital anomalies, and infectious diseases [121]. For example, Harvet et al. reported an optical detection platform for HIV, based on the conjugation of carbon nanotubes with complimentary sequence of the target oligonucleotide. After target oligonucleotide was added the results demonstrated a blue-shift in fluorescence response demonstrating the detection of target HIV oligonucleotide [122].

The detection of cancer biomarkers is another area where nucleic acid detection techniques have been widely used. For example, in 2020, Wang et al. used colloidal gold nucleic acid strip biosensor for the detection of single nucleotide polymorphism (SNP) as a cancer associated single nucleotide at genomic level in DNA sequence. The proposed technique relies on coupling gold nucleic acid strip biosensor with primer-specific polymerase chain reaction (PCR). DNA was extracted from human whole blood followed by 1st PCR and 2nd PCR (primer-specific). The product from the 1st PCR served as a template for the second PCR, which dramatically reduced the amount of non-specific amplification and produced the target product, resulted in the development of the optical detection of SNP on strip biosensor [123]. In another study, Zhang and co-workers, developed highly specific and selective microarray system for fluorometric detection of DNA and microRNA. The system combines the use of a hybridization chain reaction (HCR)-based signal amplification method with a DNA tetrahedral structured probe (DTSP). From created three different sized DTSPs (DTSP-17, DTSP-26 and DTSP-37), LOD of DTSP-26 reported to be as 10 aM. Also, it was reported that the developed system can recognize single base DNA mismatches [124].

In the last decade, PCR and microarray-based nucleic acid detection platforms have been broadly developed. However, these methods usually require expensive equipment, skilled personnel, and a great amount of time, which prevents their widespread use especially in developing nations where healthcare services are limited. To overcome these limitations, chip-based devices and microfluidic systems

have been explored. However, most of these techniques require advanced fabrication techniques and external equipment and/or rigid sample preparation steps [125]. Therefore, developing new and more simple detection platforms for nucleic acid detection is still in need.

Various detection platforms that are more straightforward and different for the detection of nucleic acids have been reported in the literature such as electrochemical [126], electrochemiluminescent [127], enzyme-assisted [128], and optical approaches [129]. Among these technologies, optical detection methods stand out because they are simpler, accessible, and cost effective. Colorimetric and fluorometric detections are explained in more detail in the following section. In this thesis, fluorometric detection was used since it is a readily available,sensitive approach.

1.5.1.1 Colorimetric Detection

The colorimetric sensors are a class of optical sensors that are based on the visual color change in the presence of an analyte. The visual detection of DNA sequences using such sensors is referred to as colorimetric DNA detection [130]. The rapid visual response without expensive equipment has made this detection technique popular and affordable in several fields of science and technology [125]. Moreover, colorimetric sensing platforms possess straightforward, inexpensive, and sensitive analytical tool that does not require complex operations or expensive gears [131]. So far, various nanomaterials, including gold nanoparticles (AuNPs) [132], silver nanoparticles (AgNPs) [133], magnetic nanoparticles (MNPs) [134], and graphene oxide (GO) [135] have been broadly used for colorimetric detection of various nucleic acid structures. Chau and co-workers synthesized nanocomposite of platinum nanoparticles supported on reduced graphene oxide (PtNPs/rGO) for the colorimetric detection of their target ssDNA sequence. The experiment proves that when complimentary of target ssDNA is in absence, bright blue color is observed with the addition of PtNPs/rGO. However, when dsDNA formed with the addition

of complimentary ssDNA strand, PtNPs/rGO does not bind to dsDNA and results in a pale blue color. The linear dynamic range and limit of detection stated as, respectively, 0.5 – 10 nM and 0.4 nM [136]. Chen et al. created a paper based analytical apparatus for the colorimetric detection of target DNA sequence. First, MNPs were prepared with target DNA, and after the addition of $NaBH_4$ (for the preparation of DNA-supported MNPs) no color change was observed. In contrast, in the absence of target DNA, MNPs showed blue precipitate after the addition of $NaBH_4$. The limit of detection was stated as 0.228 nM and the dynamic range as between 0.0075 μM and 0.25 μM [137].

AuNPs and AgNPs are also commonly employed in optical nucleic acid sensors as both detection/sensing elements and signal indicators. Compared to AgNPs, AuNPs could exhibit stronger and more specific interactions with nucleic acids, especially with thiolated sequences resulting in a more pronounced color change that makes them better materials for nucleic acid detection [131]. Most optical sensors utilizing AuNPs are based on the aggregation behavior of AuNP in the presence of the target sequence. The color of AuNPs solution is red/ruby in the absence of any target analyte. When the target analytes/sequences are presented to AuNPs solution, the color of the solution generally changes to blue/purple due to the aggregation of the nanoparticles [138]. Li et al. performed the colorimetric detection of ssDNA with un-modified AuNPs. Target ssDNA when mixed with AuNPs and salt resulted in no visible color change. When the complimentary ssDNA was added to the mixture, the color turned into purple due to the rapid aggregation of AuNPs [132]. Jung and co-workers also used AuNPs and polymeric chain reaction-amplified thiolated nucleic acids in their colorimetric assay for diagnosing Chlamydia infection in a real human urine sample. Amplified thiolated PCR products resulted in salt (NaCl) induced aggregation of AuNPs resulting in a color change from red to blue [139].

1.5.1.2 Fluorometric Detection

Fluorometric detection platforms are also commonly employed optical sensors for rapid, simple, highly sensitive, and cost-effective detection of nucleic acid structures [140]. Changes in fluorescent signals caused by physical/biological event such as DNA hybridization can be easily recognized. Fluorescence based systems have been improved over the past decades by incorporating several nanomaterials that can convert the recognition of the interaction into changes in fluorescence as intensity and wavelength [141]. The main system of fluorometric detection method is defined as follows, reporter groups (one or more fluorophores in fluorescence-based probes which serve as surrogate recognition elements) are covalently attached or noncovalently bind to oligonucleotides. To convert hybridization or ligand binding into a fluorescent signal, fluorescent markers/labels act as transducers [142]. Generally, the traditional organic fluorescent DNA binding dyes such as TOTO (thiazole orange) or OliGreen, as well as Ethidium Bromide, are used in such platforms since their fluorescence is affected by the conformational changes of the oligonucleotides [143]. For instance, TOTO and YOYO have been used commonly in detection of PCR products by flow cytometry since the beginning of 1990s. The binding of these dyes to dsDNA results in emission at around 530 nm and 510 nm when excited at 488 nm and 457 nm, respectively [144]. Wang and Krull have shown that TOTO can also be linked covalently for selective detection of complimentary DNA in their preliminary studies. TOTO covalently bonded to probe oligonucleotide with polyethylene glycol linker. The addition of complimentary ssDNA resulted an increase in the fluorescence intensity indicating the formation of dsDNA. [145]. Yang et al. stated that TOTO-1 which is unsymmetrical cyanine dye dimer, has stronger affinity toward poly(dG) compared to polyd(A), polyd(C)and polyd(T). As a result, TOTO-1 is used for the detection of poly(ADP-ribose) polymerase-1 (PARP-1) and telomerase activity. For telomerase detection limit of detection was reported as 13 cells/mL and for PARP-1, it was stated as 0.02 U with 0.02 – 1.5 U [146].

Due to the drawbacks of these dyes, such as photobleaching, toxicity, broad emission, low absorption, and low selectivity towards different DNA secondary structures etc., other fluorescent dyes or materials such as quantum dots, up-conversion nanoparticles, and nanoclusters have been investigated and found to have great potential for use in fluorescent biosensors/imaging approaches [143]. Moulick and co-workers synthesized CdTe/ZnSe core/shell quantum dot (QD) to examine its interactions with adenine (A), guanine (G), cytosine (C) and thymine (T). The results showed that when CdTe/ZnSe core/shell QDs interact with nucleobases, red shift occurred. However, the fluorescence intensity response differed with different nucleobases. The addition of T and C increased the fluorescence intensity by 27% and 51%, respectively, when compared to CdTe/ZnSe core/shell QD's fluorescence spectra (control) and upon increasing the concentrations of T and C the fluorescence intensity enhanced further. The addition of A and G decreased fluorescence intensity by 25% and 82%, respectively, when compared to the control and increasing the concentrations of A and G caused further decrease in the fluorescence intensity. Limit of detection for minimum DNA concentration reported as 500 pM [147]. Kim et al., reported a specific DNA detection method by using the combination complex of magnetic beads and CdSe-ZnS quantum dots. Briefly, in their study, FL signal produced by QDs and magnetic beads were used to isolate and concentrate the produced FL signal and CdSe-ZnS quantum dots (conjugated with streptavidin) were applied as signal producer. A sandwich hybridization mechanism between streptavidin- conjugated quantum dots and the magnetic beads was reported to be the result of the presence of the target DNA structure. In other words, the FL signal was proportional to the concentration of the target strand and no FL signal was reported in the case of non-complementary DNA structures used in this study. Also, according to the obtained results, the use of magnetic beads caused a remarkable improvement in the sensitivity of the proposed approach by more than hundred-fold (as low as 0.5 pM). In all, this research study has opened new avenues and established a reliable protocol for the cases where large volume of samples is required for analysis [148]. And, recently Bilgen and co-workers in our lab reported a selective and sensitive

probe for the detection of Pu22 G4 rather than a ssDNA or dsDNA using a different fluorescent dye. This study relies on the effective FRET (Förster resonance energy transfer) mechanism between gold nanoparticles and azacyanine5 dye (a small molecule ligand) and a tree step (off-on-off) sensing strategy. Briefly, upon the addition of azacyanine5 to the AuNPs solution a distinct fluorescence quenching (around %85) was reported followed by a clear fluorescence recovery (on step) after the addition of L-cysteine to the conjugated probe system and an obvious fluorescence restoration upon the addition of the target G4 model structure. The obtained results demonstrated that the developed probe could selectively detect/discriminate G4 DNA structure rather than ssDNA and other secondary structures. The linear range for the developed method was reported to be 0.032 – 0.347 μM with a limit of detection as low as 12.6 nM [149].

In this thesis study, due to their ease of synthesis, high fluorescence quantum yield and low toxicity, CQDs are selected as the detection probe in the fluorometric detection of HER2 G4 oligonucleotide.

1.6 HER2 Detection Techniques

As mentioned above, since HER2 overexpression is directly linked to invasive breast cancer [100], and its detection became important in cancer research in the last decades. Till now, various powerful techniques have been reported in the literature for the detection of HER2. For example, Hartati et al. [150] proposed a HER2 biomarker detection technique based on electrochemical immunosensing by using cerium oxide – monoclonal antibody bioconjugate with 0.001–20.0 ng/mL linear dynamic range (LDR) and 34.9 pg/mL of limit of detection (LOD). In addition, Rossi et al. [151] constructed a silica nanospheres-based system and applied it for the fluorometric detection of HER2 with 1 ng/mL LOD and 1.0–10,000 ng/mL LDR under optimal conditions. Another electrochemical-based technique was published in 2020 by Ehzari et al. [152]. They used Fe_3O_4@TMU-21, generated by using methacrylic acid to coat Fe_3O_4 nanoparticles, for the detection of HER2. LOD of the

developed system was reported to be 0.30 pg/mL and the LDR ranged from 1.0 pg/mL to 100 ng/mL. The studies reported in the literature are given in Table 1. These studies mostly aimed direct HER2 protein detection. There are also several studies developed to detect HER2 at DNA and RNA levels. For example, recently Slamon and co-workers reported a Northern blot assay to detect HER2 RNA in frozen breast cancer specimens. In this study, the authors reported that the proto-oncogene HER -2/neu is amplified in 25-30% of human primary breast cancers and that this change is linked to disease behavior. In addition, the biology of HER-2/neu in breast and ovarian cancer shared a number of similarities, such as similar frequency of amplification, a direct connection between amplification and overexpression, evidence of tumors with overexpression without amplification, and the relationship between gene alteration and clinical outcome [153]. According to the literature, the described method (Northern Blot) has some disadvantages, such as the fact that RNA molecules are easily and frequently degraded in tissues and affect the quality of the obtained information. In addition, it is a labor-intensive procedure and does not allow exclusive determination of HER2 status in cancer cells [154]. Other studies in the literature have used the Southern blot technique to determine HER2 gene amplification in breast cancer samples [155]. In most of these works, the DNA is digested with a restriction enzyme after DNA extraction from frozen breast cancer tissue. The digested DNA fragments are then separated by the gel electrophoresis technique. After DNA denaturation, the DNA samples are transferred from the gel to a membrane and hybridized with a radiolabeled HER2 ssDNA probe. The labeled HER2 ssDNA probe hybridizes with the HER2 ssDNA sequence based on strand annealing between complementary ssDNA molecules. The labeled HER2 sequence is then could be visualized by autoradiography[156]. Although this technique is very reliable, it cannot be used in routine diagnostics because it is time-consuming and requires a large amount of DNA. In addition, this technique does not allow morphologic preservation of the tissue and thus does not allow evaluation of the histologic features of the tumor. Because unamplified non-neoplastic cells in the tumor cannot be isolated from cancer cells, the results obtained

may underestimate the true HER2 gene amplification of the sample due to a dilution effect [154]. Although these methods are excellent approaches for the detection/determination of HER2 in diverse matrices, there is still a need to develop simpler, more straightforward, more sensitive, and cost-effective analytical methods. In this thesis, based on the studies of Cui et al., instead of detecting HER2 protein, we thought that the G4 structure, formed in the promoter region of HER2 gene, could also act as a biomarker [109]. And for this reason, we developed a platform for the detection of the HER2 G4 structure. To the best of our knowledge, the proposed system here is the first ratiometric study for the sensitive and selective detection of HER2 G4 structure that is taking advantage of CQDs. We believe that this newly developed, facile, and straightforward method can initiate the development of new techniques for the routine analysis of HER2 G4 structures.

Table 1. Summary of previously reported methods for the detection of various HER2.

METHOD	SENSING STRATEGY	SENSING ELEMENT/ WORKING SURFACE	TARGET	MATRIX	LOD	LDR	REF
PEC sensor[1]	EC[2]	HCNT/AuNPs[3]	HER2 biomarker	Human serum sample	0.08 pg/mL	$5x10^{-4}$ - 1 ng/mL	[157]
PEC sensor	EC	WS_2NW/TM[4]	HER2 biomarker	Breast cancer patients' serum	0.36 ng/mL	0.5 – 10 ng/mL	[158]
PEC sensor	EC	HCNT[5]	HER2	Healthy human serum sample	0.026 pg/mL	$1x10^{-3}$ – 1 ng/mL	[159]

Table 1. (Continued)

DPV[6]	EC	MIP[7]	HER2 – ECD[8]	Spiked human serum sample	1.6 ng/mL	10 – 70 ng/mL	[160]
DPV	EC	CdSe@ZnS QDs[9]	HER2 - ECD	Spiked human serum sample	2.1 ng/mL	10 – 150 ng/mL	[161]
DPV	EC	GE/TDN – aptamer/MCH[10]	HER2 biomarker	Serum sample	0.08 ng/mL	0.1 – 100 ng/mL	[162]
SWV[11]	EC	Ab2-PBS QDs[12]	HER2 biomarker	Spiked human serum sample	0.028 ng/mL	1 – 100 ng/mL	[163]
SWV	EC	LSG-AuNS-MIP[13]	HER2 protein	Spiked undiluted serum sample	0.43 ng/mL	1 – 200 ng/mL	[164]
SWV	EC	Polycytosine DNA	HER2 biomarker	Breast cancer patients' serum	0.5 pg/mL	0.001 – 1 ng/mL	[165]
DPV and CA[14]	EC	MnO_2 NSs/AuNPs[15]	HER2 biomarker	Human serum	16.7 and 33.3 fg/mL	50 fg/mL - 100 ng/mL and 100 fg/mL-100 ng/mL	[13]

Table 1. (Continued)

EIS[16]	EC	ErGO – SWCNT /AuNP[17]	HER2 protein	Healthy and breast cancer patients' serum sample	50 fg/mL	0.1 pg/mL – 1 ng/mL	[166]
(EOD) – LIF[18]	FLM[19]	Si photodetector	HER2 protein	Hela cells	$3x10^2$ M	0.01 – 100 nM	[167]
Lateral Flow Assay	CLM[20]	Aptamer/AuNP nanocomplex	HER2 protein	10% humans serum sample	10 nM	0 M – 99 nM	[168]
Catalytic Amplification -Based Assay	CLM	(MSN) – AuNCs – anti – HER2[21]	HER2+ breast cancer cell	HER2+ breast cancer tissue	10 cell	10 – 1000 cell	[169]
(NIR) – FRET[22]	FLM	MnCuInS/ZnS @BSA QDs[23]	HER2 protein	Human serum sample	1 ng/mL	2 – 100 ng/mL	[170]
Serum HER2 – ECD Test[24]	FLM	Cy5 – HB5[25]	HER2 – ECD	Serum	-	1.5 µg/L – 24 µg/L	[171]
"Turn–on" fluorescence	FLM	AgNCs[26]	HER2 biomarker	Breast cancer patients' serum sample	0.0904 fM	8.5 fM – 225 fM	[172]
FRET[27]	FLM	ADAPTs – QDs[28]	HER2	Serum	8 ng/mL	7 ng/mL – 3000 ng/mL	[173]

Table 1. (Continued)

Fluorescence	FLM	Pt NCs[29]	HER2	SK-BR3 breast cancer cell	-	-	[174]
DPV	EC	antiHER2/ APMS – Fe_3O_4[30]	HER2	Serum	2 x 10^{-5} ng/mL	5 x 10^{-4} ng/mL - 50 ng/mL	[175]
Fluorescence	Ratiometric	N, S-CQD	HER2 G-Quadruplex	Breast cancer cell	0.22 μM	0.27 μM – 6.02 μM	This work

[1]PEC: Photoelectrochemical sensor
[2] EC: Electrochemical
[3] HCNT/AuNPs: Hexagonal carbon nitride tubes / Gold nanoparticles
[4] WS_2NW/TM: Tungsten sulfide nanowire array on Ti mesh
[5] HCNT: Hexagonal carbon nitride tubes
[6] DPV: Differential pulse voltammetry
[7] MIP: Molecularly imprinted polymer
[8] HER2-ECD: HER2 extracellular domain
[9] CdSe@ZnS QDs: CdSe/ZnS Core-Shell quantum dots
[10] GE/TDN – aptamer/MCH: Gold electrode/Tetrahedral DNA nanostructure/6-mercepto-1-hexanol
[11] SWV: Square wave voltammetry
[12] Ab2–PBS QDs: Lead sulfide quantum dots conjugated secondary HER2 antibody
[13] LSG–AuNS – MIP: Laser scribed graphene-gold nanoclusters-molecularly imprinted polymer
[14] CA: Chronoamperometry
[15] MnO_2 NSs/AuNPs: MnO_2 nanosheets/gold nanoparticles
[16] EIS: Electrochemical impedance spectroscopy
[17] ErGO – SWCNT/AuNP: Graphene oxide and single-walled carbon nanotubes/Gold nanoparticles
[18] (EOD) – LIF: Electroosmotic driven laser-induced fluorescence
[19] FLM: Fluorometric
[20] CLM: Colorimetric
[21] (MSN) – AuNCs – anti – HER2: Gold nanoclusters entrapped in mesoporous silica nanoparticles with inclusion of target specific HER2 antibodies
[22] (NIR) – FRET: Near-infrared Förster resonance energy transfer
[23] MnCuInS/ZnS@BSA QDs: MnCuInS/ZnS encapsulated bovine serum albumin nanoparticles
[24] Serum HER2 – ECD Test: Serum HER2 - extracellular domain test
[25] Cy5 – HBS: Cy5 labeled HB5 aptamer
[26] AgNCs: Silver nanoclusters
[27] FRET: Förster resonance energy transfer
[28] ADAPTs – QDs: Histidine tagged albumin binding domain derived affinity proteins self-assemble to zwitterionic ligand coated quantum dots
[29] PtNCs: Platinum nanoclusters
[30] antiHER2/APMS – Fe_3O_4: 3-aminopropyltrimethoxysilane coated magnetite nanoparticles with antibody

1.7 Aim of the Study

As it mentioned in the introduction part of this thesis, HER2 overexpression plays an important role in breast cancer. And, in clinical practice, a variety of methods have been developed to assess the presence of HER2 as the biomarker in breast cancer specimens at the RNA, DNA, and protein levels [154]. Furthermore, Food and Drug Administration approved several different procedures to examine HER2 status, including in situ hybridization [176], fluorescence in situ hybridization [177] and immunohistochemistry [178]. However, there is still a disagreement about the best approach for determining the presence of HER2 breast cancer specimens because each methodology has advantages and limitations of its own [179]. Additionally, in the literature, a variety of in-vitro techniques presented as electrochemical, fluorometric and colorimetric approaches. The mentioned methods are excellent detection platforms for finding or determining the presence of HER2 in a variety of matrices, however developing more straightforward, simple, sensitive, and affordable analytical techniques are still in need.

Recently, studies suggested that the G4 structure observed in the HER2 promoter region could act as a possible target as a therapeutic approach in breast cancer. Ciu et al. has shown that the G4 formation in the promoter region of HER2 is one of the factors in the regulation of HER2 by constructing wild-type (G4 can form) and mutant (G4 cannot form) plasmids. The study proved that HER2 promoter activity decreased by 40% with wild-type plasmid whereas upregulated by mutant plasmid [109]. Inspired by the aforementioned considerations, we hypothesized that the detection of HER2 G4 could be a possible biomarker and the direct detection of HER2 G4 structure can be implemented in early detection of breast cancer. To our knowledge, the detection of HER2 G4 structure has not yet been studied in detail. Consequently, we aimed to develop a simple ratiometric detection platform for HER2 G4 by taking advantage of the N,S co-doped CQDs and Thioflavin T fluorescent dye which is known to be specifically binding to G4 structures [180]. The developed sensing system is thought to be relatively low-cost, facile, non-toxic,

fast, environmentally friendly, effective, and sensitive to HER2 G4. We believe that it could provide new, alternative avenues to breast cancer early detection.

CHAPTER 2

MATERIALS AND METHODS

2.1 Materials and Chemicals

All chemicals and reagents (tabulated in Table 2) were used as received without further purification. Millipore water (Milli-Q, 18.2 MΩ cm^{-1}) was used to prepare all, buffers and samples (tabulated in Table 3).

Table 2. The used chemicals/materials and reagents.

Chemicals	Sources
L-Cysteine Hydrochloride Anhydrous	Wood Dale (USA)
Citric Acid ($C_6H_8N_2$)	Merck (Darmstadt, Germany)
Sodium Hydroxide (NaOH)	Sigma–Aldrich (St. Louis, USA)
Thioflavin T ($C_{17}H_{19}ClN_2S$)	Sigma–Aldrich (St. Louis, USA)
Potassium Chloride (KCl)	Sigma–Aldrich (St. Louis, USA)
Dipotassium Hydrogen Phosphate (K_2HPO_4)	Merck (Darmstadt, Germany)
Potassium Dihydrogen Phosphate (KH_2PO_4)	Merck (Darmstadt, Germany)
Quinine Hemisulfate Salt Monohydrate ($C_{20}H_{24}N_2O_2 \cdot 0.5H_2O_4S \cdot H_2O$, ≥98.0%)	Sigma-Aldrich (St. Louis, USA)
Sulfuric Acid (H_2SO_4, 96%)	Carlo Erba Reagents

Table 3. The sequences of oligonucleotides, examined in this study.

Abbreviations for the nucleic acids	**Sequences**	**Extinction coefficient (ε) [L/(molecm)**	**Sources**
dA_{32}	5'-AAA AAA AAA AAA AAA AAA AAA AAA AAA AA-3'	ε_{260}= 387,400	Integrated DNA Technologies (Dresden, Germany)
dT_{32}	5'-TTT TTT TTT TTT TTT TTT TTT TTT TTT TT-3'	ε_{260}=259,800	Integrated DNA Technologies (Dresden, Germany)
RB	5'-CGG GGG GTT TTG GGC GGC-3'	ε_{260}=164,700	Integrated DNA Technologies (Dresden, Germany)
Pu_{22}	5'-CGG GGC GGG CCG GGG GCG GGG T-3'	ε_{260}=178,400	Integrated DNA Technologies (Dresden, Germany)
C-MYC	5'-TGG GGG AGG GGT GGG GGA GGG GTG GGG GAA AGG G-3'	ε_{260}=279,900	Integrated DNA Technologies (Dresden, Germany)
VEGF	5'-GGG CGG GCC GGG GGC GGG GTC CGG GCG GGG CGG GAG-3'	ε_{260}=338,200	Integrated DNA Technologies (Dresden, Germany)
BCL – 2	5'-AGG GGC GGG CGC GGG AGG AAG GGG GCG GGA GCG GGG C-3'	ε_{260}=368,200	Integrated DNA Technologies (Dresden, Germany)

Table 3. (Continued)

K – RAS	5'-GGG AAG AGG GAA GAG GGG GAG-3'	ε_{260}=232,800	Integrated DNA Technologies (Dresden, Germany)
HER2	5'-AGG AGA AGG AGG AGG TGG AGG AGG AGG GC-3'	ε_{260}=315,900	Integrated DNA Technologies (Dresden, Germany)
Poly (A)		ε_{258}=9,800	Boehringer Mannheim GmbH (Germany)

2.2 Instrumentation

Absorbance spectra of the samples were recorded via a double beam JASCO V-730 UV-vis spectrophotometer (Easton, MD, USA) using a 10 mm quartz cell. A Cary Eclipse fluorescence spectrophotometer (Santa Clara, CA, USA) equipped with a Cary single cell Peltier (Agilent Technologies) temperature control unit was used to record all fluorescence emission spectra of the samples between 410 and 700 nm. To examine the size and morphology of the synthesized N,S-CQDs, and their morphological change upon addition of HER2 G4 structure, transmission electron microscopy micrographs were captured using a JEOL JEM-2100F (Akishima, Tokyo, Japan) HRTEM instrument operating at an accelerating voltage of 200 kV at METU Central Laboratory. The samples were carefully placed on commercially available carbon-coated copper grids, then air dried for 24 hours at ambient temperature to allow water/solvent to completely evaporate before TEM analysis. The samples' CD spectra were collected using a JASCO J-1500 spectropolarimeter equipped with CTU-100 Circulating Thermostat Unit (Easton, USA) in the wavelength range of 220 to 500 nm with scan rate of 100 nm/min and data of

integration of 4 sec. In order to conduct dynamic light scattering (DLS) studies, Rigaku Ultima-IV X-Ray Diffraction equipment was used by taking an operatic service from Ahvaz Jondishapur University of Medical Science (Ahvaz, IRAN). A laser diffraction particle analyzer (Nanotrac wave II; Microtrac, Krefeld, Germany) was used to determine the size distribution of the synthesized N,S-CQDs in aqueous solution at 23°C. For pH adjustments and buffer preparation, a Mettler Toledo Seven CompactS210 pH meter (Greifensee, Switzerland) was used. To eliminate the extra or unreacted chemicals and to purify the synthesized N,S-CQDs, a Hermle Z 326 K centrifuge (Hermle Labortechnik, Wehingen, Germany) was employed. An Apple iPhone 12 Pro Smartphone was used to take the digital photographs of the samples.

2.3 Synthesis of N, S-CQDs

To synthesize N,S-CQDs, a well stabilized solid-phase thermal method in the literature was followed with minor modifications [181]. Scheme 1 demonstrates the synthesis procedure of N,S-CQDs. Briefly, 2.0 g citric acid and 1.0 g L-cysteine were used as carbon and heteroatom sources. The mixture of citric acid and L-cysteine was pulverized by grinding and placed in a Teflon-lined stainless-steel autoclave before being heated in a muffle furnace at 200°C for 3 h. After letting allowed to cool down to room temperature, the volume of the solution was increased to 50.0 mL with deionized water and the pH of the resulting solution was adjusted to 7.0 with 1.0 M NaOH [182]. In order to get rid of the unreacted precursors and large particles, the solution was centrifuged at 7000 rpm for 20 min and 8000 rpm for another 20 min using a Hermle Z 326 K centrifuge. Following the centrifugation, the solution was filtered with 0.22 μm syringe filters with a cut-off of 45 μm (Millipore Cork, Ireland). Finally, the product was dialyzed against H_2O for 8 hours using mega dialysis kit (Sigma, Pur-A-Lyzer, 1000 Da) before freeze-drying (conditions: 0.1 mbar, -45°C, 48 h). A yellowish-brown color N,S-CQDs powder was obtained as the final freeze-dried product. The synthesized N,S-CQDs were characterized by DLS,

TEM, fluorescence spectroscopy, UV-vis spectroscopy, X-ray diffraction and X-ray photoelectron spectroscopy.

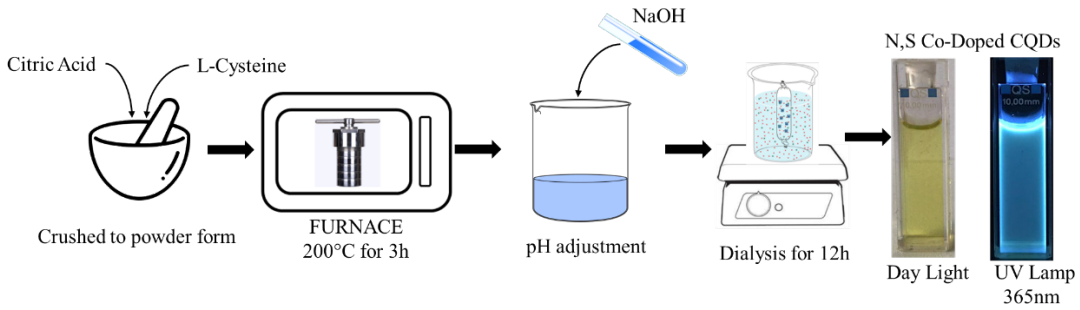

Scheme 1. Schematic illustration of the synthesis procedure of N,S-CQDs.

2.4 Preparation of the Probe and Analyte

Probe was prepared as following: 2.5 ppm 2500 µL of N, S-CQDs aqueous solution and 250.0 µL 500.0 µM aqueous solution of Thioflavin T (ThT) fluorescent dye were vortex-mixed for 5 min at 4140 rpm at room temperature. A sample only containing 2.5 ppm 2500 µL of N, S-CQDs and 250.0 µL H_2O was also prepared as a control. The prepared N,S-CQDs and N,S-CQDs/ThT mixture were also characterized by fluorescence spectroscopy and high-resolution transmission electron microscopy. All DNA samples were prepared as follows. First, all oligonucleotides obtained in freeze dried form from IDT DNA (Germany, Europe) were dissolved in 1000.0 µL H_2O to prepare the stock solutions. The concentrations of the stock solutions were determined using their extinction coefficient (ε) value provided by the supplier (IDT) using UV-vis absorbance. Next, the nucleic acid solutions at desired concentrations (75 µM and 100 µM) were prepared in K-Phosphate buffer (100 mM, pH = 7.0, containing 70 mM KCl) and were annealed by heating at 95 °C for 5 min in a water bath followed by cooling down to room temperature overnight to ensure the formation of the proper secondary structure before conducting the experiments.

Duplex nucleic acid structure ($dA_{32}dT_{32}$) was obtained by mixing the dA_{32} and dT_{32} nucleic acids in equimolar ratios.

2.5 Optimization Studies

Several factors affecting the detection performance including N,S-CQDs concentration, ThT concentration, pH, time, and temperature were investigated and optimized. Optimization experiments were performed using a one-factor-at-a time approach. Following that, the optimum conditions were used for all further experiments.

For fluorometric measurements, unless otherwise stated, parameters were set as following. The excitation wavelength was 350 nm, the emission spectra was recorded from 360 nm to 650 nm, the emission and excitation slits were both 5.0 nm, the operation voltage was 625 V and the scan rate was 12,000 nm/min.

In so doing, the fluorescence quantum yield (FL QY) of the N,S-CQDs were determined [183]–[185]. The standard sample (Quinine Sulfate) was dissolved in 0.10 M sulfuric acid and the synthesized N,S-CQDs were dissolved in H_2O and absorbance spectra of standard sample (quinine sulfate) and N,S-CQDs with different concentrations (0.00, 0.02, 0.04, 0.06, 0.08 and 0.10 Abs) were collected at 350 nm. Following the absorbance measurements, fluorescence spectra of the same samples were recorded. Eqn. 1 was used for the quantum yield% calculation of the N,S-CQDs

$$Q_x = Q_s \, x \, (Grad_x / Grad_s) \, x \, (\eta_x^2 / \eta_s^2) \text{ x } 100 \qquad \text{Eqn. 1}$$

Where Q is the fluorescence quantum yield, $Grad$ is the gradient from the plot of integrated fluorescence vs. absorbance, and η is the refractive index of solvents (subscript s represents standard solution and subscript x represents the N,S-CQDs) [186].

The influence of N,S-CQDs concentration was monitored by altering the N,S-CQDs concentration from 2.5 to 10.0 ppm (2500 μL) while the ThT stock concentration was kept constant (1000 μM).

The effect of the ThT concentration on the sensing performance of the proposed method was observed by titration of 2.5 ppm 2500 μL N,S-CQDs with varying ThT solutions. The concentration of ThT solutions were tested between 500 μM to 4000 μM and the best concentration was selected accordingly.

N,S-CQDs with pH values between 3.0-9.0 (3.0, 5.0, 7.0, and 9.0) were prepared separately using NaOH and HCl solutions (0.1 M) to determine the changes in the FL emission profile of the synthesized N,S-CQDs upon pH changes. Also, the optimum ThT concentration was added to the mentioned pH-adjusted N,S-CQDs solutions for the detection the effect of pH on N,S-CQDs/ThT.

The selectivity of the proposed N,S-CQDs/ThT probe towards different nucleic acid structures, such as single-stranded nucleic acids (Poly A, dA_{32}, dT_{32}), double-stranded nucleic acid ($dA_{32}dT_{32}$), and other available G4 structures (RB, Pu22, C-MYC, VEGF, BCL2, K-RAS,) was examined using the mentioned nucleic acid structures instead of HER2 G4 where the final concentrations of the nucleic acids were 9.84 μM. Fluorescence response of HER2 G4 structure was also examined at a lower concentration of 7.37 μM to show that the system's response to even lower concentrations of HER2 G4 compared to other structures under the same conditions.

HER G4 stock solution (75 μM) was added to probe and vortex-mixed for 5 min. For the time-dependent qualitative test the fluorescence response of the probe system after the addition of HER2 G4 was monitored at 1, 3, 5, 10, 15, 20, 30, 45 and 60 min (under optimal circumstances).

The optimal temperature of the system was investigated with varying the temperature of the sensing platform from 5°C to 70°C with 5°C increments. For the control experiment, N,S-CQDs fluorescence response with varying temperature from 5°C to 70°C was investigated under the same conditions.

All experimental sets were conducted in triplicate at ambient condition except for the QY% calculations and pH adjustments.

To assess the quantitative properties of the N,S-CQDs/ThT probe, calibration plots of $F_1/(F_0-F_2)$ vs. 1/[Q], and $F_1/(F_0-F_2)$ vs. [HER2 G4] were used. $F_1/(F_0-F_2)$ vs. time (min) was used for time optimization.

Here [Q] represents the concentration of ThT, F_0 is the corresponding fluorescence response of N,S-CQDs at 406 nm in the absence of ThT and target analyte addition, F_1 and F_2 represent the fluorescence response at 494 nm and 406 nm of N,S-CQDs/ThT in the presence of the target analyte (HER2 G4).

Finally, fluorometric titration tests were conducted under optimal conditions to examine the sensing performance (sensitivity and linear range) of the assay. Limit of detection (LOD) was calculated using LOD = 3.3 x (S_b/a) equation. Where, 'S_b' denotes the intercept's standard error and 'a' denotes the calibration curve's slope.

CHAPTER 3

RESULTS AND DISCUSSION

3.1 Characterizations of N,S-CQDs

N,S-CQDs were synthesized via the solid-phase thermal synthesis method in a muffle furnace at 200°C mainly due to the availability, and simplicity of the method. The details of the synthesis are given in section 2.3. To gain further insight into the size, phase, and elemental composition of the synthesized N,S-CQDs particle size distribution Dynamic Light Scattering (DLS), X-ray diffraction (XRD), and X-ray photoelectron spectroscopy (XPS) analyses were conducted. High resolution transmission electron microscopy (HR-TEM) images were also acquired for morphological analysis.

According to the DLS analysis, depicted in Figure 8, 83.09% of the synthesized particles had a size of 10 nm or smaller (details are given in Appendix B, Figure 23). Qie et al. reported a very similar particle size analysis profile for the N,S-CQDs that they synthesized from citric acid and thiourea under optimized conditions [187]. XRD analysis revealed that the synthesized N,S-CQDs have amorphous structures with a broad peak, 2θ ranging from about 10 to 30 degrees (see Figure 9). This is very similar to the amorphous structure of N,S-CQDs synthesized by Wang and co-workers from ascorbic acid and ammonium persulfate with a broad peak centered at 2-theta at 24° [188]. XPS was performed to further investigate the surface composition and chemical state of N,S-CQDs (Figure 10). The full-scan XPS spectrum shows that the sample consists of the elements C, N, S, O. Four major peaks observed in the HR-XPS survey spectrum shown in Figure 10 at 162.4, 283.4, 399.1 and 529.5 eV belongs to Sulfur (S) 2p, carbon (C) 1s, nitrogen (N) 1s, and oxygen (O) 1s, respectively confirming the presence of sulfur, carbon, nitrogen and oxygen elements, being in perfect agreement with similar reports in the literature

[189]. The HR-TEM images of samples including N,S-CQDs (a and b, scale bars: 10 nm and 20 nm, respectively) is shown in Figure 11. According to the captured micrographs, N,S-CQDs have spherical morphology and narrow size distribution below 10 nm, which is again in a perfect agreement with our DLS results and the published reports in the literature [190].

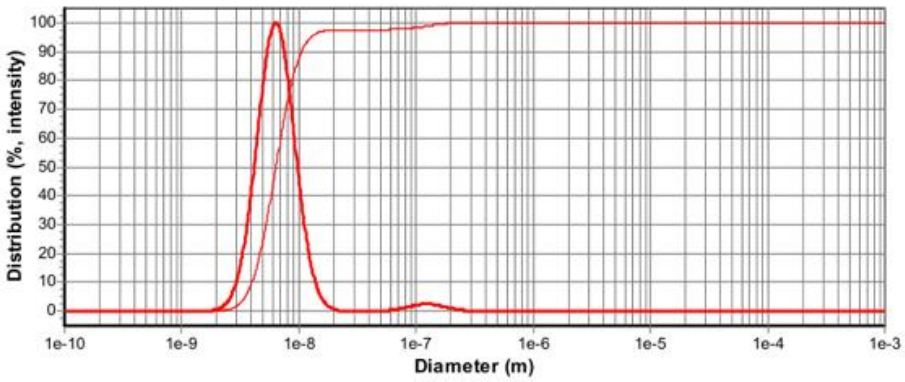

Figure 8. Particle size distribution measurement of synthesized N,S-CQDs.

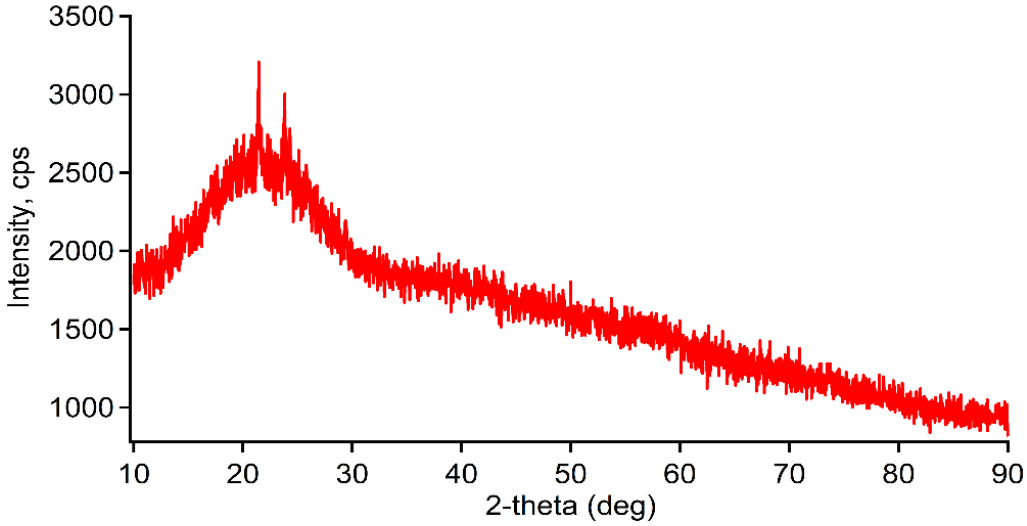

Figure 9. XRD analysis of synthesized N,S-CQDs

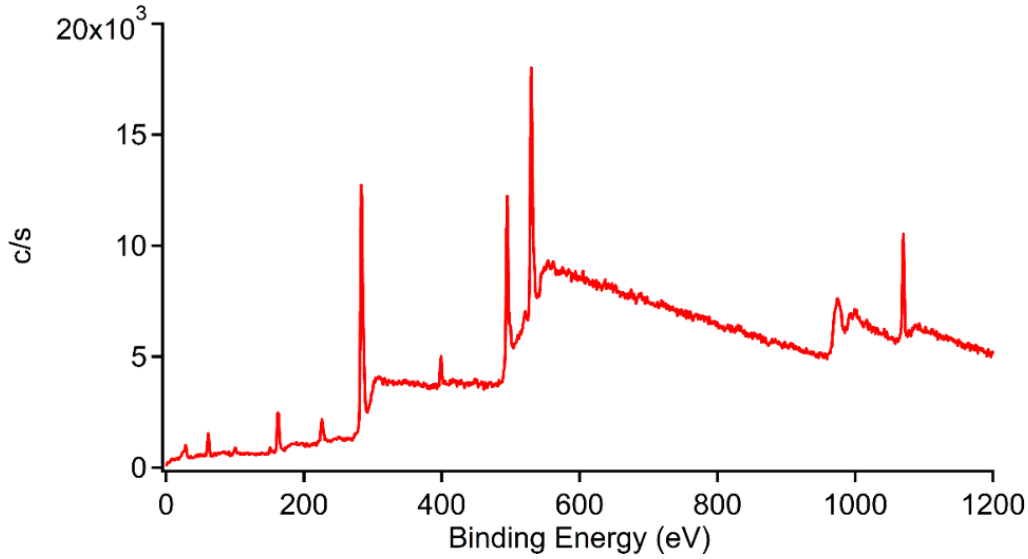

(a)

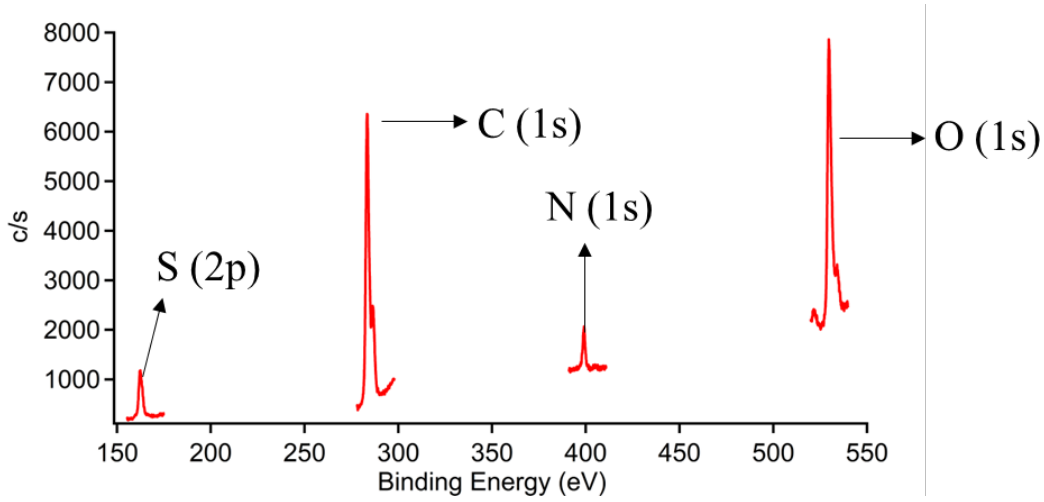

(b)

Figure 10. (a) XPS and (b) high-resolution XPS (HR-XPS) analysis of synthesized N,S-CQDs.

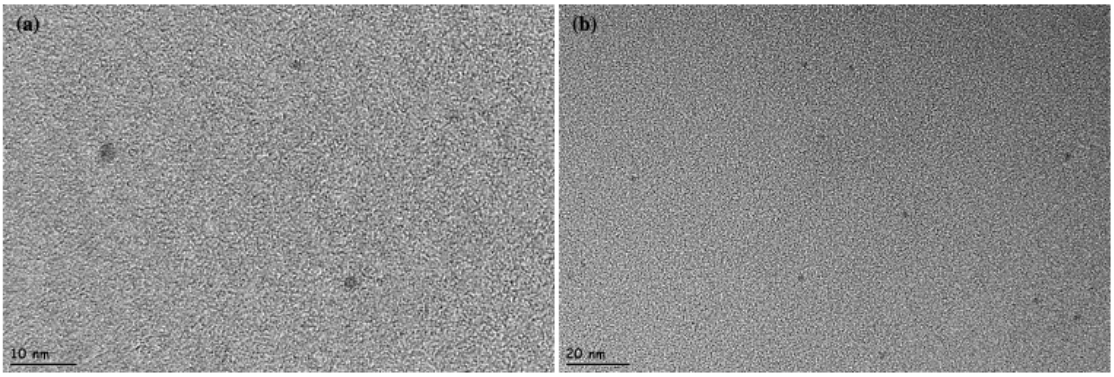

Figure 11. HR-TEM micrographs of the synthesized N,S-CQDs (a and b are at different magnifications).

3.2 Quantum Yield Measurements of Synthesized N, S-CQDs

In order to determine the excitation, and emission wavelengths of N,S-CQDs, the synthesized samples with a known concentration (50 ppm) were excited at different wavelengths (from 300 nm to 400 nm, increased by five units) and the corresponding emission spectra were collected between 300 and 600 nm for the all samples. From the obtained results (Figure 12), since the emissions were relatively high, the excitation wavelength of the synthesized N,S-CQDs was selected to be as 350 nm. The excitation wavelength of 350 nm was used in further experiments.

The efficiency of converting absorbed light into emitted light, in other words the ratio of the number of photons emitted to the number of photons absorbed, has been termed by the quantum yield (QY) and even at low concentrations, fluorophores with a high QY often emit strong fluorescence [191], [192]. N,S-CQDs with high quantum yield exhibit robust luminescence [193]. In order to determine the fluorescence quantum yield of the synthesized N,S-CQDs, Quinine Sulfate was used as the standard sample. According to the literature, to diminish the effects of re-absorption, inner filter effects, and other factors such as aggregation, the relative determination of QY relies on the measurement of samples and standards with low absorbances below 0.10. Accordingly, the absorbance values for all samples and

standards were all kept below 0.10 [194]. In order to prepare samples with different concentrations, Quinine Sulfate stock was dissolved in 0.10 M sulfuric acid and the synthesized N,S-CQDs were dissolved in H_2O [195].

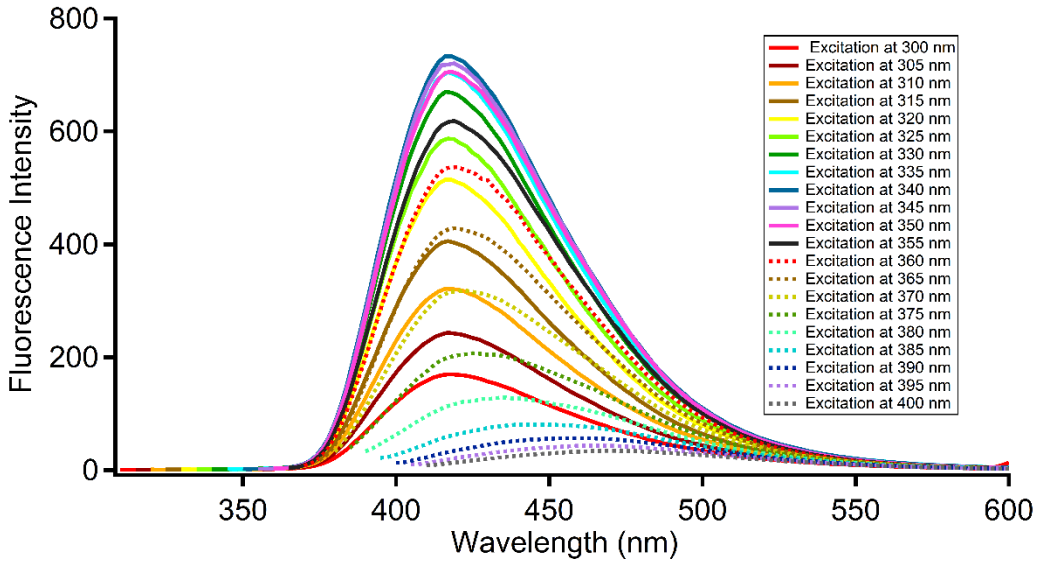

Figure 12. Fluorescence intensity spectra of N,S-CQDs excited at varying excitation wavelengths.

Quantum yield measurements were conducted by the comparative method according to the literature [196]. To calculate the fluorescence quantum yield of the synthesized N,S-CQDs, UV-vis spectrophotometer was used to adjust the absorbance values of the both N,S-CQDs and Quinine sulfate samples at 350 nm (Appendix C, Figures 25-28). Quinine sulfate (QY=0.54 in 0.1 M H_2SO_4 [197]) was selected as the standard sample since its excitation/emission wavelengths are in the same range as the synthesized N,S-CQDs (λ_{Ex} : 350 nm, λ_{Em} : 360 nm). Fluorescence emission spectra of the samples were recorded between 360 nm and 650 nm with 625 V and the excitation and emission slits were set to 5 nm. Eqn.1 was used to calculate the QY% of the N,S-CQDs.

$$Q_x = Q_s \, x \, (Grad_x / Grad_s) \, x \, (\eta_x^2 / \eta_s^2) \text{ x } 100 \qquad \text{Equation 1}$$

Where Q is the fluorescence quantum yield, *Grad* is the gradient from the plot of integrated fluorescence vs. absorbance, and η is the refractive index of solvents (subscript s represents standard solution and subscript x represents the N,S-CQDs) [186]. Figure 13 depicts the integrated FL intensity vs. absorbance for both standard and N,S-CQDs samples. Form the obtained results, fluorescence quantum yield is calculated as 34 using the line equations of the standard sample and N,S-CQDs.

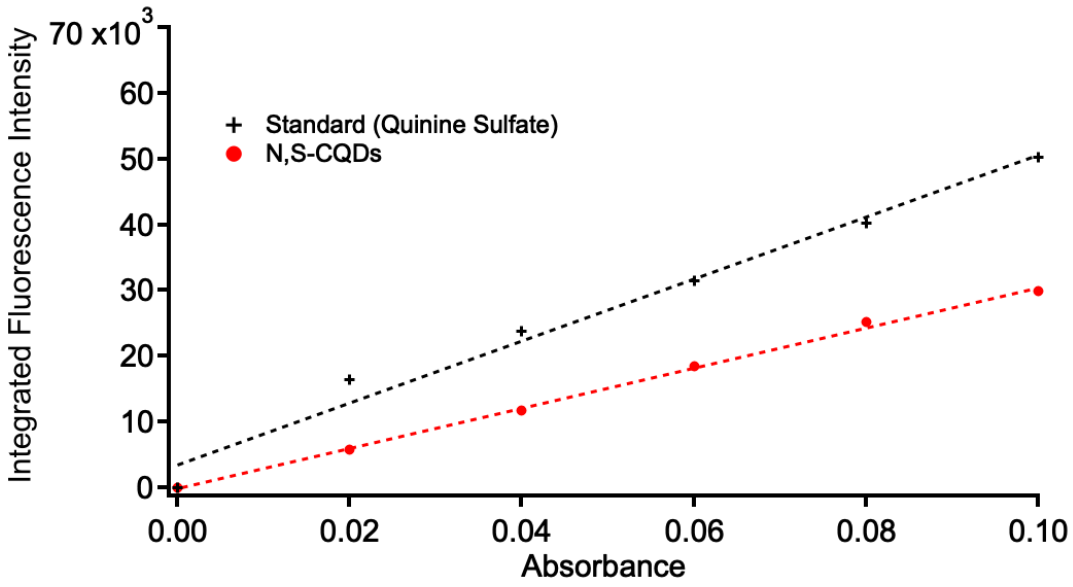

Figure 13. Integrated fluorescence intensity vs. Absorbance graph of standard sample and N,S-CQDs. The lines equations were calculated as y = 9441.4x - 6020.1 and y = 6118.4x - 6258.3 for standard sample and N,S-CQDs, respectively.

3.3 Fluorometric Detection of HER2 G-Quadruplex Using Conjugated N,S-CQDs and Probe

Figure 14 displays the stepwise fluorometric response of the developed probe towards HER2 G4 structure under the optimized conditions along with the digital luminescence images under day light and UV illumination at 365 nm. As it can be seen from the black trace in Figure 14 (a), N,S-CQDs exhibits an intense, broad, and distinct fluorescence response when excited at 350 nm with a maximum emission

wavelength of approximately 420 nm. When the N,S-CQDs and ThT was vortex-mixed before the addition of the HER2 G4 for the quantitative detection, a significant fluorescence quenching is observed with a shift in the maximum emission wavelength to 460 nm, and a very broad shoulder with a local maximum around 406 nm as shown by the grey line in Figure 14 (a). The addition of HER2 G4, restored the fluorescence intensity of the probe resulting in a local maximum emission at 406 nm, and a new maximum emission at 494 nm after 5-minutes of interaction as can be seen from red trace (Figure 14 a).

As displayed in Figure 28 (Appendix C), the red peak with an emission at 494 nm is due to the interaction between ThT and HER2 G4. ThT gives rise to very weak fluorescence intensity by itself in the absence of HER2 G4 under these conditions (Appendix D, Figure 29, black spectrum). The titration of HER2 G4 onto N,S-CQDs/ThT solution results in a clear increase in the intensity of the peak at 494 nm. In the meantime, an increase in fluorescence intensity was also observed at 406 nm with the gradual addition of HER2 G4 to the probe solution. The peak at 406 nm is thought to be representing the N,S-CQDs, whose interactions with ThT were weakened in the presence of HER2 G4, resulting in an increase in intensity at 406 nm (Appendix C, Figure 30). The titration of ThT onto N,S-CQDs solution was also performed as the control experiment (Appendix C, Figures 31-33). As can be seen in Figures 31-33, only a decrease in the fluorescence intensity of the N,S-CQDs was observed upon addition of ThT. The fluorescence of N,S-CQDs was clearly quenched by ThT, confirming the presence of interactions between N,S-CQDs and ThT. In addition, the broad emission of peak of N,S-CQDs with a maximum emission wavelength at 420 nm is converted into a broad peak with a shoulder with a maximum emission wavelength at 460 nm, and a local maximum emission wavelength at 406 nm. Overall, these results clearly demonstrate the interactions of ThT with N,S-CQDs and with HER2 G4 in the presence of N,S-CQDs.

The digital photographs of the probe captured under day light and UV illumination in the presence and absence of HER2 G4 are given in Figure 14 (b) and Figure 14

(c). Cuvettes 1 and 4 contains only the N,S-CQDs solution. N,S-CQDs solution which is almost clear under the daylight (Cuvette 1), has blue emission under the UV-light. Quenching of the fluorescence of N, S-CQDs was observed upon addition of ThT onto the N, S-CQDs sample (Cuvettes 2 and 5) under the optimal conditions. No aggregation was observed under the daylight upon addition of ThT onto the N, S-CQDs solution (probe system). Only, the color of the solution changed to pale yellow. On the other hand, under the UV illumination a distinct fluorescence quenching of the N,S-CQDs was observed mainly due to the interactions of N,S-CQDs with ThT dye. After the addition of the target analyte HER2 G4 solution to the probe system, a clear fluorescence recovery and emission shift from blue to green was observed under the UV-light (Cuvette 6) with a color change to brighter yellow under day light (Cuvette 3). The change in the emission wavelength and the color represents the binding of ThT to HER2 G4.

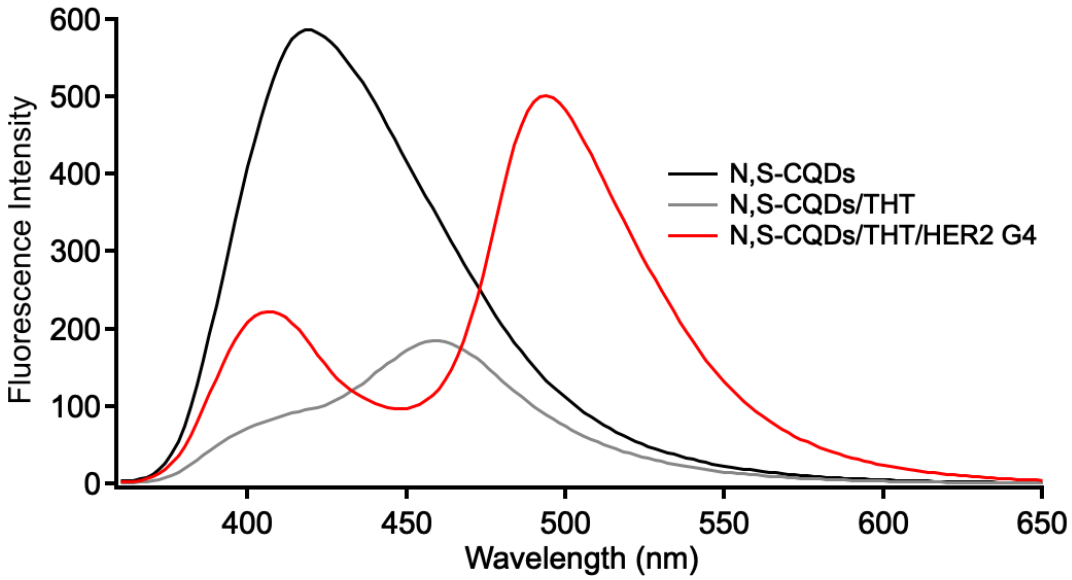

(a)

(1) (2) (3) (4) (5) (6)

(b) (c)

Figure 14. (a) Step-by step fluorescence response of the developed probe towards the target analyte (HER2 G4): black and gray traces represent 2.5 ppm N,S-CQDs and the same sample upon addition of ThT, respectively under the optimized conditions (40.98 μM), recorded after 5-minutes of mixing. The red trace represents the developed probe 1-minute after the addition of the target analyte, HER2 G4, at the optimized conditions. The corresponding step-by-step digital photographs of the probe captured under day light (b) and UV illumination at 365 nm (c) upon addition of the sensing ingredients under the optimized conditions at room temperature. Cuvettes from 1 to 6 contains N,S-CQDs, N,S-CQDs/ThT, N,S-CQDs/ThT/HER2 G4, N,S-CQDs, N,S-CQDs/ThT, N,S-CQDs/ThT/HER2 G4, respectively.

3.4 Optimization of N,S-CQDs Concentration

The concentration of the main probe, N,S-CQD concentration, was needed to be optimized as the initial step in creating a sensitive detection platform. First, 2.5 ppm, 5.0 ppm, and 10.0 ppm concentrations of N,S-CQDs were prepared, and each concentration was titrated with 1000.0 μM ThT stock solution (Figure 15). In the graphs, for consistent detection, the fluorescence intensity of the systems was adjusted with different voltages as follows 625 (2.5 ppm), 560 (5.0 ppm), and 530 (10.0 ppm). The black line represents 2500.0 μL of prepared N,S-CQDs, the grey

lines represent the samples after the gradual addition of 1000.0 µM ThT where the volume was increased by ten unit, and the red line represents the final titration point. Following N,S-CQDs titrations, there was a noticeable decrease and shift in the fluorescence intensity of the peak. Figure 15 (c) shows that 10.0 ppm N,S-CQD solution was quenched faster. However, as the concentration of N,S-CQDs decreased, the quenching of the solution started to decrease as shown in Figures 15 (a) and (b). Since the response of the solutions containing 2.5 ppm or 5.0 ppm N,S-CQDs were similar, 2.5 ppm was chosen as the concentration of N,S-CQDs to use in further experiments to make the probe system more economical for the method development by using less material.

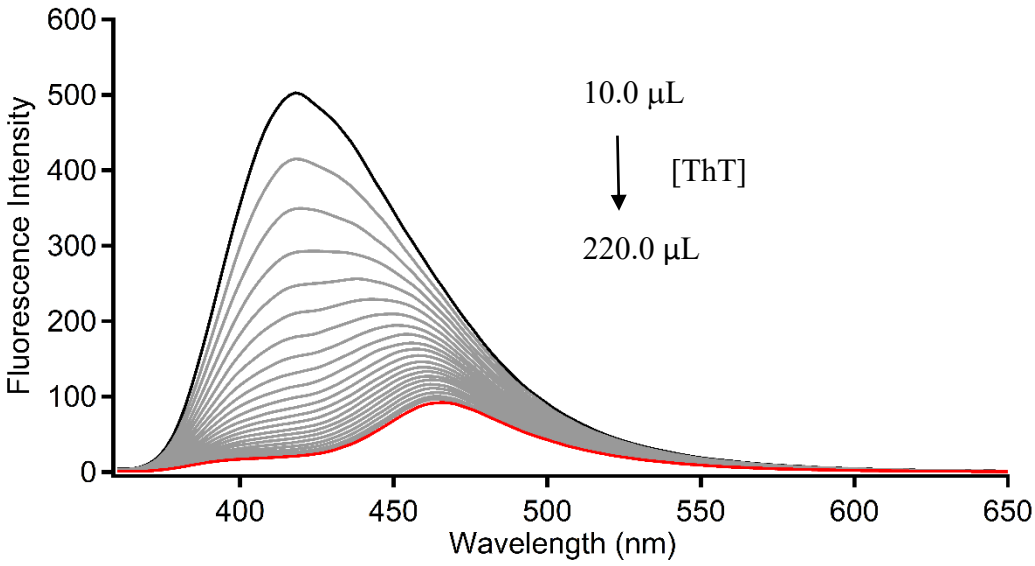

(a)

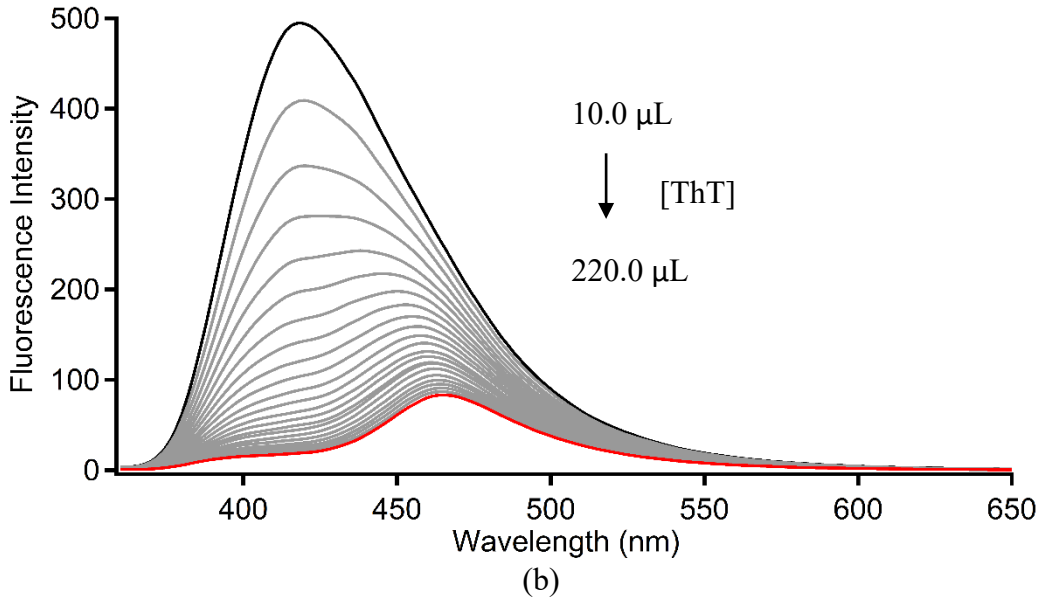

(b)

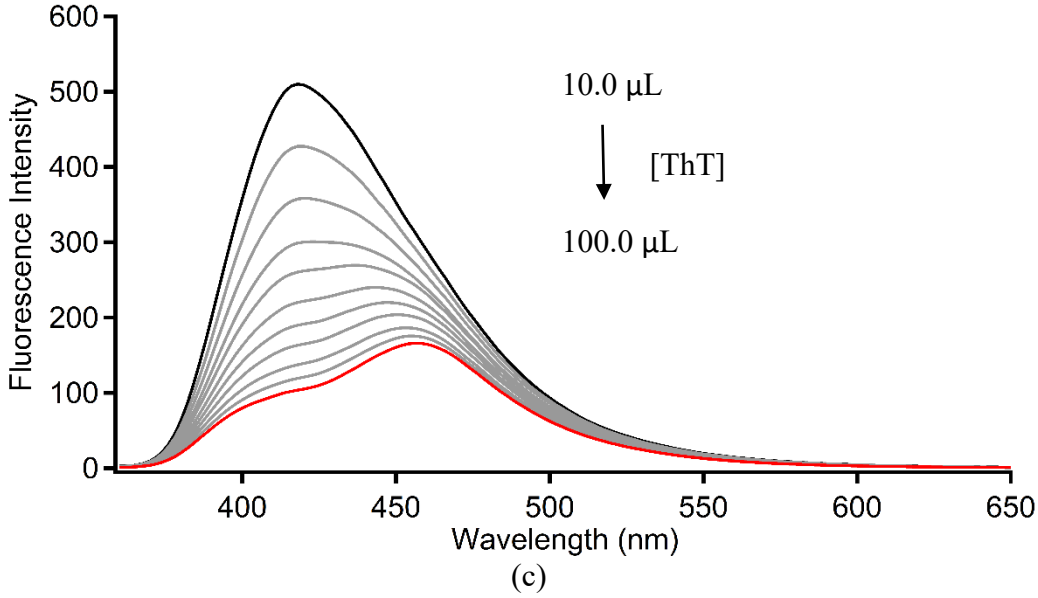

(c)

Figure 15. Fluorescence spectra of 2500 µL of (a) 2.5 ppm N, S-CQDs (b) 5.0 ppm N, S-CQDs (c) 10.0 ppm N, S-CQDs upon titration with increasing volumes of ThT under ambient temperature after 5-minutes of mixing.

3.4.1 Optimization of ThT Concentration

Thioflavin T [2-(4-(dimethylamino)phenyl)-3,6-dimethylbenzo[d]thiazol-3-ium; ThT] is another name for the commonly used dye Basic Yellow 1, a benzothiazole salt. For more than 50 years, it has been utilized as a fluorescent marker in biomedical research [198]. In aqueous solution, ThT exhibits a weak fluorescence with an emission band at 494 nm and excitation wavelength of 425 nm (Appendix D, Figure 29) [199]. The fluorescence emission signal of ThT shows slight increase when binds to DNA duplex structures [200]. However, in 2012, Mohanty and co-workers reported that water soluble ThT can bind to G4 structures with very high selectivity using 22AG human telomeric DNA resulting in a fluorescence light-up in the visible area. When compared to the other DNA forms (250-fold increase in emission in their presence), the fluorescence intensity of ThT is found to be increased about 2100 or 1700-fold upon binding to 22AG in the presence and absence of K^+ ions [201]. In another study, Faverie et al. reported that compared to control duplexes and single strands, which had a much less impact on emission, not only the telomeric G4 structure but most of the other G4 structures studied (Bom17, Oxy 3.5, Asc20, Plas24, 22Ag, 45Ag, 22AgR, c-myc, AKTI, VEGF, VAV1, and KRAS) were also able to increase the fluorescence emission of ThT significantly. Their study lead the way to the use of ThT to detect the presence of G4 structures [202].

Here, our developed probe depends on the fluorescence quenching of N,S-CQDs in the presence of ThT, and the regain of the fluorescence upon addition of HER2 G4 in addition to the increase in the emission of ThT upon HER2 G4 binding. Consequently, ThT concentration was optimized next to achieve a higher sensitivity.

In order to optimize ThT concentration in the developed probe, 2.5 ppm N,S-CQD solution was titrated by 500 μM, 1000 μM, and 4000 μM ThT with 10.0 μL increments (Figure 16). In the graphs, the black line represents 2.5 ppm 2.5 mL prepared N,S-CQDs, the grey lines represent the ThT addition with 10.0 μL increments, and the red line represents the final point of the titration with ThT. As

displayed in Figure 16, titration with 500 μM ThT exhibited a more gradual decrease in the fluorescence intensity mainly due to the addition of lower amounts of ThT, and therefore this concentration was chosen as the ThT concentration to use in all future experiments.

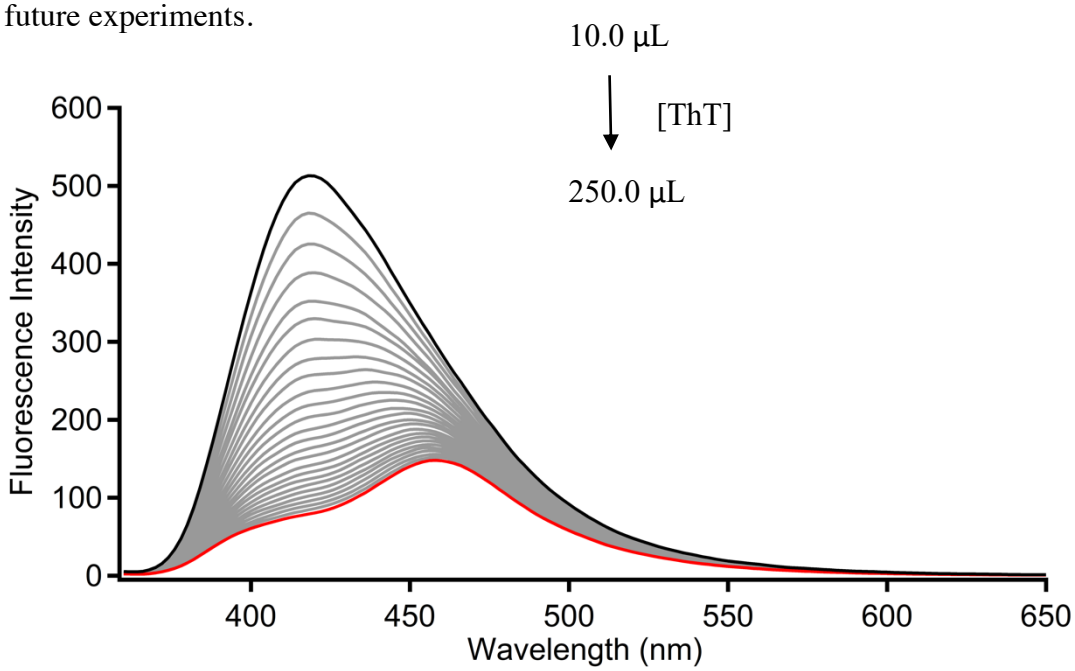

(a)

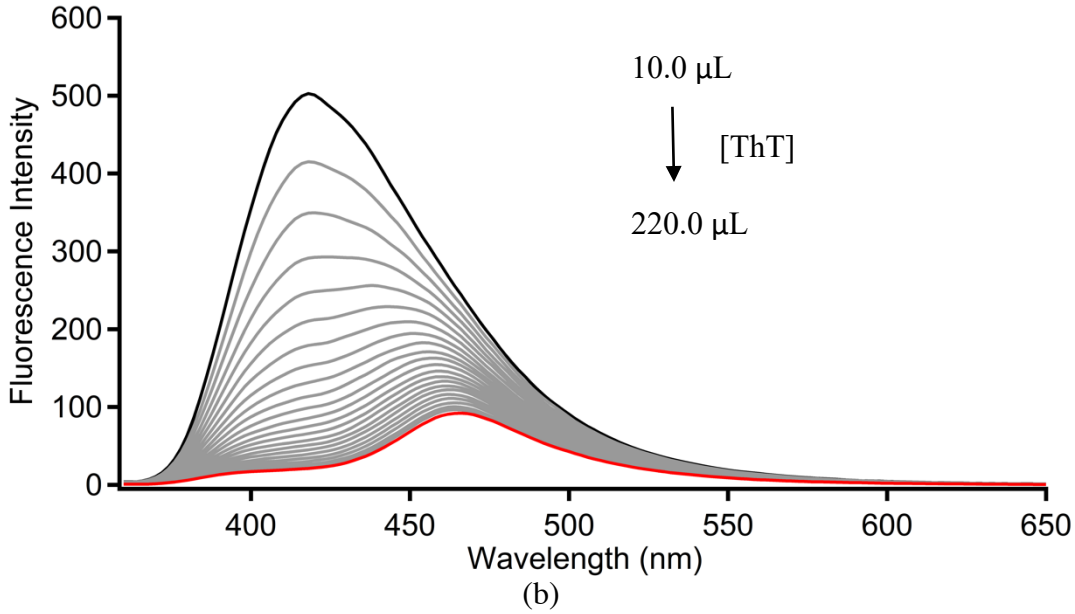

(b)

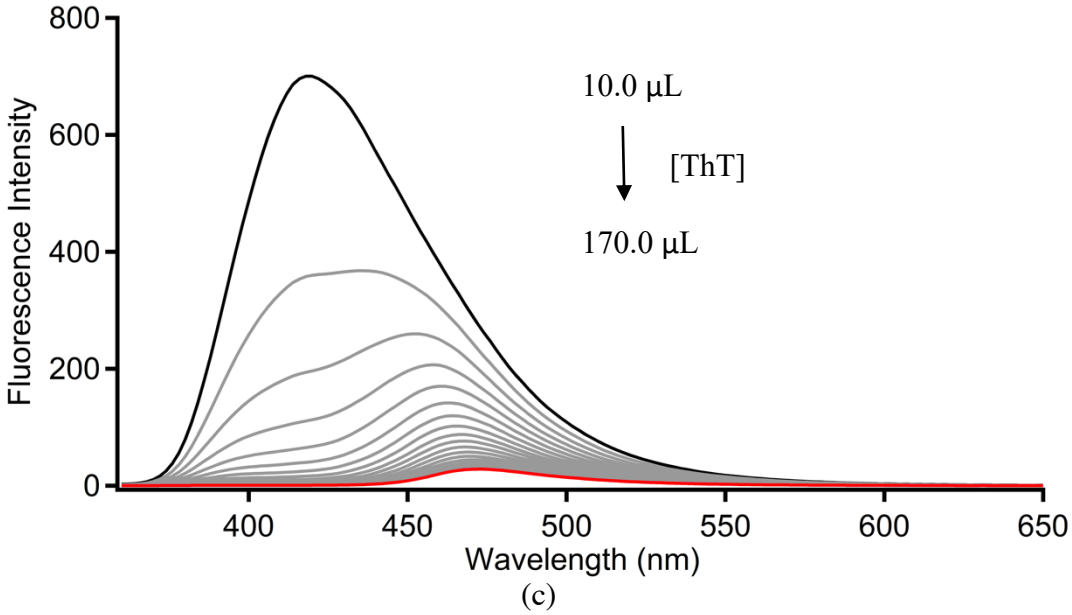

Figure 16. Fluorescence spectra of 2.5 ppm 2500 µL of N,S-CQDs titrated with varying concentrations of ThT (a) 500 µM (b) 1000 µM and (c) 4000 µM under ambient temperature, after 5-minutes of mixing.

2.4.2. Quenching Constant

To calculate the quenching constant, N,S-CQDs solution (2.5 ppm) was titrated with 500 µM ThT. The experiment was conducted in triplicate (Appendix C, Figures 28-31). Figure 16 represents the corresponding modified Stern-Volmer plot and the quenching constant calculated as 4.6×10^4 L/mol form $y = (1.7157 \times 10^{-5}) x + 0.9206$ by the related Stern-Volmer equation [203];

$$F_0/(F_0-F) = [1/(f_a K_q)] \times [1/[Q]] + 1/f_a$$

Where, F_0 is the fluorescence intensity of N,S-CQD solution in the absence of the quencher, and F is the fluorescence intensity N,S-CQD solution in the presence of quencher at maximum emission wavelengths. f_a is the accessible fluorescence's fraction, K_q is the quenching constant, and [Q] is the concentration of quencher.

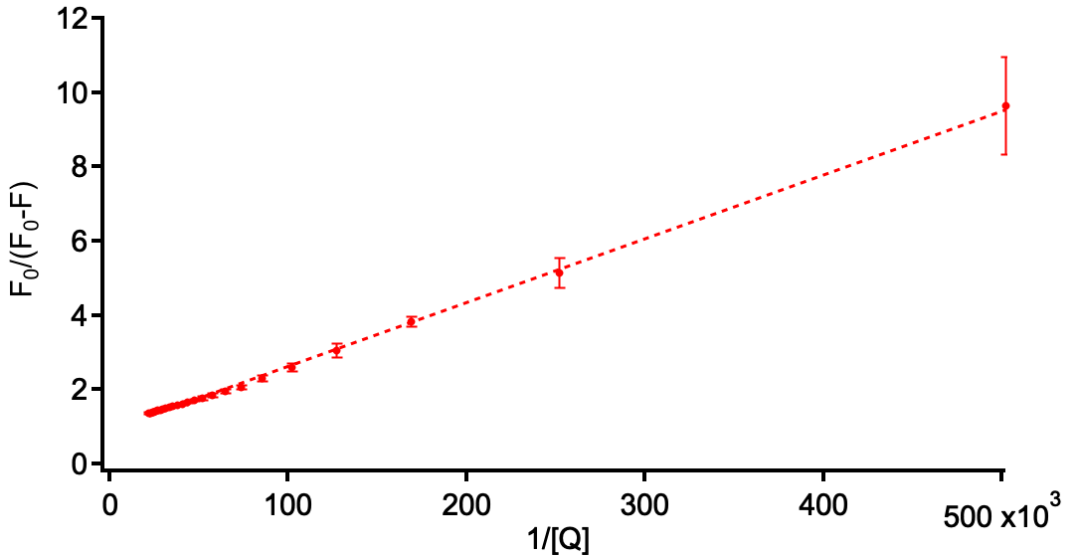

Figure 17. Modified Stern-Volmer plot of $F_0/(F_0-F)$ vs. 1/[Q]. The error bars indicate SD (n=3).

3.4.2 pH Optimization of the Probe

One of the critical parameters that affect the response of the system in sensing procedures is the pH. Since, CQDs have different degrees of oxidational functional groups (such as C=C and -COOH) on their surface, pH can alter the CQDs' energy band gap and result as different emission wavelengths and fluorescence intensities [204]. The pH of the synthesized N,S-CQDs was optimized to 3.0, 5.0, 7.0, and 9.0, where the initial pH was 6.0. N,S-CQDs/ThT mixtures were also prepared at the same pH values as control experiments. As displayed in Figure 18, the highest fluorescence intensity belongs to the initial pH of the probe which is represented as black line. When pH was adjusted to 3 (pink line), the peak was shifted to longer wavelength where the maximum emission wavelength changed from 420 nm to 438 nm. The intensity of the peak was also decreased compared to the intensity of the peak at the original pH of 6.0. When the pH was adjusted to the 5.0, 7.0, and 9.0 (represented by green, blue and purple lines, respectively) the fluorescence intensity of the N,S-CQDs did not change remarkably. Furthermore, with the addition of ThT,

the fluorescence intensity of the quenched N,S-CQDs was almost the same at pH 6.0, 7.0, and 9.0 which are represented by red, blue and purple dashed-lines in Figure 18, respectively. However, when the pH was adjusted to 5 (shown as green dashed-line), quenching was lower and when the pH was 3 (shown as pink dashed-line) quenching was higher, but the shoulder at 406 nm was disappeared, and the peak was shifted. In conclusion, the pH of the original probe (pH = 6) was selected for the future experiments.

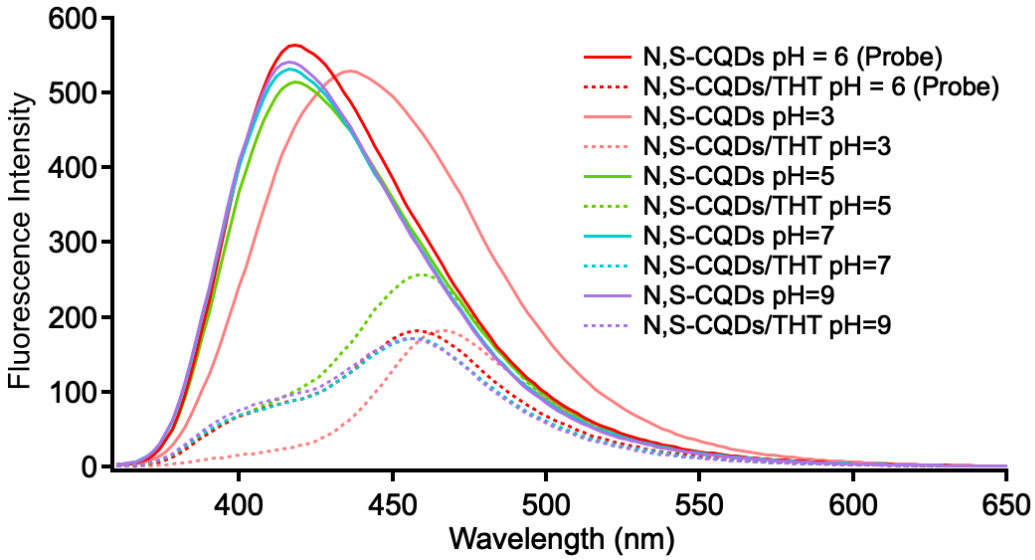

Figure 18. Fluorescence emission spectra of 2.5 ppm N, S-CQD solution at different pH values in the absence and presence of 500 μM 250.0 μL ThT. Under ambient temperature after 5-minute mixing.

3.4.3 Response Time of the Proposed Probe to HER2 G-Quadruplex

Another important parameter for evaluating the fluorescence detection performance of the proposed probe is the response time [205]. Figure 19 represents the response time of the proposed probe upon addition of target analyte in 1-hour time interval. 2.5 ppm N,S-CQDs sample is represented by the black trace, and N,S-CQDs/ThT mixture (probe system) is represented by the grey trace. The orange traces represent the fluorescence response of the probe system with HER2 G4 (target analyte) after

1, 3, 5, 10, 15, 20, 30, and 45 minutes, and the red trace shows the fluorescence response after 60 minutes. The inset shows the corresponding plot of $F_1/(F_0-F_2)$ vs. time (min), where F_0 is the corresponding fluorescence response of N,S-CQDs at 406 nm in the absence of ThT and target analyte addition, F_1 and F_2 are representing the fluorescence response of the N,S-CQDs/ThT probe with the target analyte HER2 G4 at 494 nm and 406 nm, respectively. Here, F_1 represents the interactions between HER2 G4 and ThT (at 494 nm), and F_2 represents the weakened interactions of ThT and N,S-CQDs upon addition of the target analyte, HER2 G4. As displayed in Figure 19, the maximum response was achieved within 1 minute and no significant change was observed afterwards. Accordingly, the obtained results prove that the probe's response time is fast and stable for 60 min. Therefore, 1 min was chosen as the optimized reaction time for all the future experiments.

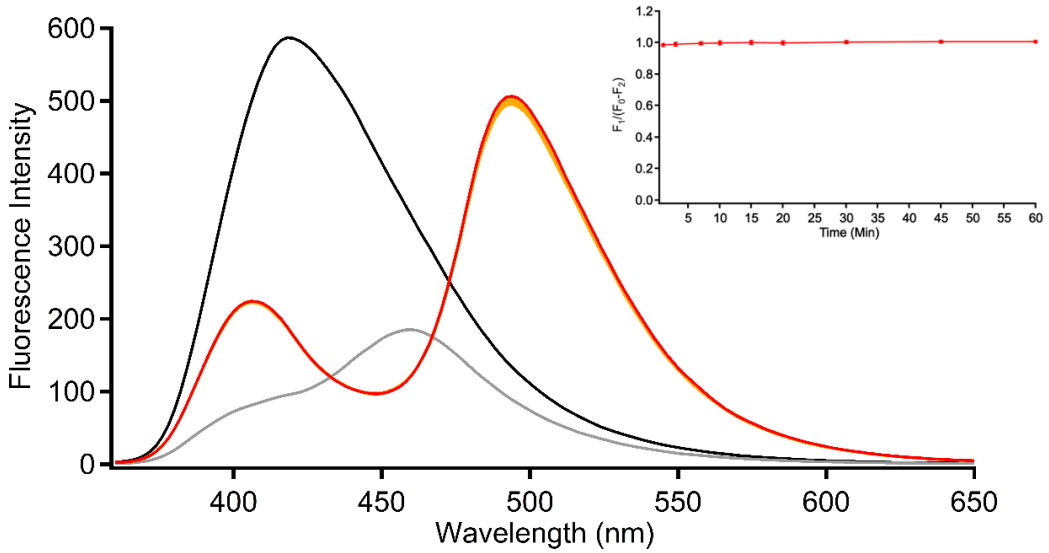

Figure 19. Fluorescence spectra of N,S-CQDs (2.5 ppm, black spectrum), 2.5 ppm N,S-CQDs/ThT (final concentration 40.98 µM, gray spectrum) and N,S-CQDs/ThT probe after the addition of HER2 G4 stock solution (75 µM) at 1, 3, 5, 10, 15, 20, 30, 45 (orange spectra), and 60 minutes (red spectrum). The inset represents the corresponding plot of $F_1/(F_0-F_2)$ vs. time (min). Under ambient temperature without mixing. The error bars indicate SD (n=3).

3.4.4 The Effect of Temperature

Temperature is one of the main thermodynamic variables that significantly influence the biological and chemical systems [206]. Consequently, the temperature at which the experiment is performed is another crucial parameter for evaluating the detection performance of the sensing platforms. A number of studies reported the effect of temperature on the fluorescence of CQDs [206]. For instance, Yu et al. reported that the fluorescent carbon dots synthesized from glacial acetic acid, H_2O and P_2O_5 displayed a decrease in fluorescence with increasing temperature. Their detailed investigation concluded that this was mainly due to electron – electron interactions [207]. Kalytchuk et al. synthesized N,S-CQDs that are similar to ours using acid and L-cysteine via hydrothermal synthesis method. They reported that the N,S-CQDs were also displaying decreasing fluorescence intensity in the 1-80 °C temperature range without causing any detectable shift of the PL emissions [208]. In an another study, Li et al. synthesized N,S-CQDs using methionine and ethylenediamine as the precursors by hydrothermal method. They also observed a decrease in fluorescence of N,S-CQDs with increasing temperature from 20°C to 80°C [209].

Then again, the effect of temperature on G4 structures and their interactions with small molecules are also well reported in the literature. Typically, G4 structures have relatively high thermal denaturation temperatures, that depends on the sequence, structure and the solution conditions [210]–[212]. Assessment of G-quadruplex stabilities has been predominantly based in the literature on a simple determination of G-quadruplex melting temperatures Tm, i.e., the temperature at which 50% of the quadruplex is unfolded [213]. As an example, Mohanty et al. reported that the ThT binding could induce the formation of human telomeric G4 with different thermal denaturation temperatures depending on the buffer conditions [201].

Based on the aforementioned studies, we evaluated the temperature response of our developed probe. Figure 20 (a) and (b) display the fluorescence response of the probe upon addition of HER2 G4 after 1 minute of interaction (optimal time) with

increasing temperature from 5°C to 70°C with 5°C increments. Figure 20 (a) depicts the change in emission intensity at 406 nm that can be taken as a representation of decreasing N,S-CQDs/ThT interactions upon addition of the target analyte, and Figure 20 (b) displays the change in intensity at 494 nm which can be taken as the representative of the interactions between HER2 G4 and ThT. As it can be seen from the Figure 20, at both wavelengths, fluorescence intensity decreased dramatically with a gradual increase in temperature. A control experiment with only 2.5 ppm N, S-CQDs (Appendix C, Figures 34-35), exhibited almost the same trend in the fluorescence as temperature increased, demonstrating that the probe system and N,S-CQDs solution are not stable at high temperatures As a result, it was found that the decrease in the fluorescence intensity of the detection platform was due to the instability of N,S-CQDs at high temperatures as expected, in line with the previously reported studies [185], [214]–[216]. These findings were reported to be due to the CQDs' surface imperfection. It has been reported that the majority of excited electrons return to the ground state non-radiatively at higher temperatures (due to the increase of non-radiative surface pathways (traps/defects), resulting in a decrease in fluorescence intensity with increasing temperature [217]. Accordingly, the ambient temperature was selected for use in further experiments due to the relatively high stability of N,S-CQDs at ambient temperature, and its convenience.

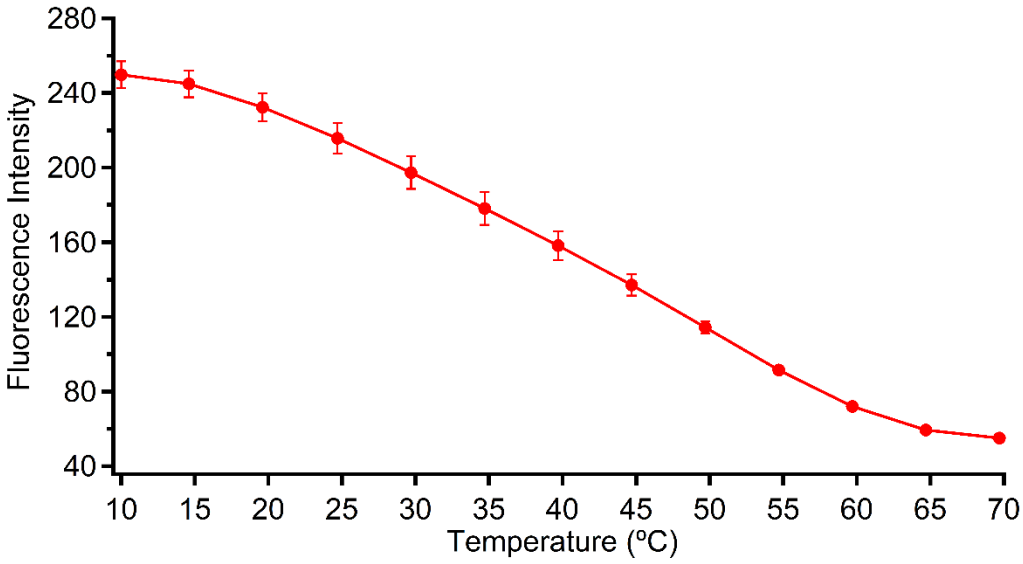

(a)

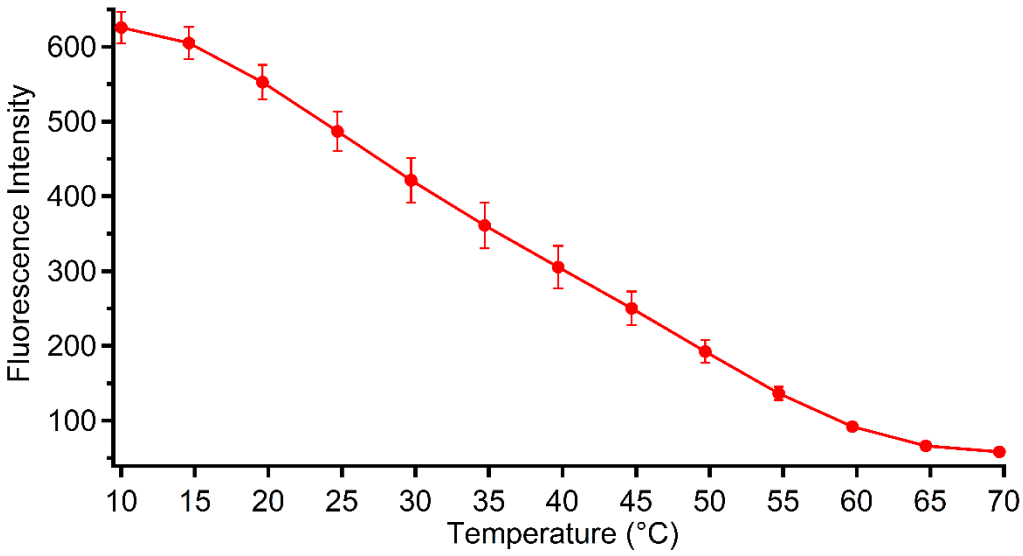

(b)

Figure 20. The effect of temperature on the response of the probe upon addition of HER2 G4 under the optimized conditions at (a) 406 nm and (b) 494 nm. The error bars indicate the SD (n=3).

3.4.5 The Selectivity of the Proposed Probe

The fluorescence recovery response of the system towards different nucleic acid structures, such as single-stranded nucleic acids (Poly A, dA_{32}, dT_{32}), double-stranded nucleic acid ($dA_{32}dT_{32}$), and other available G4 structures in our laboratory (RB, Pu22, C-MYC, VEGF, BCL2, K-RAS) was examined under the same conditions to determine the selectivity of the developed sensing platform. The final concentrations of all examined nucleic acids were set as 32.8 nM. In these control experiments, the nucleic acid stock solutions were also prepared at K-phosphate buffer solution (25 mM, containing 70 mM KCl) and the probe solution was prepared in H_2O. Figure 21 (a) depicts the fluorescence response of the probe after the addition of various nucleic acid structure into the probe one at a time under the optimized conditions. The bar graph in Figure 21 (b) also displays the fluorescence recovery responses as the $F_1/(F_0-F_2)$ with respect to nucleic acid sequence. As it can be seen from both Figures 21 (a) and (b), neither single-stranded structures nor double-stranded structures were able to recover the fluorescence intensity of the proposed probe significantly.

For the purpose of decreasing the limit of detection, HER2 G4 with a final concentration of 7.37 μM was also compared to nucleic acid structures with a final concentration of 9.84 μM. When compared to other tested nucleic acid structures with a final concentration of 9.84 μM, it was observed that even HER2 G4 with final concentration of 7.37 μM exhibited a substantially stronger fluorescence recovery response. The $F_1/(F_0-F_2)$ value of single- and double-stranded DNAs are around 0.2, and other G4 structures value ranges from 0.4 to 0.6. While that of HER2 G4 (at the same and lower concentrations) is around 1.5.

It has been known that ThT does have only limited emission in the presence of double stranded or single stranded nucleic acid structures, where as it displays high but varying emission profiles in the presence of G4 structures [202], [218], [219]. De la Faverie et al. assayed 31 different nucleic acid structures and reported that

statistically the fluorescence enhancement was >60 times in the presence of G4 and <20 times on average in the presence of other structures. They also report that the emission profile of ThT in the presence of G4s is shown to depend on the G4 sequence and structure [202]. Consequently, here the selectivity of our probe, not observing the emergence of fluorescence emission at 494 nm in the presence of neither single stranded nor double stranded nucleic acid structures is not surprising.

Among the examined G4 structures in this study, RB shows antiparallel [220] G-quadruplex folding however, Pu22, C-MYC, VEGF, BCL-2, KRAS, and HER2 G-quadruplex structures shows parallel folding [220]–[225]. ThT binds to G4 structures from conformational cavity [219]. From the aforementioned information, it can be concluded that the developed probe can selectively discriminate HER2 G4 structure from other tested nucleic acid structures. And, the developed system shows high selectivity towards HER parallel G4 structure among other parallel G4 structures, demonstrating the applicability and affordability of proposed method for selective detection of HER2 G4. Moreover, to examine the structural interactions of N,S-CQDs and N,S-CQDs/ThT with HER2 G4 CD experiments were performed.

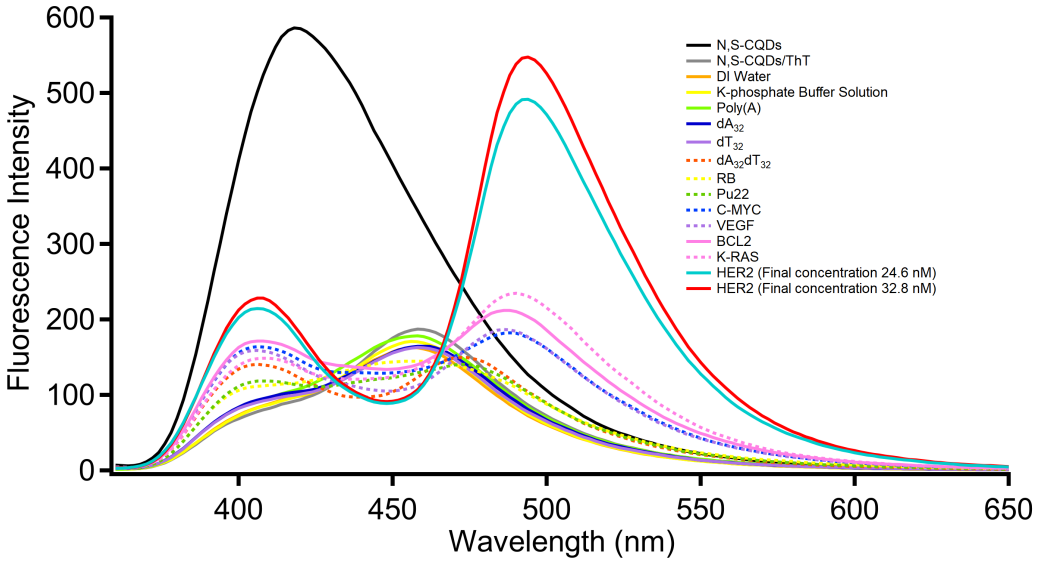

(a)

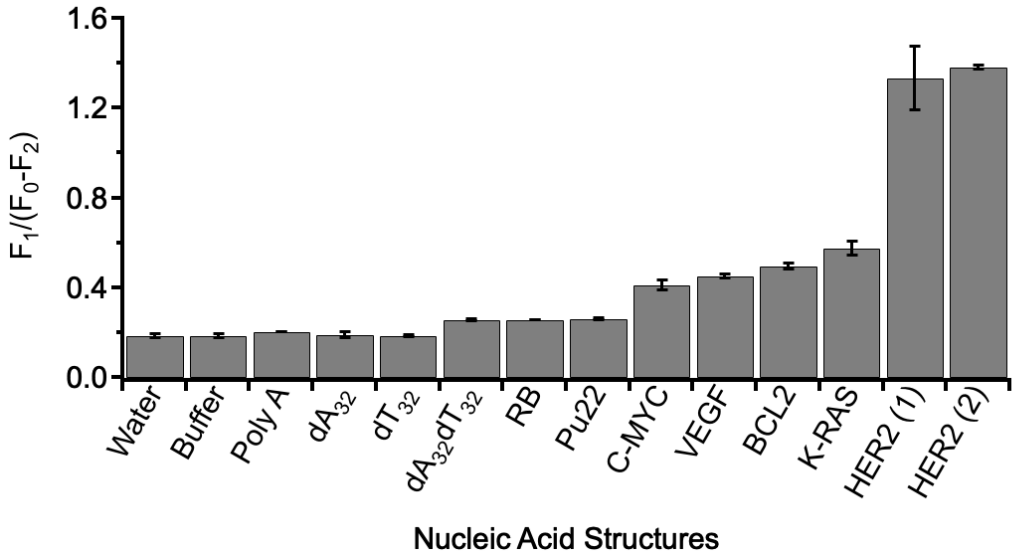

(b)

Figure 21. Selectivity studies for the N,S-CQDs/ThT probe based on addition of 300 μL of 100 μM of each nucleic acid structure except HER2 (1) which is based on the addition of 300 μL of 75 μM of G4 structure under ambient temperature (a) fluorescence response (b) bar graph of $F_1/(F_0-F_2)$ vs. Nucleic Acid Structures. The error bars indicate SD (n=3).

3.4.6 The Sensitivity of the Proposed Probe

Fluorometric titration tests were conducted under optimal conditions to examine the analytical characterization of the proposed probe (sensitivity and linear range) of the assay. Figure 22 (a) depicts the fluorescence profile of the N,S-CQDs (2.5 ppm, 2500 μL) and ThT (500 μM, 250 μL) probe upon gradual addition of HER2 G4 (75 μM, 300 μL) in the range of 0.27 - 6.0 μM. As it can be seen in the Figure 22 (a), a gradual recovery of the fluorescence was observed with the appearance of two new peaks at 406 nm and 494 nm. The obtained calibration curve (Figure 22 (b)) shows a linear fit equation as $F_1/(F_0-F_2) = 0.1753C + 0.1754$ with $R^2 = 0.99$ (where C is the concentration of HER2 G4) in the dynamic range between 0.27 - 6.0 μM – [HER2]. Additionally, the detection platform's limit of detection (LOD) was determined to be

0.22 µM proving the suitability of the proposed fluorometric method for the sensitive detection of HER2 G4 structure (calculated using the formula below):

LOD = 3.3 x (S_b/a)

Where, 'S_b' denotes the intercept's standard error and 'a' denotes the calibration curve's slope [149].

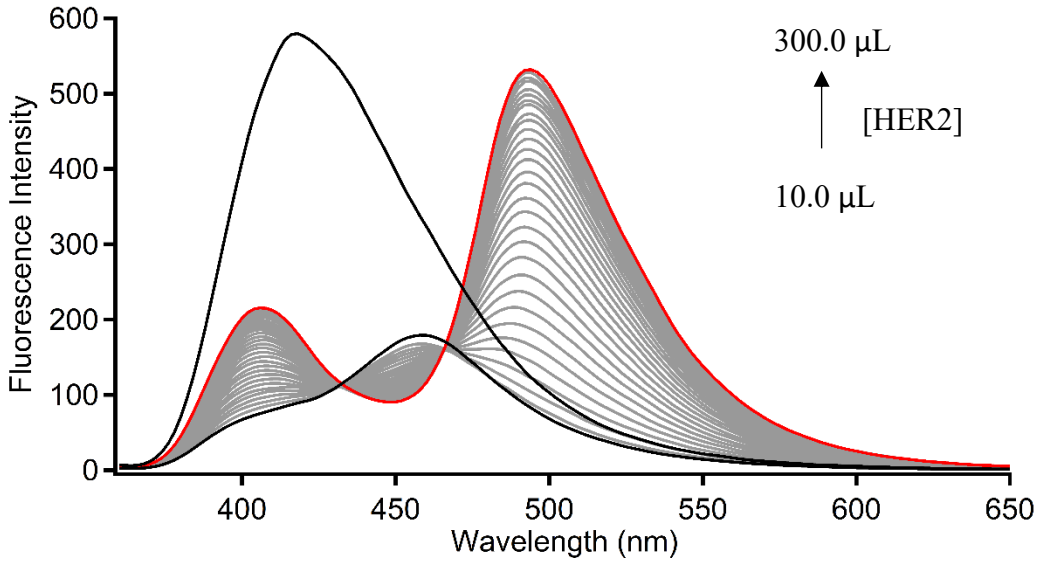

(a)

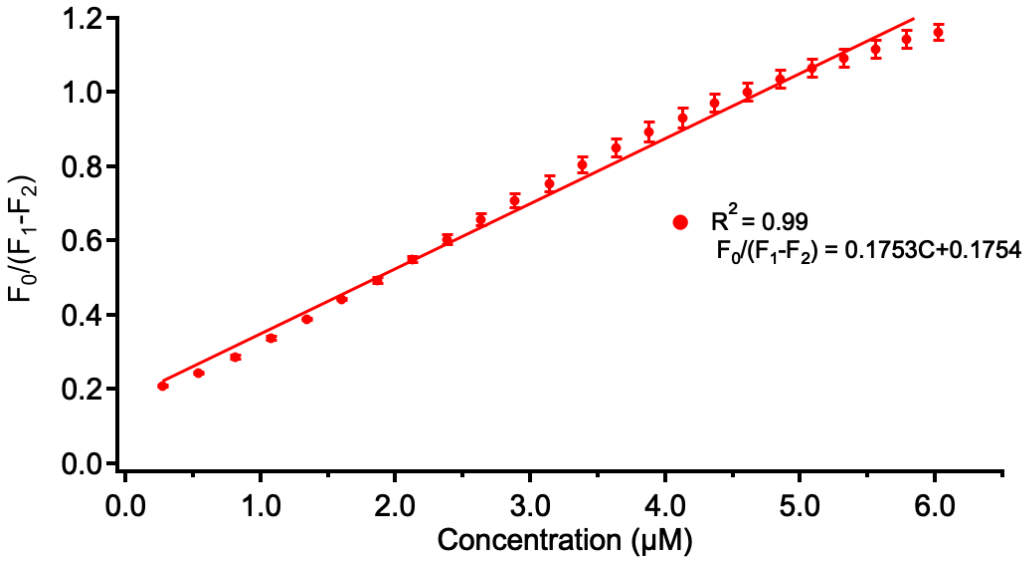

(b)

Figure 22. (a) Fluorescence spectra of 2.5 ppm N, S-CQDs/ThT (final concentration 40.98 μM) probe upon the addition of different volumes (10.0 – 300.0 μL) of HER2 G4 stock solution (75 μM). (b) Plot of $F_1/(F_0-F_2)$ vs. HER2 G4 concentration under ambient temperature. The error bars indicate SD (n=3).

3.4.7 Characterization of the Proposed Platform via Circular Dichroism (CD) Spectroscopy

Finally, to further characterize the proposed system, circular dichroism (CD) spectra of the components of the proposed platform were collected [226]. CD spectroscopy is commonly used to depict the G4 secondary structures. It has been known that parallel and anti-parallel G4 structures both shows positive CD absorption at 210 nm. However, parallel G4 structures shows minimum absorption at around 245 nm and positive CD absorption at 260 nm, whereas anti-parallel G4 structures shows negative CD absorption at 260 nm along with positive absorption peak at 290 nm [109], [226], [227]. As displayed in Figure 23, HER2 G4 structure displayed a parallel folding (green line) with an ellipticity minimum at 240 nm (-12.5 mdeg) and a maximum at 261 nm (27.19 mdeg) , which being in good agreement with recent reports published in the literature [109], [226], [227]. N,S-CQDs/ThT mixture did not rise to a CD spectrum due to the lack of optical activity (black line). Furthermore, it was established that neither the addition ThT nor the mixture of N,S-CQDs/ThT could alter the structure of HER2 G4 (blue and red lines), since no change was observed in the CD spectra of HER2 G4, HER2 G4/ThT, and HER2 G4/ThT/N,S-CQDs.

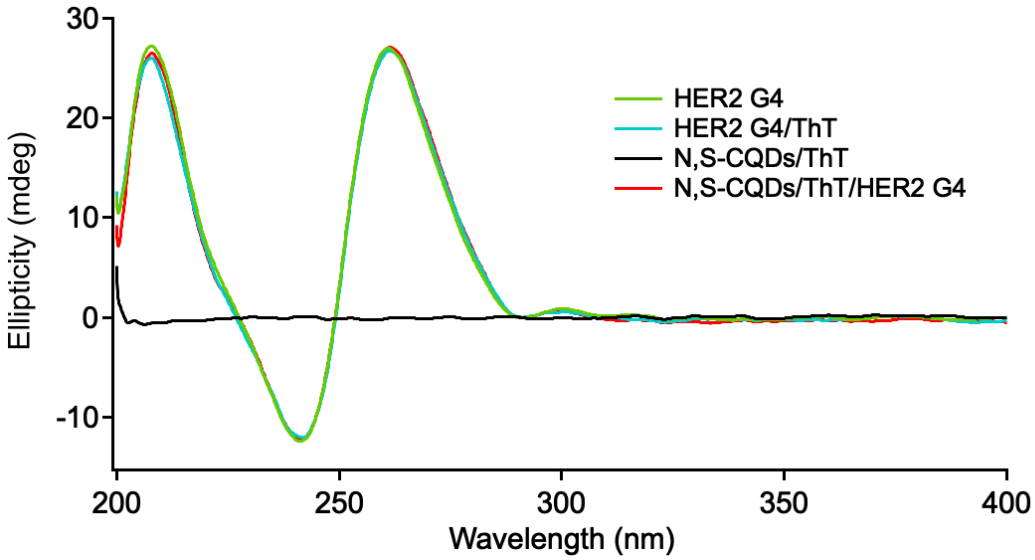

Figure 23. CD spectra of HER2 G4 (3.0 µM), HER2 G4/ThT (3.0 µM/3.0 µM), N,S-CQDs/ThT/HER2 G4 (2.5 ppm/3.0 µM/3.0 µM) and N,S-CQDs/ThT (2.5 ppm/3.0 µM) samples recorded at optimized conditions.

3.4.8 Characterization of Proposed System

The HR-TEM images of samples including N,S-CQDs/ThT (a and b, scale bars: 10 nm and 20 nm, respectively) and N,S-CQDs/ThT/HER2 G4 (c and d, scale bars: 50 nm and 5 nm, respectively) is shown in Figure 24. According to the captured micrographs. It can be clearly observed that the addition of neither ThT nor target analyte (HER2 G4) in the probe system (N,S-CQDs/ThT) change the topology, morphology and size significantly.

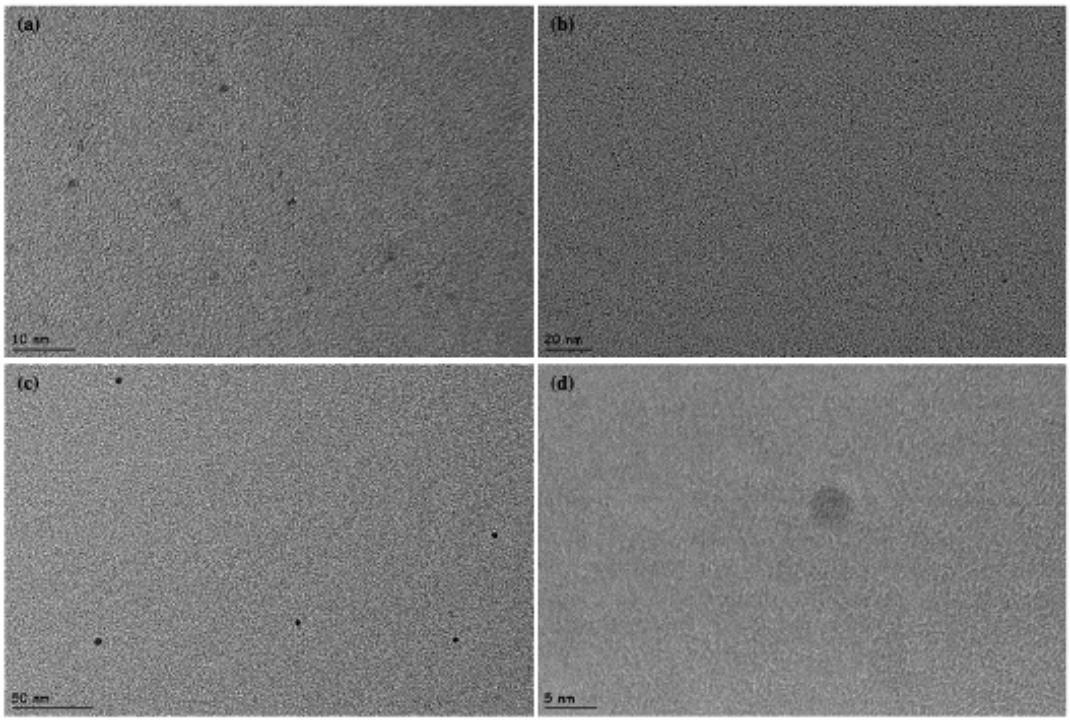

Figure 24. HR-TEM micrographs of the synthesized N,S-CQDs upon addition of ThT under the optimized conditions (a and b) and the probe system (N,S-CQDs/ThT) after the addition of the target analyte, HER2 G4, (c and d), at different magnifications.

3.4.9 Possible Sensing Mechanism

One possible explanation for the mechanism of action of the proposed system is displayed in Scheme 2. As can be seen, the synthesized N,S-CQDs exhibit bright and distinct blue emission fluorescence upon excitation at 350 nm. However, after the addition of ThT fluorescent dye under the optimal conditions, the FL emission of the N,S-CQDs was quenched remarkably probably due to the fact that the functional groups on the surface of N,S-CQDs interacts with ThT followed by their surface covering. After the addition of the target HER2 G4 structure, a relative and weak FL recovery at 406 nm and a color shift from pale blue to bright green was observed. The fact behind this behavior could be possibly due to the strong interaction and

affinity between HER2 G4 and ThT on the surface of the N,S-CQDs (which was quenched in the presence of ThT) resulting in the relative recovery of fluorescence emission of N,S-CQDs accompanied by the appearance of a new peak at around 494 nm due to the binding of HER2 G4 structure to ThT. As discussed earlier, ThT binds to G4 structures strongly and the interaction between N,S-CQDs and ThT is thought to change/weaken as a result of this interaction.

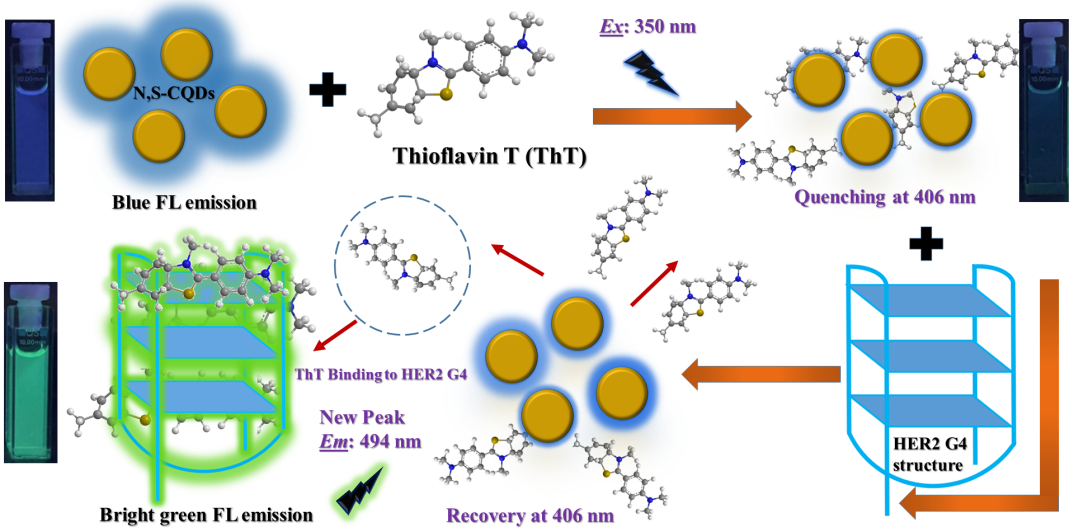

Scheme 2. Schematic representation of possible mechanism of the developed probe for the detection of HER2 G4 structure.

CHAPTER 4

CONCLUSION

Within the scope of this thesis, a facile, low-cost, sensitive, non-toxic, fast, effective, and novel ratiometric fluorescence detection platform was developed to detect HER2 G4 structure. As it is mentioned in the introduction part of this thesis, HER2 G4 structure is found to have an important role in the regulation of HER2 expression where the absence of HER2 G4 resulted in the up-regulation of HER2 protein [109]. The upregulation of HER2 is directly linked especially to the development and progression of breast cancer [109]. Moreover, the regulation of normal breast growth can be linked to HER2 receptor [100]. Recently, it was demonstrated by Cui et. al. that compared to the wild type (G4 forming in plasmid) the relative luciferase activity of the mutant plasmid (lacking G4 formation) was increased approximately 40%, demonstrating that the deletion of the G4 can increase the activity eof HER2 promoter and expression of HER2. In the wild type, down regulation of the HER 2 activity was observed [109]. Overall, since increased HER2 expression is associated with the progression and development of aggressive breast cancer, the detection of HER2 G4 is thought to possibly play a vital role in early detection or treatment of the breast cancer. To the best of our knowledge, there is no reported detection platform for the HER2 G4 structure of HER2 promoter region, so far.

Furthermore, as mentioned earlier, current detection platforms including immunohistochemical, in situ hybridization and fluorescence in situ hybridization are relatively expensive and time-consuming in spite the fact that they present powerful performance in detection of cancer biomarkers [179].

Based on the aforementioned studies, within the scope of this thesis we aimed to develop a ratiometric detection platform based on fluorescence spectroscopy with decent selectivity and high sensitivity for HER2 G4 structure using cost effective

and environmentally friendly N,S-CQDs/THT system. N,S-CQDs was synthesized via solid-phase thermal synthesis method. Particle size analysis and HR-TEM images showed that the synthesized N,S-CQDs have sizes lower than 10 nm. The obtained XRD pattern showed that the synthesized N,S-CQDs have an amorphous structure and XPS analysis results confirmed that the co-doping with nitrogen and sulfur, have been accomplished successfully. Fluorescence quantum yield of the synthesized N,S-CQDs was found as 34%. The optimum concentration of N,S-CQDs and ThT was chosen with the titration experiments as 2.5 ppm and 40.98 μM, respectively. Following to concentration optimizations, pH, time, and temperature effects were examined and optimized. The pH of the probe was as 6.0 (original pH value) since the probe gave the highest fluorescence response at original pH value. The reaction time was selected as 1 minute and ambient temperature was selected for all detection steps. Spectroscopic methods (CD and Fluorescence spectroscopy) showed that the developed probe can be used as a selective and reliable detection platform for HER2 G4. The CD measurements showed that the secondary structure of HER2 was not affected by the probe. The selectivity investigations showed that under the optimized conditions the developed probe is highly selective towards HER2 G4 structure compared to the other examined G4 structures (RB, Pu22, C-MYC, VEGF, BCL2, K-RAS) and available single (Poly A, dA_{32}, dT_{32}), and double ($dA_{32}dT_{32}$), stranded DNAs. The N,S-CQDs/THT probe showed high selectivity towards HER2 G4 within the linear dynamic range of 0.27μM – 6.0 μM and a LOD of 0.22 μM. We believe that the developed detection platform can bring a new perspective to the early detection of HER2 G4. As the future perspective of this study, cell-line experiments and in-vitro studies will be performed to confirm the applicability of the developed probe in complicated matrices.

REFERENCES

[1] S. E. McNeil, “Nanotechnology for the biologist,” *J. Leukoc. Biol.*, vol. 78, no. 3, pp. 585–594, 2005, doi: 10.1189/jlb.0205074.

[2] S. Singh and H. S. Nalwa, “Nanotechnology and health safety - Toxicity and risk assessments of nanostructured materials on human health,” *J. Nanosci. Nanotechnol.*, vol. 7, no. 9, pp. 3048–3070, 2007, doi: 10.1166/jnn.2007.922.

[3] S. Mutluer, “The history of little things that changed our lives,” *Child’s Nerv. Syst.*, vol. 27, no. 10, pp. 1513–1520, 2011, doi: 10.1007/s00381-011-1517-7.

[4] I. Ijaz, E. Gilani, A. Nazir, and A. Bukhari, “Detail review on chemical, physical and green synthesis, classification, characterizations and applications of nanoparticles,” *Green Chem. Lett. Rev.*, vol. 13, no. 3, pp. 223–245, 2020, doi: 10.1080/17518253.2020.1802517.

[5] G. A. Silva, “Introduction to nanotechnology and its applications to medicine,” *Surg. Neurol.*, vol. 61, no. 3, pp. 216–220, 2004, doi: 10.1016/j.surneu.2003.09.036.

[6] S. Sahani and Y. C. Sharma, “Advancements in applications of nanotechnology in global food industry,” *Food Chem.*, vol. 342, no. May 2020, p. 128318, 2021, doi: 10.1016/j.foodchem.2020.128318.

[7] M. Usman *et al.*, “Nanotechnology in agriculture: Current status, challenges and future opportunities,” *Sci. Total Environ.*, vol. 721, p. 137778, 2020, doi: 10.1016/j.scitotenv.2020.137778.

[8] J. L. West and N. J. Halas, “Applications of nanotechnology to biotechnology: Commentary,” *Curr. Opin. Biotechnol.*, vol. 11, no. 2, pp. 215–217, 2000, doi: 10.1016/S0958-1669(00)00082-3.

[9] M. H. Ahmadi *et al.*, “Renewable energy harvesting with the application of nanotechnology: A review,” *Int. J. Energy Res.*, vol. 43, no. 4, pp. 1387–1410, 2019, doi: 10.1002/er.4282.

[10] Y. Zhang, M. Li, X. Gao, Y. Chen, and T. Liu, “Nanotechnology in cancer diagnosis: Progress, challenges and opportunities,” *J. Hematol. Oncol.*, vol. 12, no. 1, pp. 1–13, 2019, doi: 10.1186/s13045-019-0833-3.

[11] A. Muhaymin, U. A. Awan, A. Haider, and M. Naeem, “Nanotechnology for Cancer Biomarkers,” in *Cancer Biomarkers in Diagnosis and Therapeutics*, Springer, 2022, pp. 345–365.

[12] L. H. Pan, S. H. Kuo, T. Y. Lin, C. W. Lin, P. Y. Fang, and H. W. Yang, “An electrochemical biosensor to simultaneously detect VEGF and PSA for early prostate cancer diagnosis based on graphene oxide/ssDNA/PLLA nanoparticles,” *Biosens. Bioelectron.*, vol. 89, pp. 598–605, Mar. 2017, doi: 10.1016/J.BIOS.2016.01.077.

[13] Q. Ma, “Dual-mode electrochemical immunosensor based on Au@Ag NRs as double signal indicator for sensitive detection of HER2,” *J. Electrochem. Soc.*, vol. 168, no. 2, p. 027515, 2021, doi: 10.1149/1945-7111/abe56d.

[14] X. Fang, Y. Bando, U. K. Gautam, C. Ye, and D. Golberg, “Inorganic semiconductor nanostructures and their field-emission applications,” *J. Mater. Chem.*, vol. 18, no. 5, pp. 509–522, 2008, doi: 10.1039/b712874f.

[15] V. V. Pokropivny and V. V. Skorokhod, “New dimensionality classifications of nanostructures,” *Phys. E Low-Dimensional Syst. Nanostructures*, vol. 40, no. 7, pp. 2521–2525, 2008, doi: 10.1016/j.physe.2007.11.023.

[16] X. Fang, L. Hu, C. Ye, and L. Zhang, “One-dimensional inorganic semiconductor nanostructures: A new carrier for nanosensors,” *Pure Appl. Chem.*, vol. 82, no. 11, pp. 2185–2198, 2010, doi: 10.1351/PAC-CON-09-11-40.

[17] A. Ramanavicius *et al.*, “Prospects of nanostructure materials and their composites as antimicrobial agents,” *Front. Microbiol. | www.frontiersin.org*, vol. 1, p. 422, 2018, doi: 10.3389/fmicb.2018.00422.

[18] R. J. Martín-Palma, M. Manso, and V. Torres-Costa, “Optical biosensors based on semiconductor nanostructures,” *Sensors*, vol. 9, pp. 5149–5172, 2009, doi: 10.3390/s90705149.

[19] D. A. Neamen, “Semiconductor physics and devices: basic principles, ” 3rd ed. McGraw-Hill, 2003.

[20] T. L. Brown, H. E. LeMay, B. E. Bursten, and L. S. Brunauer, “Chemistry: The Central Science, ” *Pearson,* vol. 14. 2018, pp. 539–540.

[21] S. Suresh, “Semiconductor nanomaterials , methods and applications : A Review,” vol. 3, no. 3, pp. 62–74, 2013, doi: 10.5923/j.nn.20130303.06.

[22] R. Limpens, “Spectroscopical investigations of the space-separated quantum cutting mechanism,” Master thesis, van der Waals-Zeeman Institute, University of Amsterdam, Amsterdam, 2015. [Online]. https://www.researchgate.net/publication/280564604_Master_thesis

[23] D. Bimberg, *Nanoscience and technology - semiconductor nanostructures*, vol. 0, no. 0. 2008.

[24] F. Grillot, J. Duan, B. Dong, and H. Huang, “Uncovering recent progress in nanostructured light-emitters for information and communication technologies,” *Light Sci. Appl.*, vol. 10, no. 1, 2021, doi: 10.1038/s41377-021-00598-3.

[25] A. Medvid’, *The formation of nanocones on the surface of semiconductors by laser-induced self-assembly*. Woodhead Publishing Limited, 2012.

[26] J. Stangl, “Structural properties of self-organized semiconductor nanostructures,” vol. 76, no. July, pp. 725–783, 2004.

[27] Z. B. Li, W. Cai, and X. Chen, “Semiconductor quantum dots for in vivo,” *J. Nanosci. Nanotechnol.*, vol. 7, no. 8, pp. 2567–2581, 2007, doi: 10.1166/jnn.2007.628.

[28] O. Millo, D. Katz, Y. Cao, and U. Banin, “Imaging and spectroscopy of artificial-atom states in core/shell nanocrystal quantum dots,” *Phys. Rev. Lett.*, vol. 86, no. 25, pp. 5751–5754, 2001, doi: 10.1103/PhysRevLett.86.5751.

[29] J. L. Dye, “Electrides: Early examples of quantum confinement,” *Acc. Chem. Res.*, vol. 42, no. 10, pp. 1564–1572, 2009, doi: 10.1021/ar9000857.

[30] N. Liu and M. Tang, “Toxicity of different types of quantum dots to mammalian cells in vitro : An update review,” *J. Hazard. Mater.*, vol. 399, no. May, p. 122606, 2020, doi: 10.1016/j.jhazmat.2020.122606.

[31] Z. Zhang, T. Zheng, X. Li, J. Xu, and H. Zeng, “Progress of carbon quantum dots in photocatalysis applications,” *Part. Part. Syst. Charact.*, vol. 33, no. 8, pp. 457–472, 2016.

[32] W. A. A. Mohamed *et al.*, “Quantum dots synthetization and future prospect applications,” *Nanotechnol. Rev.*, vol. 10, no. 1, pp. 1926–1940, 2021, doi: 10.1515/ntrev-2021-0118.

[33] L. Wang, D. Xu, J. Gao, X. Chen, Y. Duo, and H. Zhang, “Semiconducting quantum dots: Modification and applications in biomedical science,” *Sci. China Mater.*, vol. 63, no. 9, pp. 1631–1650, 2020, doi: 10.1007/s40843-020-1330-7.

[34] P. Wu and X. P. Yan, “Doped quantum dots for chemo/biosensing and bioimaging,” *Chem. Soc. Rev.*, vol. 42, no. 12, pp. 5489–5521, 2013, doi: 10.1039/c3cs60017c.

[35] A. Das and P. T. Snee, “Synthetic developments of nontoxic quantum dots,” *ChemPhysChem.,* vol. 17, pp. 598-617, 2016, doi: 10.1002/cphc.201500837.

[36] X. Sun and Y. Lei, “Fluorescent carbon dots and their sensing applications,” *TrAC - Trends Anal. Chem.*, vol. 89, pp. 163–180, 2017, doi: 10.1016/j.trac.2017.02.001.

[37] N. Azam, M. Najabat Ali, and T. Javaid Khan, “Carbon quantum dots for bbiomedical applications: Review and analysis,” *Front. Mater.*, vol. 8, no. August, pp. 1–21, 2021, doi: 10.3389/fmats.2021.700403.

[38] Q. Zhao, W. Song, B. Zhao, and B. Yang, “Spectroscopic studies of the optical properties of carbon dots: Recent advances and future prospects,” *Mater. Chem. Front.*, vol. 4, no. 2, pp. 472–488, 2020, doi: 10.1039/c9qm00592g.

[39] A. Cayuela, M. L. Soriano, C. Carrillo-Carrión, and M. Valcárcel, “Semiconductor and carbon-based fluorescent nanodots: The need for consistency,” *Chem. Commun.*, vol. 52, no. 7, pp. 1311–1326, 2016, doi: 10.1039/c5cc07754k.

[40] C. Xia, S. Zhu, T. Feng, M. Yang, and B. Yang, “Evolution and synthesis of carbon dots: From carbon dots to carbonized polymer dots,” *Adv. Sci.*, vol. 6, no. 23, 2019, doi: 10.1002/advs.201901316.

[41] M. Sajid, “Nanomaterials: types, properties, recent advances, and toxicity concerns,” *Curr. Opin. Environ. Sci. Heal.*, vol. 25, p. 100319, 2022, doi: 10.1016/j.coesh.2021.100319.

[42] X. Xu *et al.*, “Electrophoretic analysis and purification of fluorescent single-walled carbon nanotube fragments,” *J. Am. Chem. Soc.*, vol. 126, no. 40, pp. 12736–12737, 2004, doi: 10.1021/ja040082h.

[43] Y. P. Sun *et al.*, “Quantum-sized carbon dots for bright and colorful photoluminescence,” *J. Am. Chem. Soc.*, vol. 128, no. 24, pp. 7756–7757, Jun. 2006, doi: 10.1021/JA062677D.

[44] L. Cao *et al.*, “Carbon dots for multiphoton bioimaging,” *J. Am. Chem. Soc.*, vol. 129, no. 37, pp. 11318–11319, 2007, doi: 10.1021/ja073527l.

[45] J. Zuo, T. Jiang, X. Zhao, X. Xiong, S. Xiao, and Z. Zhu, “Preparation and application of fluorescent carbon dots,” *J. Nanomater.*, vol. 2015, 2015, doi: 10.1155/2015/787862.

[46] X. Zhang *et al.*, “Highly sensitive humidity sensing properties of carbon quantum dots films,” *Mater. Res. Bull.*, vol. 48, no. 2, pp. 790–794, 2013, doi: 10.1016/j.materresbull.2012.11.056.

[47] K. J. Mintz, Y. Zhou, and R. M. Leblanc, “Recent development of carbon quantum dots regarding their optical properties, photoluminescence mechanism, and core structure,” *Nanoscale*, vol. 11, no. 11, pp. 4634–4652, 2019, doi: 10.1039/c8nr10059d.

[48] S. A. Hill, D. Benito-Alifonso, D. J. Morgan, S. A. Davis, M. Berry, and M. C. Galan, “Three-minute synthesis of sp^3 nanocrystalline carbon dots as non-toxic fluorescent platforms for intracellular delivery,” *Nanoscale*, vol. 8, no. 44, pp. 18630–18634, 2016, doi: 10.1039/c6nr07336k.

[49] B. P. de Oliveira and F. O. M. da Silva Abreu, “Carbon quantum dots synthesis from waste and by-products: Perspectives and challenges,” *Mater. Lett.*, vol. 282, p. 128764, 2021, doi: 10.1016/j.matlet.2020.128764.

[50] A. P. Demchenko and M. O. Dekaliuk, “Novel fluorescent carbonic nanomaterials for sensing and imaging,” *Methods Appl. Fluoresc.*, vol. 1, no. 4, 2013, doi: 10.1088/2050-6120/1/4/042001.

[51] P. Zuo, X. Lu, Z. Sun, Y. Guo, and H. He, “A review on syntheses, properties, characterization and bioanalytical applications of fluorescent carbon dots,” *Microchim. Acta*, vol. 183, no. 2, pp. 519–542, 2016, doi: 10.1007/s00604-015-1705-3.

[52] Z. Zhu, Y. Zhai, Z. Li, P. Zhu, and S. Mao, “Red carbon dots : Optical property regulations and applications,” no. June, 2019, doi: 10.1016/j.mattod.2019.05.003.

[53] X. Kou, S. Jiang, S. J. Park, and L. Y. Meng, “A review: recent advances in preparations and applications of heteroatom-doped carbon quantum dots,” *Dalt. Trans.*, vol. 49, no. 21, pp. 6915–6938, 2020, doi: 10.1039/d0dt01004a.

[54] L. Lin, Y. Luo, P. Tsai, J. Wang, and X. Chen, “Metal ions doped carbon quantum dots: Synthesis, physicochemical properties, and their applications,” *TrAC - Trends Anal. Chem.*, vol. 103, pp. 87–101, 2018, doi: 10.1016/j.trac.2018.03.015.

[55] F. Li, D. Yang, and H. Xu, “Non-metal-heteroatom-doped carbon dots: synthesis and properties,” *Chem. Eur. J.*, vol. 25, no. 5, pp. 1165–1176, 2019, doi: 10.1002/chem.201802793.

[56] Y. Park, J. Yoo, B. Lim, W. Kwon, and S.-W. Rhee, “Improving the functionality of carbon nanodots: doping and surface functionalization,” *J. Mater. Chem. A*, vol. 4, no. 30, pp. 11582–11603, 2016, doi: 10.1039/c6ta04813g.

[57] G. Kandasamy, “Recent advancements in doped/co-doped carbon quantum dots for multi-potential applications,” *C*, vol. 5, no. 2, p. 24, May 2019, doi: 10.3390/C5020024.

[58] R. Wang, K. Q. Lu, Z. R. Tang, and Y. J. Xu, “Recent progress in carbon quantum dots: synthesis, properties and applications in photocatalysis,” *J. Mater. Chem. A*, vol. 5, no. 8, pp. 3717–3734, 2017, doi: 10.1039/c6ta08660h.

[59] J. Zhou *et al.*, “An electrochemical avenue to blue luminescent nanocrystals from multiwalled carbon nanotubes (MWCNTs),” *J. Am. Chem. Soc.*, vol. 129, no. 4, pp. 744–745, 2007, doi: 10.1021/ja0669070.

[60] Y. P. Sun *et al.*, “Quantum-sized carbon dots for bright and colorful photoluminescence,” *J. Am. Chem. Soc.*, vol. 128, no. 24, pp. 7756–7757, 2006, doi: 10.1021/ja062677d.

[61] J. Deng *et al.*, “Electrochemical synthesis of carbon nanodots directly from alcohols,” *Chem. - A Eur. J.*, vol. 20, no. 17, pp. 4993–4999, 2014, doi: 10.1002/chem.201304869.

[62] M. Farshbaf, S. Davaran, F. Rahimi, N. Annabi, R. Salehi, and A. Akbarzadeh, “Carbon quantum dots: recent progresses on synthesis, surface modification and applications,” *Artif. Cells, Nanomedicine Biotechnol.*, vol. 46, no. 7, pp. 1331–1348, 2018, doi: 10.1080/21691401.2017.1377725.

[63] K. Hagiwara, S. Horikoshi, and N. Serpone, “Photoluminescent carbon quantum dots: Synthetic approaches and photophysical properties,” *Chem. Eur. J.*, vol. 27, no. 37, pp. 9466–9481, 2021.

[64] P. Namdari, B. Negahdari, and A. Eatemadi, “Synthesis, properties and biomedical applications of carbon-based quantum dots: An updated review,” *Biomed. Pharmacother.*, vol. 87, no. 88, pp. 209–222, 2017, doi: 10.1016/j.biopha.2016.12.108.

[65] I. Singh, R. Arora, H. Dhiman, and R. Pahwa, “Carbon quantum dots: Synthesis, characterization and biomedical applications,” *Turkish J. Pharm. Sci.*, vol. 15, no. 2, pp. 219–230, 2018, doi: 10.4274/tjps.63497.

[66] A. S. Rasal *et al.*, “Carbon quantum dots for energy applications: A review,” *ACS Appl. Nano Mater.*, vol. 4, no. 7, pp. 6515–6541, 2021, doi: 10.1021/acsanm.1c01372.

[67] Q. Xu *et al.*, “Heteroatom-doped carbon dots: synthesis, characterization, properties, photoluminescence mechanism and biological applications,” *J. Mater. Chem. B*, vol. 4, no. 45, pp. 7204–7219, 2016, doi: 10.1039/C6TB02131J.

[68] M. Li, T. Chen, J. J. Gooding, and J. Liu, “Review of carbon and graphene quantum dots for sensing,” *ACS Sensors*, vol. 4, no. 7, pp. 1732–1748, 2019, doi: 10.1021/acssensors.9b00514.

[69] A. Das and P. T. Snee, “Synthetic developments of nontoxic quantum dots,” *ChemPhysChem*, vol. 17, no. 5, pp. 598–617, 2016.

[70] Z. M. S. H. Khan, S. Saifi, Shumaila, Z. Aslam, S. A. Khan, and M. Zulfequar, “A facile one step hydrothermal synthesis of carbon quantum dots for label - free fluorescence sensing approach to detect picric acid in aqueous solution,” *J. Photochem. Photobiol. A Chem.*, vol. 388, no. October 2019, 2020, doi: 10.1016/j.jphotochem.2019.112201.

[71] U. A. Rani, L. Y. Ng, C. Y. Ng, and E. Mahmoudi, “A review of carbon quantum dots and their applications in wastewater treatment,” *Adv. Colloid Interface Sci.*, vol. 278, p. 102124, 2020, doi: 10.1016/j.cis.2020.102124.

[72] X. Luo, Y. Han, X. Chen, W. Tang, T. Yue, and Z. Li, “Carbon dots derived fluorescent nanosensors as versatile tools for food quality and safety assessment: A review,” *Trends Food Sci. Technol.*, vol. 95, no. March 2019, pp. 149–161, 2020, doi: 10.1016/j.tifs.2019.11.017.

[73] N. A. A. Nazri, N. H. Azeman, Y. Luo, and A. A. A Bakar, “Carbon quantum dots for optical sensor applications: A review,” *Opt. Laser Technol.*, vol. 139, no. January, p. 106928, 2021, doi: 10.1016/j.optlastec.2021.106928.

[74] R. M. El-Shabasy, M. Farouk Elsadek, B. M. Ahmed, M. F. Farahat, K. N. Mosleh, and M. M. Taher, “Recent developments in carbon quantum dots: properties, fabrication techniques, and bio-applications,” *Processes.,* vol. 9, no. 2, 2021, doi: 10.3390/pr9020388.

[75] T. Li, Z. Li, T. Huang, and L. Tian, “Carbon quantum dot-based sensors for food safety,” *Sensors Actuators, A Phys.*, vol. 331, p. 113003, 2021, doi: 10.1016/j.sna.2021.113003.

[76] Z. W. Heng, W. C. Chong, Y. L. Pang, and C. H. Koo, “An overview of the recent advances of carbon quantum dots/metal oxides in the application of heterogeneous photocatalysis in photodegradation of pollutants towards visible-light and solar energy exploitation,” *J. Environ. Chem. Eng.*, vol. 9, no. 3, p. 105199, 2021, doi: 10.1016/j.jece.2021.105199.

[77] R. Atchudan, T. N. Jebakumar Immanuel Edison, M. Shanmugam, S. Perumal, T. Somanathan, and Y. R. Lee, “Sustainable synthesis of carbon quantum dots from banana peel waste using hydrothermal process for in vivo bioimaging,” *Phys. E Low-Dimensional Syst. Nanostructures*, vol. 126, no. August 2020, p. 114417, 2021, doi: 10.1016/j.physe.2020.114417.

[78] S. S. Arumugam *et al.*, “Facile preparation of fluorescent carbon quantum dots from denatured sour milk and its multifunctional applications in the fluorometric determination of gold ions, in vitro bioimaging and fluorescent polymer film,” *J. Photochem. Photobiol. A Chem.*, vol. 401, no. July, 2020, doi: 10.1016/j.jphotochem.2020.112788.

[79] W. Su *et al.*, “Red-Emissive Carbon Quantum Dots for Nuclear Drug Delivery in Cancer Stem Cells,” *J. Phys. Chem. Lett*, vol. 11, p. 39, 2020, doi: 10.1021/acs.jpclett.9b03891.

[80] X. W. Hua, Y. W. Bao, Z. Chen, and F. G. Wu, “Carbon quantum dots with intrinsic mitochondrial targeting ability for mitochondria-based theranostics,” *Nanoscale*, vol. 9, no. 30, pp. 10948–10960, 2017, doi: 10.1039/c7nr03658b.

[81] H. Li *et al.*, “Carbon quantum dots with photo-generated proton property as efficient visible light controlled acid catalyst,” *Nanoscale*, vol. 6, no. 2, pp. 867–873, 2014, doi: 10.1039/c3nr03996j.

[82] S. Sahu *et al.*, “Visible-light photoconversion of carbon dioxide into organic acids in an aqueous solution of carbon dots,” *Langmuir*, vol. 30, no. 28, pp. 8631–8636, 2014, doi: 10.1021/la5010209.

[83] V. C. Hoang, K. Dave, and V. G. Gomes, “Carbon quantum dot-based composites for energy storage and electrocatalysis: Mechanism, applications and future prospects,” *Nano Energy*, vol. 66, no. August, p. 104093, 2019, doi: 10.1016/j.nanoen.2019.104093.

[84] W. Li *et al.*, “Carbon-quantum-dots-loaded ruthenium nanoparticles as an efficient electrocatalyst for hydrogen production in alkaline media,” *Adv. Mater.*, vol. 30, no. 31, p. 1800676, 2018.

[85] S. Yang, R. Du, Y. Yu, Z. Zhang, and F. Wang, “One-step electrodeposition of carbon quantum dots and transition metal ions for N-doped carbon coupled with NiFe oxide clusters: A high-performance electrocatalyst for oxygen evolution,” *Nano Energy*, vol. 77, no. February, p. 105057, 2020, doi: 10.1016/j.nanoen.2020.105057.

[86] M. S. Balogun *et al.*, “Carbon Quantum Dot Surface-Engineered VO2 Interwoven Nanowires: A Flexible Cathode Material for Lithium and Sodium Ion Batteries,” *ACS Appl. Mater. Interfaces*, vol. 8, no. 15, pp. 9733–9744, 2016, doi: 10.1021/acsami.6b01305.

[87] M. Jing *et al.*, “Carbon quantum dot coated Mn_3O_4 with enhanced performances for lithium-ion batteries,” *J. Mater. Chem. A*, vol. 3, no. 32, pp. 16824–16830, 2015, doi: 10.1039/c5ta03610k.

[88] S. Ying Lim, W. Shen, and Z. Gao, “Carbon quantum dots and their applications,” *This J. is Cite this Chem. Soc. Rev*, vol. 44, p. 362, 2015, doi: 10.1039/c4cs00269e.

[89] R. Zhang and W. Chen, “Nitrogen-doped carbon quantum dots: Facile synthesis and application as a ‘turn-off’ fluorescent probe for detection of Hg^{2+} ions,” *Biosens. Bioelectron.*, vol. 55, pp. 83–90, 2013, doi: 10.1016/j.bios.2013.11.074.

[90] J. Zong *et al.*, “Carbon dots as fluorescent probes for ‘off-on’ detection of Cu^{2+} and l-cysteine in aqueous solution,” *Biosens. Bioelectron.*, vol. 51, pp. 330–335, 2014, doi: 10.1016/j.bios.2013.07.042.

[91] H. Zhang *et al.*, “Determination of iodide via direct fluorescence quenching at nitrogen-doped carbon quantum dot fluorophores,” *Environ. Sci. Technol. Lett*, vol. 1, p. 5, 2014, doi: 10.1021/ez400137j.

[92] H. Huang, Y. Weng, L. Zheng, B. Yao, W. Weng, and X. Lin, “Nitrogen-doped carbon quantum dots as fluorescent probe for ‘off-on’ detection of mercury ions, L-cysteine and iodide ions,” *J. Colloid Interface Sci.*, vol. 506, pp. 373–378, 2017, doi: 10.1016/j.jcis.2017.07.076.

[93] A. H. Loo, Z. Sofer, D. Bouša, P. Ulbrich, A. Bonanni, and M. Pumera, “Carboxylic carbonqQuantum dts as a fluorescent sensing platform for DNA detection,” *ACS Appl. Mater. Interfaces*, vol. 8, no. 3, pp. 1951–1957, 2016, doi: 10.1021/acsami.5b10160.

[94] B. Kumari, R. Kumari, and P. Das, “Visual detection of G-quadruplex with mushroom derived highly fluorescent carbon quantum dots,” *J. Pharm. Biomed. Anal.*, vol. 157, pp. 137–144, 2018, doi: 10.1016/j.jpba.2018.05.013.

[95] I. Rubin and Y. Yarden, “The basic biology of HER2,” *Ann. Oncol.*, vol. 12, no. 1, pp. S3–S8, 2001, doi: 10.1093/annonc/12.suppl_1.S3.

[96] R. S. Herbst, “Review of epidermal growth factor receptor biology,” *Int. J. Radiat. Oncol. Biol. Phys.*, vol. 59, no. 2, pp. S21–S26, 2004, doi: 10.1016/j.ijrobp.2003.11.041.

[97] E. Tagliabue, A. Balsari, M. Campiglio, and S. M. Pupa, “HER2 as a target for breast cancer therapy,” *Expert Opin. Biol. Ther.*, vol. 10, no. 5, pp. 711–724, 2010, doi: 10.1517/14712591003689972.

[98] C. Marchiò, L. Annaratone, A. Marques, L. Casorzo, E. Berrino, and A. Sapino, “Evolving concepts in HER2 evaluation in breast cancer: Heterogeneity, HER2-low carcinomas and beyond,” *Semin. Cancer Biol.*, vol. 72, pp. 123–135, 2021, doi: 10.1016/j.semcancer.2020.02.016.

[99] L. Wilkinson and T. Gathani, “Understanding breast cancer as a global health concern,” *Br. J. Radiol.*, vol. 95, no. 1130, pp. 7–9, 2022, doi: 10.1259/BJR.20211033.

[100] S. Ahn, J. W. Woo, K. Lee, and S. Y. Park, “HER2 status in breast cancer: Changes in guidelines and complicating factors for interpretation,” *J. Pathol. Transl. Med.*, vol. 54, no. 1, pp. 34–44, 2020, doi: 10.4132/jptm.2019.11.03.

[101] Yarden Y, “Biology of HER2 and its importance in breast Cancer,” *Oncology*, vol. 61, no. 2, pp. 1–13, 2001.

[102] C. Marchini *et al.*, “HER2-driven carcinogenesis: New mouse models for novei Immunotherapies,” *Oncogene Cancer - From Bench to Clin.*, no. May, 2013, doi: 10.5772/53880.

[103] J. A. Kretzmann, K. L. Irving, N. M. Smith, and C. W. Evans, “Modulating gene expression in breast cancer via DNA secondary structure and the CRISPR toolbox,” vol. 3, no. 4, 2021, doi: 10.1093/narcan/zcab048.

[104] S. Asamitsu, S. Obata, Z. Yu, T. Bando, and H. Sugiyama, “Recent progress of targeted G-quadruplex-preferred ligands toward cancer therapy,” *Molecules*, vol. 24, no. 3, 2019, doi: 10.3390/MOLECULES24030429.

[105] T. Zhang, H. Zhang, Y. Wang, and L. B. Mcgown, “Capture and identification of proteins that bind to a GGA-rich sequence from the ERBB2 gene promoter region,” *Analytical and bioanalytical chemistry,* vol. 404, no. 6, pp. 1867-1876, 2012, doi: 10.1007/s00216-012-6322-y.

[106] S. Ebbinghaus, “Specific Inhibition of HER-2/neu Transcription Initiation,” p. 25, Jul. 2006.

[107] F. Y. Teng *et al.*, “G-quadruplex DNA: a novel target for drug design,” *Cell. Mol. Life Sci.*, vol. 78, no. 19–20, pp. 6557–6583, 2021, doi: 10.1007/s00018-021-03921-8.

[108] R. V. Brown, V. C. Gaerig, T. Simmons, and T. A. Brooks, “Helping eve overcome ADAM: G-quadruplexes in the ADAM-15 promoter as new molecular targets for breast cancer therapeutics,” *Molecules*, vol. 18, no. 12, pp. 15019–15034, 2013, doi: 10.3390/molecules181215019.

[109] X. Cui, H. Chen, Q. Zhang, M. Xu, G. Yuan, and J. Zhou, “Exploration of the structure and recognition of a G-quadruplex in the her2 proto-oncogene promoter and its transcriptional regulation,” *Sci. Rep.*, vol. 9, no. 1, pp. 1–12, 2019, doi: 10.1038/s41598-019-39941-5.

[110] C. Pratt and K. Cornely, *Essential Biochemistry*. John Wiley & Sons, Inc., 2012.

[111] A. Singh, M. P. Singh, V. Sharma, H. N. Verma, and K. Arora, "Molecular Techniques." *Chemical Analysis of Food: Techniques and Applications*., pp. 401, 2012, doi: 10.1016/b978-0-12-384862-8.00018-2.

[112] S. Minchin and J. Lodge, “Understanding biochemistry: Structure and function of nucleic acids,” *Essays Biochem.*, vol. 63, no. 4, pp. 433–456, 2019, doi: 10.1042/EBC20180038.

[113] L. Roewer, “DNA fingerprinting in forensics: Past, present, future,” *Investig. Genet.*, vol. 4, no. 1, pp. 1–10, 2013, doi: 10.1186/2041-2223-4-22.

[114] I. Palchetti and M. Mascini, “Nucleic acid biosensors for environmental pollution monitoring,” *Analyst*, vol. 133, no. 7, pp. 846–854, 2008, doi: 10.1039/b802920m.

[115] M. Passamano and M. Pighini, “QCM DNA-sensor for GMOs detection,” *Sensors Actuators, B Chem.*, vol. 118, no. 1–2, pp. 177–181, 2006, doi: 10.1016/j.snb.2006.04.012.

[116] D. A. Dean, “Peptide nucleic acids: Versatile tools for gene therapy strategies,” *Adv. Drug Deliv. Rev.*, vol. 44, no. 2–3, pp. 81–95, 2000, doi: 10.1016/S0169-409X(00)00087-9.

[117] A. Hashem *et al.*, “Nucleic acid-based electrochemical biosensors for rapid clinical diagnosis: advances, challenges, and opportunities,” *Crit. Rev. Clin. Lab. Sci.*, vol. 59, no. 3, pp. 156–177, 2022, doi: 10.1080/10408363.2021.1997898.

[118] R. Saad, “Discovery, development, and current applications of DNA identity testing,” *Baylor Univ. Med. Cent. Proc.*, vol. 18, no. 2, pp. 130–133, 2005, doi: 10.1080/08998280.2005.11928051.

[119] S. Tombelli, M. Mascini, C. Sacco, and A. P. F. Turner, “A DNA piezoelectric biosensor assay coupled with a polymerase chain reaction for bacterial toxicity determination in environmental samples,” *Anal. Chim. Acta*, vol. 418, no. 1, pp. 1–9, 2000, doi: 10.1016/S0003-2670(00)00943-0.

[120] Z. Yu *et al.*, “Efficient gene therapy of pancreatic cancer via a peptide nucleic acid (PNA)-loaded layered double hydroxides (LDH) Nanoplatform,” *Small*, vol. 16, no. 23, pp. 1–10, 2020, doi: 10.1002/smll.201907233.

[121] Y. Zhao *et al.*, “Nucleic acids analysis,” *Sci China Chem*, vol. 64, no. 2, pp. 171–203, 2021, doi: 10.1007/s11426-020-9864-7.

[122] J. D. Harvey, H. A. Baker, M. V. Ortiz, A. Kentsis, and D. A. Heller, “HIV detection via a carbon nanotube RNA sensor,” *ACS Sensors*, vol. 4, no. 5, pp. 1236–1244, 2019, doi: 10.1021/acssensors.9b00025.

[123] H. B. Wang, L. H. Ma, T. Zhang, K. C. Huang, Y. Di Zhao, and T. C. Liu, “Simple and accurate visual detection of single nucleotide polymorphism based on colloidal gold nucleic acid strip biosensor and primer-specific PCR,” *Anal. Chim. Acta*, vol. 1093, pp. 106–114, 2020, doi: 10.1016/j.aca.2019.09.048.

[124] H. Zhang *et al.*, "A DNA tetrahedral structure-mediated ultrasensitive fluorescent microarray platform for nucleic acid test," *Sensors Actuators, B Chem.*, vol. 321, no. June, 2020, doi: 10.1016/j.snb.2020.128538.

[125] G. Ammanath *et al.*, "Flow-through colorimetric assay for detection of nucleic acids in plasma," *Anal. Chim. Acta*, vol. 1066, pp. 102–111, 2019, doi: 10.1016/j.aca.2019.03.036.

[126] M. Bartosik and L. Jirakova, "Electrochemical analysis of nucleic acids as potential cancer biomarkers," *Curr. Opin. Electrochem.*, vol. 14, pp. 96–103, 2019, doi: 10.1016/j.coelec.2019.01.002.

[127] Z. Wang *et al.*, "Nucleic acid-based ratiometric electrochemiluminescent, electrochemical and photoelectrochemical biosensors: a review," *Microchim. Acta*, vol. 186, no. 7, 2019, doi: 10.1007/s00604-019-3514-6.

[128] A. Suea-Ngam, L. Bezinge, B. Mateescu, P. D. Howes, A. J. Demello, and D. A. Richards, "Enzyme-sssisted nucleic acid detection for infectious disease diagnostics: Moving toward the point-of-care," *ACS Sensors*, vol. 5, no. 9, pp. 2701–2723, 2020, doi: 10.1021/acssensors.0c01488.

[129] J. R. Epstein, I. Biran, and D. R. Walt, *Fluorescence-based nucleic acid detection and microarrays*, vol. 469, no. 1. 2002, doi: 10.1016/s0003-2670(02)00030-2.

[130] A. Piriya V.S, P. Joseph, K. Daniel S.C.G., S. Lakshmanan, T. Kinoshita, and S. Muthusamy, "Colorimetric sensors for rapid detection of various analytes," *Mater. Sci. Eng. C*, vol. 78, pp. 1231–1245, 2017, doi: 10.1016/j.msec.2017.05.018.

[131] T. Yang, Z. Luo, Y. Tian, C. Qian, and Y. Duan, "Design strategies of AuNPs-based nucleic acid colorimetric biosensors," *TrAC - Trends Anal. Chem.*, vol. 124, p. 115795, 2020, doi: 10.1016/j.trac.2019.115795.

[132] H. Li and L. Rothberg, “Colorimetric detection of DNA sequences based on electrostatic interactions with unmodified gold nanoparticles,” *Proc. Natl. Acad. Sci. U. S. A.*, vol. 101, no. 39, pp. 14036–14039, 2004, doi: 10.1073/pnas.0406115101.

[133] D. Vilela, M. C. González, and A. Escarpa, “Sensing colorimetric approaches based on gold and silver nanoparticles aggregation: Chemical creativity behind the assay. A review,” *Anal. Chim. Acta*, vol. 751, pp. 24–43, 2012, doi: 10.1016/j.aca.2012.08.043.

[134] K. S. Park, M. Il Kim, D. Cho, and H. G. Park, “Label-free colorimetric detection of nucleic acids based on target-induced shielding against the peroxidase-mimicking activity of magnetic nanoparticles,” *Small*, vol. 7, no. 11, pp. 1521–1525, 2011.

[135] Y. Song, K. Qu, C. Zhao, J. Ren, and X. Qu, “Graphene oxide: intrinsic peroxidase catalytic activity and its application to glucose detection,” *Adv. Mater.*, vol. 22, no. 19, pp. 2206–2210, 2010.

[136] T. M. H Lee, L. Yin Chau, Q. He, A. Qin, and S. Ping Yip, “Platinum nanoparticles on reduced graphene oxide as peroxidase mimetics for the colorimetric detection of specific DNA sequence Platinum nanoparticles on reduced graphene oxide as peroxidase mimetics for the colorimetric detection of specific DNA sequence ,” *J. Mater. Chem. B*, vol. 4, p. 4076, doi: 10.1039/c6tb00741d.

[137] W. Chen, X. Fang, H. Li, H. Cao, and J. Kong, “DNA-mediated inhibition of peroxidase-like activities on platinum nanoparticles for simple and rapid colorimetric detection of nucleic acids,” *Biosens. Bioelectron.*, vol. 94, no. February, pp. 169–175, 2017, doi: 10.1016/j.bios.2017.02.025.

[138] M. H. Jazayeri, T. Aghaie, A. Avan, A. Vatankhah, and M. R. S. Ghaffari, “Colorimetric detection based on gold nano particles (GNPs): An easy, fast, inexpensive, low-cost and short time method in detection of analytes (protein, DNA, and ion),” *Sens. Bio-Sensing Res.*, vol. 20, no. March, pp. 1–8, 2018, doi: 10.1016/j.sbsr.2018.05.002.

[139] Y. L. Jung, C. Jung, H. Parab, T. Li, and H. G. Park, “Direct colorimetric diagnosis of pathogen infections by utilizing thiol-labeled PCR primers and unmodified gold nanoparticles,” *Biosens. Bioelectron.*, vol. 25, no. 8, pp. 1941–1946, 2010, doi: 10.1016/j.bios.2010.01.010.

[140] J. Ge *et al.*, “Fluorometric determination of nucleic acids based on the use of polydopamine nanotubes and target-induced strand displacement amplification,” *Microchim. Acta*, vol. 185, no. 2, pp. 1–7, 2018, doi: 10.1007/s00604-017-2632-2.

[141] J. H. Choi, T. Ha, M. Shin, S. N. Lee, and J. W. Choi, “Nanomaterial-based fluorescence resonance energy transfer (Fret) and metal-enhanced fluorescence (mef) to detect nucleic acid in cancer diagnosis,” *Biomedicines*, vol. 9, no. 8, 2021, doi: 10.3390/biomedicines9080928.

[142] B. Juskowiak, “Nucleic acid-based fluorescent probes and their analytical potential,” *Anal. Bioanal. Chem.*, vol. 399, no. 9, pp. 3157–3176, 2011, doi: 10.1007/s00216-010-4304-5.

[143] Y. Du and S. Dong, “Nucleic acid biosensors: Recent advances and perspectives,” *Anal. Chem.*, vol. 89, no. 1, pp. 189–215, 2017, doi: 10.1021/acs.analchem.6b04190.

[144] G. T. Hirons, J. J. Fawcett, and H. A. Crissman, “TOTO and YOYO: New very bright fluorochromes for DNA content analyses by flow cytometry,” *Cytometry*, vol. 15, no. 2, pp. 129–140, 1994, doi: 10.1002/cyto.990150206.

[145] X. Wang and U. J. Krull, “Tethered thiazole orange intercalating dye for development of fibre-optic nucleic acid biosensors,” *Anal. Chim. Acta*, vol. 470, no. 1, pp. 57–70, 2002, doi: 10.1016/S0003-2670(02)00671-2.

[146] H. Yang, F. Fu, W. Li, W. Wei, Y. Zhang, and S. Liu, “Telomerase and poly(ADP-ribose) polymerase-1 activity sensing based on the high fluorescence selectivity and sensitivity of TOTO-1 towards G bases in single-stranded DNA and poly(ADP-ribose),” *Chem. Sci.*, vol. 10, no. 13, pp. 3706–3714, 2019, doi: 10.1039/c8sc05770b.

[147] A. Moulick *et al.*, “Using CdTe/ZnSe core/shell quantum dots to detect DNA and damage to DNA,” *Int. J. Nanomedicine*, vol. 12, pp. 1277–1291, 2017, doi: 10.2147/IJN.S121840.

[148] Y. S. Kim, B. C. Kim, J. H. Lee, J. Kim, and M. B. Gu, “Specific detection of DNA using quantum dots and magnetic beads for large volume samples,” *Biotechnol. Bioprocess Eng.*, vol. 11, no. 5, pp. 449–454, 2006, doi: 10.1007/BF02932313.

[149] E. Bilgen, M. Forough, and Ö. Persil Çetinkol, “A conjugated gold nanoparticle-azacyanine off-on-off fluorescence probe for sensitive and selective detection of G-quadruplexes,” *Talanta*, vol. 217, no. March, p. 121076, 2020, doi: 10.1016/j.talanta.2020.121076.

[150] Y. W. Hartati, L. K. Letelay, S. Gaffar, S. Wyantuti, and H. H. Bahti, “Cerium oxide-monoclonal antibody bioconjugate for electrochemical immunosensing of HER2 as a breast cancer biomarker,” *Sens. Bio-Sensing Res.*, vol. 27, no. August 2019, p. 100316, 2020, doi: 10.1016/j.sbsr.2019.100316.

[151] L. M. Rossi, L. Shi, N. Rosenzweig, and Z. Rosenzweig, “Fluorescent silica nanospheres for digital counting bioassay of the breast cancer marker HER2/nue,” *Biosens. Bioelectron.*, vol. 21, no. 10, pp. 1900–1906, 2006, doi: 10.1016/j.bios.2006.02.002.

[152] H. Ehzari, M. Samimi, M. Safari, and M. B. Gholivand, “Label-free electrochemical immunosensor for sensitive HER2 biomarker detection using the core-shell magnetic metal-organic frameworks,” *J. Electroanal. Chem.*, vol. 877, p. 114722, 2020, doi: 10.1016/j.jelechem.2020.114722.

[153] D. J. Slamon *et al.*, “HER-2/neu Proto-oncogene in Human Bresat and Ovarian Cancer,” *Science.*, vol. 244, pp. 707–712, 1989, doi: 10.1126/science.2470152.

[154] D. Furrer, F. Sanschagrin, S. Jacob, and C. Diorio, “Advantages and disadvantages of technologies for HER2 Testing in Breast Cancer Specimens,” *Am. J. Clin. Pathol.*, vol. 144, no. 5, pp. 686–703, 2015, doi: 10.1309/AJCPT41TCBUEVDQC.

[155] I. L. Andrulis *et al.*, “neu/erbB-2 amplification identifies a poor-prognosis group of women with node-negative breast cancer,” *J. Clin. Oncol.*, vol. 16, no. 4, pp. 1340–1349, Apr. 1998, doi: 10.1200/JCO.1998.16.4.1340.

[156] A. Jukkola, R. Bloigu, Y. Soini, E. R. Savolainen, K. Holli, and G. Blanco, “c-erbB-2 Positivity is a factor for poor prognosis in breast cancer and poor response to hormonal or chemotherapy treatment in advanced disease,” *Eur. J. Cancer*, vol. 37, no. 3, pp. 347–354, 2001, doi: 10.1016/S0959-8049(00)00395-6.

[157] J. Luo, D. Liang, X. Qiu, and M. Yang, “Photoelectrochemical detection of breast cancer biomarker based on hexagonal carbon nitride tubes,” *Anal. Bioanal. Chem.*, vol. 411, no. 26, pp. 6889–6897, 2019, doi: 10.1007/s00216-019-02060-1.

[158] X. Guo, S. Liu, M. Yang, H. Du, and F. Qu, “Dual signal amplification photoelectrochemical biosensor for highly sensitive human epidermal growth factor receptor-2 detection,” *Biosens. Bioelectron.*, vol. 139, no. May, p. 111312, 2019, doi: 10.1016/j.bios.2019.05.017.

[159] J. Luo *et al.*, “Photoelectrochemical detection of human epidermal growth factor receptor 2 (HER2) based on Co_3O_4-ascorbic acid oxidase as multiple signal amplifier,” *Microchim. Acta*, vol. 188, no. 5, 2021, doi: 10.1007/s00604-021-04829-7.

[160] J. G. Pacheco, P. Rebelo, M. Freitas, H. P. A. Nouws, and C. Delerue-Matos, “Breast cancer biomarker (HER2-ECD) detection using a molecularly imprinted electrochemical sensor,” *Sensors Actuators, B Chem.*, vol. 273, no. June, pp. 1008–1014, 2018, doi: 10.1016/j.snb.2018.06.113.

[161] M. Freitas, M. M. P. S. Neves, H. P. A. Nouws, and C. Delerue-Matos, “Quantum dots as nanolabels for breast cancer biomarker HER2-ECD analysis in human serum,” *Talanta*, vol. 208, no. June 2019, p. 120430, 2020, doi: 10.1016/j.talanta.2019.120430.

[162] D. Ou, D. Sun, X. Lin, Z. Liang, Y. Zhong, and Z. Chen, “A dual-aptamer-based biosensor for specific detection of breast cancer biomarker HER2 via flower-like nanozymes and DNA nanostructures,” *J. Mater. Chem. B*, vol. 7, no. 23, pp. 3661–3669, 2019, doi: 10.1039/c9tb00472f.

[163] Z. M. A. N. H. Lah, S. A. A. Ahmad, M. S. Zaini, and M. A. Kamarudin, “An electrochemical sandwich immunosensor for the detection of HER2 using antibody-conjugated PbS quantum dot as a label,” *J. Pharm. Biomed. Anal.*, vol. 174, pp. 608–617, 2019, doi: 10.1016/j.jpba.2019.06.024.

[164] A. A. Lahcen *et al.*, “Laser-scribed graphene sensor based on gold nanostructures and molecularly imprinted polymers: Application for Her-2 cancer biomarker detection,” *Sensors Actuators B Chem.*, vol. 347, no. July, pp. 1–12, 2021, doi: 10.1016/j.snb.2021.130556.

[165] X. Li, C. Shen, M. Yang, and A. Rasooly, “Polycytosine DNA electric-current-generated immunosensor for electrochemical detection of human epidermal growth factor receptor 2 (HER2),” *Anal. Chem.*, vol. 90, no. 7, pp. 4764–4769, 2018, doi: 10.1021/acs.analchem.8b00023.

[166] P. F. Rostamabadi and E. Heydari-Bafrooei, “Impedimetric aptasensing of the breast cancer biomarker HER2 using a glassy carbon electrode modified with gold nanoparticles in a composite consisting of electrochemically reduced graphene oxide and single-walled carbon nanotubes,” *Microchim. Acta*, vol. 186, no. 8, 2019, doi: 10.1007/s00604-019-3619-y.

[167] X. Geng, M. Shi, H. Ning, C. Feng, and Y. Guan, “A compact and low-cost laser induced fluorescence detector with silicon based photodetector assembly for capillary flow systems,” *Talanta*, vol. 182, no. January, pp. 279–284, 2018, doi: 10.1016/j.talanta.2018.01.076.

[168] V. Ranganathan, S. Srinivasan, A. Singh, and M. C. DeRosa, “An aptamer-based colorimetric lateral flow assay for the detection of human epidermal growth factor receptor 2 (HER2),” *Anal. Biochem.*, vol. 588, no. October 2019, p. 113471, 2020, doi: 10.1016/j.ab.2019.113471.

[169] M. Li *et al.*, “A multifunctional mesoporous silica-gold nanocluster hybrid platform for selective breast cancer cell detection using a catalytic amplification-based colorimetric assay,” *Nanoscale*, vol. 11, no. 6, pp. 2631–2636, 2019, doi: 10.1039/c8nr08337a.

[170] H. Xing, T. Wei, X. Lin, and Z. Dai, “Near-infrared MnCuInS/ZnS@BSA and urchin-like Au nanoparticle as a novel donor-acceptor pair for enhanced FRET biosensing,” *Anal. Chim. Acta*, vol. 1042, pp. 71–78, 2018, doi: 10.1016/j.aca.2018.05.048.

[171] M. Wang, D. Yue, Q. Qiao, L. Miao, H. Zhao, and Z. Xu, “Aptamer based fluorescent probe for serum HER2-ECD detection: The clinical utility in breast cancer,” *Chinese Chem. Lett.*, vol. 29, no. 5, pp. 703–706, 2018, doi: 10.1016/j.cclet.2018.03.025.

[172] M. Zhang, G. Gao, Y. Ding, C. Deng, J. Xiang, and H. Wu, “A fluorescent aptasensor for the femtomolar detection of epidermal growth factor receptor-2 based on the proximity of G-rich sequences to Ag nanoclusters,” *Talanta*, vol. 199, no. November 2018, pp. 238–243, 2019, doi: 10.1016/j.talanta.2019.02.014.

[173] Y. Wu *et al.*, “Quantum dot–based FRET immunoassay for HER2 using ultrasmall affinity proteins,” *Small*, vol. 14, no. 35, p. 1802266, 2018, doi: 10.1002/smll.201802266.

[174] S. I. Tanaka, H. Wadati, K. Sato, H. Yasuda, and H. Niioka, “Red-fluorescent Pt nanoclusters for detecting and imaging HER2 in breast cancer cells,” *ACS Omega*, vol. 5, no. 37, pp. 23718–23723, 2020, doi: 10.1021/acsomega.0c02578.

[175] M. Shamsipur, M. Emami, L. Farzin, and R. Saber, “A sandwich-type electrochemical immunosensor based on in situ silver deposition for determination of serum level of HER2 in breast cancer patients,” *Biosens. Bioelectron.*, vol. 103, no. September 2017, pp. 54–61, 2018, doi: 10.1016/j.bios.2017.12.022.

[176] M. Bilous *et al.*, “Assessing HER2 amplification in breast cancer: findings from the Australian In Situ Hybridization Program,” *Breast Cancer Res Treat*, vol. 134, pp. 617–624, 2012, doi: 10.1007/s10549-012-2093-6.

[177] D. G. Hicks and R. R. Tubbs, “Assessment of the HER2 status in breast cancer by fluorescence in situ hybridization: A technical review with interpretive guidelines,” *Hum. Pathol.*, vol. 36, no. 3, pp. 250–261, 2005, doi: 10.1016/j.humpath.2004.11.010.

[178] R. L. Ridolfi, M. R. Jamehdor, and J. M. Arber, “HER-2/neu Testing in Breast Carcinoma: A Combined Immunohistochemical and Fluorescence In Situ Hybridization Approach,” *Mod Pathol.,* vol. 13, pp. 866-873, 2000, doi: 10.1038/modpathol.3880154.

[179] Y. Chen, L. Liu, R. Ni, and W. Zhou, “Advances in HER2 testing”, *Advances in Clinical Chemistry*, vol. 91, 2019, doi: 10.1016/bs.acc.2019.03.004.

[180] F. Yeasmin Khusbu, X. Zhou, H. Chen, C. Ma, and K. Wang, “Thioflavin T as a fluorescence probe for biosensing applications,” *TrAC - Trends Anal. Chem.*, vol. 109, pp. 1–18, 2018, doi: 10.1016/j.trac.2018.09.013.

[181] M. Amjadi, T. Hallaj, and F. Mirbirang, “A chemiluminescence reaction consisting of manganese (IV), sodium sulfite, and sulfur-and nitrogen-doped carbon quantum dots, and its application for the determination of oxytetracycline,” *Microchim. Acta*, vol. 187, no. 3, pp. 1–7, 2020.

[182] M. Amjadi, J. L. Manzoori, T. Hallaj, and N. Azizi, “Sulfur and nitrogen co-doped carbon quantum dots as the chemiluminescence probe for detection of Cu^{2+} ions,” *J. Lumin.*, vol. 182, pp. 246–251, 2017, doi: 10.1016/j.jlumin.2016.10.021.

[183] H. Wu, J. Jiang, X. Gu, and C. Tong, “Nitrogen and sulfur co-doped carbon quantum dots for highly selective and sensitive fluorescent detection of Fe(III) ions and L-cysteine,” *Microchim. Acta*, vol. 184, no. 7, pp. 2291–2298, 2017, doi: 10.1007/s00604-017-2201-8.

[184] F. Akhgari, N. Samadi, K. Farhadi, and M. Akhgari, “A green one-pot synthesis of nitrogen and sulfur co-doped carbon quantum dots for sensitive and selective detection of cephalexin,” *Can. J. Chem.*, vol. 95, no. 6, pp. 641–648, 2017, doi: 10.1139/cjc-2016-0531.

[185] J. Chen, J. Liu, J. Li, L. Xu, and Y. Qiao, “One-pot synthesis of nitrogen and sulfur co-doped carbon dots and its application for sensor and multicolor cellular imaging,” *J. Colloid Interface Sci.*, vol. 485, pp. 167–174, 2017, doi: 10.1016/j.jcis.2016.09.040.

[186] S. Liao *et al.*, “Talanta Novel S , N-doped carbon quantum dot-based " o ff - on " fl uorescent sensor for silver ion and cysteine,” *Talanta*, vol. 180, no. December 2017, pp. 300–308, 2018, doi: 10.1016/j.talanta.2017.12.040.

[187] X. Qie *et al.*, “One-step synthesis of nitrogen, sulfur co-doped carbon nanodots and application for Fe3+ detection,” *J. Mater. Chem. B*, vol. 6, no. 21, pp. 3549–3554, 2018, doi: 10.1039/c8tb00193f.

[188] Y. Wang *et al.*, “Synthesis of N,S-doped carbon quantum dots for use in organic solar cells as the ZnO modifier to eliminate the light-soaking effect,” *ACS Appl. Mater. Interfaces*, vol. 11, no. 2, pp. 2243–2253, 2019, doi: 10.1021/acsami.8b17128.

[189] Q. Liang, W. Ma, Y. Shi, Z. Li, and X. Yang, “Easy synthesis of highly fluorescent carbon quantum dots from gelatin and their luminescent properties and applications,” *Carbon N. Y.*, vol. 60, pp. 421–428, 2013, doi: 10.1016/j.carbon.2013.04.055.

[190] J. Wei, B. Liu, X. Zhang, and C. Song, “One-pot synthesis of N, S co-doped photoluminescent carbon quantum dots for Hg^{2+} ion detection,” *Xinxing Tan Cailiao/New Carbon Mater.*, vol. 33, no. 4, pp. 333–340, 2018, doi: 10.1016/S1872-5805(18)60343-9.

[191] S. Sadjadi, “The utility of carbon dots for photocatalysis,” *Emerging Carbon Materials for Catalysis.*, pp. 123-160, 2021, doi: 10.1016/B978-0-12-817561-3.00004-4.

[192] G. B. Nair and S. J. Dhoble, “Fundamentals of LEDs,” *Fundam. Appl. Light. Diodes*, pp. 35–57, Jan. 2021, doi: 10.1016/B978-0-12-819605-2.00002-1.

[193] P. Saheeda, K. Sabira, J. Joseph, and S. Jayaleksmi, “Green chemistry route to realize, high quantum yield carbon quantum dots for cellular imaging applications,” *Mater. Res. Express*, vol. 6, no. 7, pp. 0–10, 2019, doi: 10.1088/2053-1591/ab1450.

[194] U. Resch-Genger and K. Rurack, “Determination of the photoluminescence quantum yield of dilute dye solutions (IUPAC Technical Report),” *Pure Appl. Chem.*, vol. 85, no. 10, pp. 2005–2026, 2013, doi: 10.1351/PAC-REP-12-03-03.

[195] S. Fery-Forgues and D. Lavabre, “Are fluorescence quantum yields so tricky to measure? A demonstration using familiar stationery products,” *J. Chem. Educ.*, vol. 76, no. 9, pp. 1260–1264, 1999, doi: 10.1021/ed076p1260.

[196] G. A. Crosby and J. N. Demas, “Measurement of photoluminescence quantum yields. Review,” *J. Phys. Chem.*, vol. 75, no. 8, pp. 991–1024, 1971.

[197] L. Zhou, M. Qiao, L. Zhang, L. Sun, Y. Zhang, and W. Liu, “Green and efficient synthesis of carbon quantum dots and their luminescent properties,” *J. Lumin.*, vol. 206, no. June 2018, pp. 158–163, 2019, doi: 10.1016/j.jlumin.2018.10.057.

[198] S. Verma, V. Ravichandiran, and N. Ranjan, “Beyond amyloid proteins: Thioflavin T in nucleic acid recognition,” *Biochimie*, vol. 190, pp. 111–123, 2021, doi: 10.1016/j.biochi.2021.06.003.

[199] Y. Y. Li *et al.*, “Ratiometric fluorescence detection of silver ions using thioflavin T-based organic/inorganic hybrid supraparticles,” *Analyst*, vol. 140, no. 17, pp. 6108–6113, 2015, doi: 10.1039/c5an01146a.

[200] R. B. Cundall, A. K. Davies, P. G. Morris, and J. Williams, “Factors influencing the photosensitizing properties and photoluminescence of thioflavin T,” *J. Photochem.*, vol. 17, no. 2, pp. 369–376, Jan. 1981, doi: 10.1016/0047-2670(81)85379-8.

[201] J. Mohanty, N. Barooah, V. Dhamodharan, S. Harikrishna, P. I. Pradeepkumar, and A. C. Bhasikuttan, “Thioflavin T as an efficient inducer and selective fluorescent sensor for the human telomeric G-quadruplex DNA,” *J. Am. Chem. Soc.*, vol. 135, no. 1, pp. 367–376, 2013, doi: 10.1021/ja309588h.

[202] A. Renaud De La Faverie, A. Gué Din, A. Bedrat, L. A. Yatsunyk, and J.-L. Mergny, “Thioflavin T as a fluorescence light-up probe for G4 formation,” *Nucleic Acids Research*, vol. 42, no. 8, 2014, doi: 10.1093/nar/gku111.

[203] Y.-J. Hu, Y. Liu, L.-X. Zhang, R.-M. Zhao, and S.-S. Qu, “Studies of interaction between colchicine and bovine serum albumin by fluorescence quenching method,” *J. Mol. Struct.*, vol. 750, no. 1–3, pp. 174–178, 2005.

[204] C. W. Lei, M. L. Hsieh, and W. R. Liu, “A facile approach to synthesize carbon quantum dots with pH-dependent properties,” *Dye. Pigment.*, vol. 169, no. May, pp. 73–80, 2019, doi: 10.1016/j.dyepig.2019.05.014.

[205] L. Soleymani and F. Li, “Mechanistic challenges and advantages of biosensor miniaturization into the nanoscale,” *ACS Sensors*, vol. 2, no. 4, pp. 458–467, 2017, doi: 10.1021/acssensors.7b00069.

[206] L. J. Mohammed and K. M. Omer, “Carbon dots as new generation materials for nanothermometer: Review,” *Nanoscale Res. Lett.*, vol. 15, no. 1, 2020, doi: 10.1186/s11671-020-03413-x.

[207] P. Yu, X. Wen, Y. R. Toh, and J. Tang, “Temperature-dependent fluorescence in carbon dots,” *J. Phys. Chem. C*, vol. 116, no. 48, pp. 25552–25557, 2012, doi: 10.1021/jp307308z.

[208] S. Kalytchuk *et al.*, “Carbon dot nanothermometry: Intracellular photoluminescence lifetime thermal sensing,” *ACS Nano*, vol. 11, no. 2, pp. 1432–1442, 2017, doi: 10.1021/acsnano.6b06670.

[209] G. Liu *et al.*, “Facile synthesis of nitrogen and sulfur co-doped carbon dots for multiple sensing capacities: Alkaline fluorescence enhancement effect, temperature sensing, and selective detection of Fe^{3+} ions,” *New J. Chem.*, vol. 42, no. 15, pp. 13147–13156, 2018, doi: 10.1039/c8nj02086h.

[210] R. D. Gray and J. B. Chaires, “Analysis of multidimensional Q-quadruplex melting curves,” *Curr. Protoc. Nucleic Acid Chem.*,no. 45, pp. 1–16, 2011, doi: 10.1002/0471142700.nc1704s45.

[211] Y. Zhang, J. Chen, H. Ju, and J. Zhou, “Thermal denaturation profile: A straightforward signature to characterize parallel G-quadruplexes,” *Biochimie*, vol. 157, pp. 22–25, 2019, doi: 10.1016/j.biochi.2018.10.018.

[212] A. De Rache and J. L. Mergny, “Assessment of selectivity of G-quadruplex ligands via an optimised FRET melting assay,” *Biochimie*, vol. 115, pp. 194–202, 2015, doi: 10.1016/j.biochi.2015.06.002.

[213] J. Jana and K. Weisz, “Thermodynamic stability of G-Quadruplexes: Impact of sequence and environment,” *ChemBioChem*, vol. 22, no. 19, pp. 2848–2856, 2021, doi: 10.1002/cbic.202100127.

[214] Y. Liu, P. Chen, K. Yu, Z. Wu, N. Wang, and X. Yu, “Nitrogen and sulfur co-doped carbon dots: Facile synthesis and multifunctional applications for pH sensing, temperature sensing and RNA-selective imaging,” *Microchem. J.*, vol. 168, no. May, p. 106248, 2021, doi: 10.1016/j.microc.2021.106248.

[215] X. Cui *et al.*, “Dual functional N- and S-co-doped carbon dots as the sensor for temperature and Fe^{3+} ions,” *Sensors Actuators, B Chem.*, vol. 242, pp. 1272–1280, 2017, doi: 10.1016/j.snb.2016.09.032.

[216] Z. Han, H. Zhang, L. He, S. Pan, H. Liu, and X. Hu, “One-pot hydrothermal synthesis of nitrogen and sulfur co-doped carbon dots and their application for sensitive detection of curcumin and temperature,” *Microchem. J.*, vol. 146, no. January, pp. 300–308, 2019, doi: 10.1016/j.microc.2019.01.024.

[217] Y. Hu, J. Yang, L. Jia, and J. S. Yu, “Ethanol in aqueous hydrogen peroxide solution: Hydrothermal synthesis of highly photoluminescent carbon dots as multifunctional nanosensors,” *Carbon N. Y.*, vol. 93, pp. 999–1007, 2015, doi: 10.1016/j.carbon.2015.06.018.

[218] S. Xu *et al.*, “Thioflavin T as an efficient fluorescence sensor for selective recognition of RNA G-quadruplexes OPEN,” *Nat. Publ. Gr.*, 2016, doi: 10.1038/srep24793.

[219] P. Hanczyc, P. Rajchel-Mieldzioć, M. B. Feng, and P. Fita, “Identification of thioflavin T binding modes to DNA: A structure-specific molecular probe for lasing applications,” *J. Phys. Chem. Lett. 2021*, vol. 12, p. 5442, 2021, doi: 10.1021/acs.jpclett.1c01254.

[220] Y. Xu and H. Sugiyama, “Formation of the G-quadruplex and i-motif structures in retinoblastoma susceptibility genes (Rb),” doi: 10.1093/nar/gkj485.

[221] X. Cui, H. Chen, Q. Zhang, M. Xu, G. Yuan, and J. Zhou, “Exploration of the structure and recognition of a G-quadruplex in the her2 proto-oncogene promoter and its transcriptional regulation,” *Sci. Rep.*, vol. 9, no. 1, pp. 1–12, 2019.

[222] E. Bilgen and Ö. Persil Çetinkol, “Doxorubicin exhibits strong and selective association with VEGF Pu22 G-quadruplex,” *Biochim. Biophys. Acta - Gen. Subj.*, vol. 1864, no. 12, p. 129720, 2020, doi: 10.1016/j.bbagen.2020.129720.

[223] J. Dai, M. Carver, L. H. Hurley, and D. Yang, “Solution structure of a 2:1 quindoline-c-MYC G-quadruplex: Insights into G-quadruplex-interactive small molecule drug design,” *J. Am. Chem. Soc.*, vol. 133, no. 44, pp. 17673–17680, 2011, doi: 10.1021/ja205646q.

[224] V. H. Le, N. Nagesh, and E. A. Lewis, “Bcl-2 promoter sequence G-Quadruplex interactions with three planar and non-planar cationic porphyrins: TMPyP4, TMPyP3, and TMPyP2,” *PLoS One*, vol. 8, no. 8, p. 72462, 2013, doi: 10.1371/journal.pone.0072462.

[225] J. Jana *et al.*, “Chelerythrine down regulates expression of VEGFA, BCL2 and KRAS by arresting G-Quadruplex structures at their promoter regions OPEN,” *Nat. Publ. Gr.*, 2016, doi: 10.1038/srep40706.

[226] R. del Villar-Guerra, R. D. Gray, and J. B. Chaires, “Quadruplex DNA structure characterization by circular dichroism,” *Curr. Protoc. nucleic acid Chem.*, vol. 68, pp. 17–18, 2017.

[227] R. del Villar-Guerra, J. O. Trent, and J. B. Chaires, “G-Quadruplex secondary structure obtained from circular dichroism spectroscopy,” *Angew. Chemie*, vol. 130, no. 24, pp. 7289–7293, 2018, doi: 10.1002/ange.201709184.

APPENDICES

A. Preparation of Buffer and Stock Solutions

0.100 M Standard Sample (Quinine Sulfate) Preparation

Quinine sulfate in solid form was dissolved in 0.100 M H_2SO_4 solution. Quinine sulfate solution was prepared at a random concentration was prepared as follows:

First, for the preparation of 0.100 M H_2SO_4 solution the steps specified below were followed:

%96 H_2SO_4 = 10.00 x 96.00 x d (g/mL) / molecular weight (g/mol)

H_2SO_4, Molecular Weight (MW): 98.07 g/mol Density: 1.835 g/mL

%96 H_2SO_4 = 10.00 x 96.00 x 1.835 g/mL / 98.07 g/mL = 17.96 M

Concentration was rearranged by using the following equation:

$M_1 \times V_1 = M_2 \times V_2$

0.100 M x 100.0 mL = 17.96 M x V_2 V_2 = 0.560 mL

V_2 was completed to 100.0 mL with Millipore water for preparation of 0.100 M H_2SO_4.

Second, a known amount of Quinine sulfate powder was dissolved in the prepared H_2SO_4 solution to prepare the stock solution and the other samples with absorbance values between 0.02 and 0.10 at maximum wavelength (350 nm) were prepared by serial dilution of the stock solution.

2.5 ppm, 5.0 ppm, and 10.0 ppm 50.0 mL N,S-CQDs Preparation

2.5 ppm, 5.0 ppm, and 10.0 ppm N,S-CQDs solutions were prepared from 50.0 ppm stock solution of N,S-CQDs.

50.0 ppm 50.0 mL N,S-CQDs preparation:

ppm = mg/L

50.0 ppm = 50.0 mg/ 1L = 0.00250 g/ 50.0 mL

0.00250 g solid N,S-CQDs was dissolved in 50.0 mL Millipore water.

Concentrations were rearranged by using the following equation:

$M_1 \times V_1 = M_2 \times V_2$

For 2.5 ppm: 50.0 ppm x V_1 = 2.5 ppm x 50.0 mL and V_1 = 2.5 mL

For 5.0 ppm : 50.0 ppm x V_1 = 5.0 ppm x 50.0 mL and V_1 = 5.0 mL

For 10.0 ppm : 50.0 ppm x V_1 = 10.0 ppm x 50.0 mL and V_1 = 10.0 mL

V_1 values were completed to 50.0 mL with Millipore water for the preparation of 2.5 ppm, 5.0 ppm, and 10.0 ppm N,S-CQDs.

5.0×10^2 μM, 1.0×10^3 μM, and 4.0×10^3 μM ThT Preparation

5.0×10^2 μM, 1.0×10^3 μM, and 4.0×10^3 μM ThT solutions prepared from 5.0×10^3 μM 5.0 mL ThT stock solution.

ThT, Molecular Weight (MW) : 318.86 g/mol

n (mol) = M (molarity) x V (volume)

n (mol) = 5.0×10^{-3} M x 5.0×10^{-3} L = 2.5×10^{-5} mol

2.50×10^{-5} mol ThT = m (g) / 318.86 g/mol so; m (g) = 7.97×10^{-3} g

7.97×10^{-3} g ThT was dissolved in 5.0 mL Millipore water for the preparation of 5.0×10^3 μM ThT solution.

Concentrations were rearranged by using the following equation:

$M_1 \times V_1 = M_2 \times V_2$

For 5.0×10^2 μM: 5.0×10^3 μM x $V_1 = 5.0 \times 10^2$ μM x 5.0 mL and $V_1 = 0.5$ mL

For 1.0×10^3 μM: 5.0×10^3 μM x $V_1 = 1.0 \times 10^3$ μM x 5.0 mL and $V_1 = 1.0$ mL

For 4.0×10^3 μM: 5.0×10^3 μM x $V_1 = 4.0 \times 10^3$ μM x 5.0 mL and $V_1 = 4.0$ mL

The total volumes of above solutions were completed to 5.0 mL with Millipore water.

100.0 mM K-Phosphate Buffer Preparation for Fluorometry Experiments:

1.0 M, 0.500 L K_2HPO_4 Stock Preparation:

K_2HPO_4 Molecular Weight (MW): 174.18 g/mol and n (mol) = m (g) / MW(g/mol)

n (mol) = M (molarity) x V (volume)

n (mol) = 1.000 M x 0.500 L = 0.500 mol

0.500 mol K_2HPO_4 = m (g) / 174.18 g/mol so; m (g) = 87.09 g

87.09 g K_2HPO_4 was dissolved in 500.00 mL Millipore water for preparation of 1.00 M K_2HPO_4 solution.

1.0 M, 0.500 L KH_2PO_4 Stock Preparation:

KH_2PO_4 Molecular Weight (MW): 136.09 g/mol and n (mol) = m (g) / MW(g/mol)

n (mol) = M (molarity) x V (volume)

n (mol) = 1.000 M x 0.500 L = 0.500 mol

0.500 mol KH_2PO_4 = m (g) / 136.09 g/mol so; m (g) = 68.05 g

68.05 g KH_2PO_4 was dissolved in 500.00 mL Millipore water for preparation of 1.00 M KH_2PO_4 solution.

100.0 mM K-Phosphate Buffer Preparation:

Concentrations were rearranged by using the following equation:

$M_1 \times V_1 = M_2 \times V_2$

For K_2HPO_4 : 1.000 M x V_1 = 0.6150 M x 1.000 L and V_1 = 61.50 mL

For KH_2PO_4 : 1.000 M x V_1 = 0.3850 M x 1.000 L and V_1 = 38.50 mL

The above solutions were mixed and total volume was completed to 1.0 L with Millipore water. With 1.0 M NaOH solution, the pH of the buffer was adjusted to 7.0.

500.0 mM 100.0 mL KCl Solution Preparation for Fluorometry Experiments:

n (mol) = M (molarity) x V (volume)

n (mol) = 0.500 M x 0.100 L = 0.050 mol

0.050 mol KCl = m (g) / 74.55 g/mol so; m (g) = 3.730 g

3.730 g KCl was dissolved in 100.0 mL Millipore water for preparation of 500.0 mM KCl solution.

B. DLS Experimet Analysis Report

Analysis Results					
d(0)	1.51 nm / 3.15 nm	**d(5)**	3.07 nm / 67.1 nm	**number of Peaks 3**	
d(10)	4.14 nm/ 109 nm	**d(25)**	5.40 nm/ 176 nm	6.35 nm	113 nm
d(50)	6.22 nm / 2.07 μm	**d(75)**	8.66 nm / 5.24 μm	4.09 μm	
d(90)	10.5 nm / 5.30 μm	**d(95)**	12.8 nm / 8.55 μm		
d(100)	209 nm / 17.7 μm				

Table 4. Particle size analysis results for the synthesized N,S-CQDs. “d” represents particle distribution %.

C. Quantum Yield Experiments

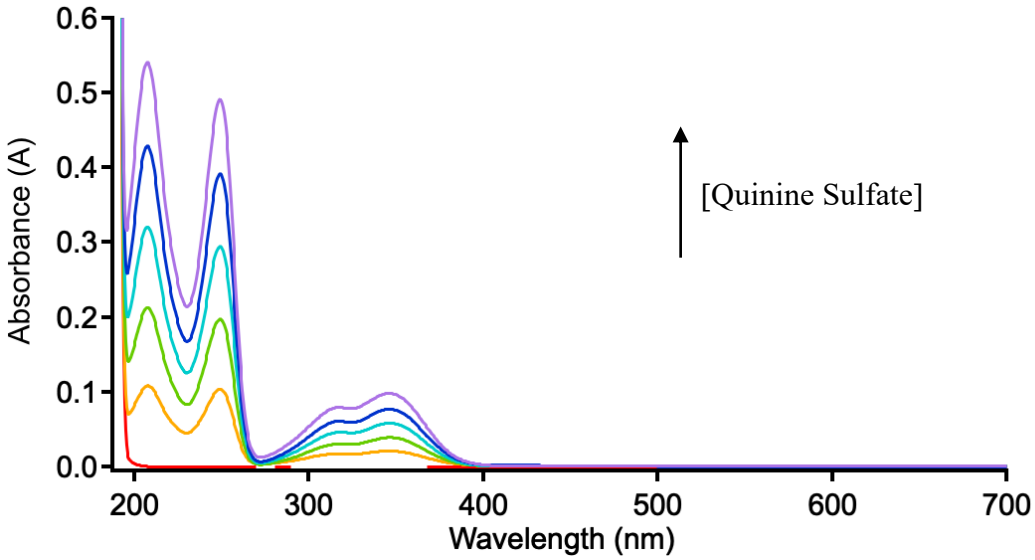

Figure 25. Absorbance spectra of standard sample (quinine sulfate) at different concentrations (Absorbance values: 0.00, 0.02, 0.04, 0.06, 0.08 and 0.10) at 350 nm.

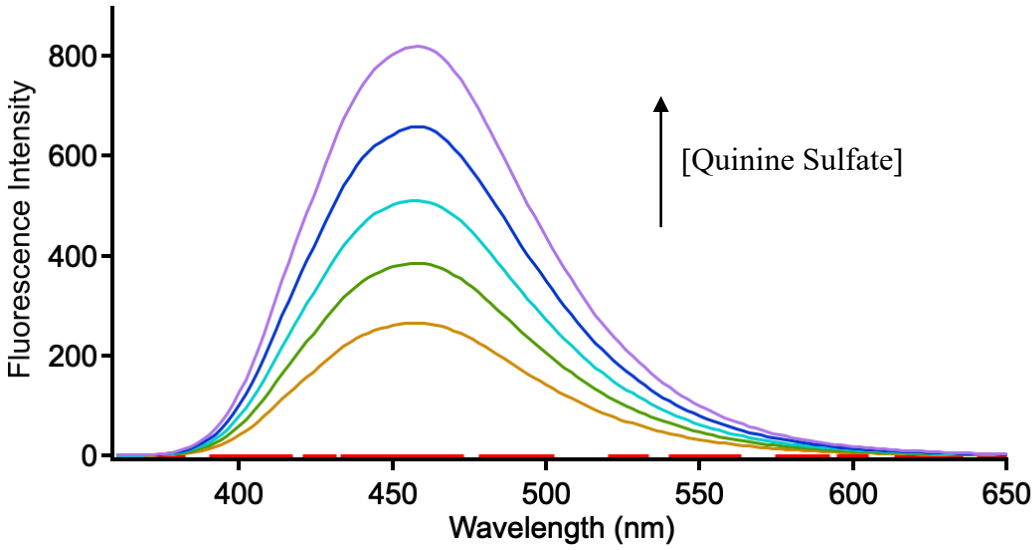

Figure 26. Fluorescence spectra of standard sample (quinine sulfate) at different concentrations (Absorbance values: 0.00, 0.02, 0.04, 0.06, 0.08 and 0.10) for quantum yield calculation.

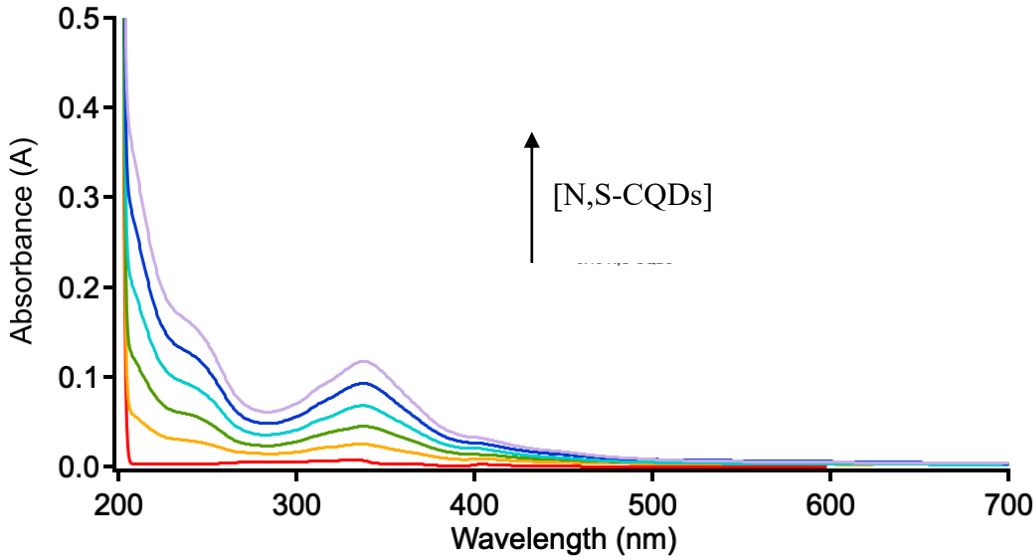

Figure 27. Absorbance spectra of N,S-CQDs at different concentrations (Absorbance values: 0.00, 0.02, 0.04, 0.06, 0.08 and 0.10) at 350 nm

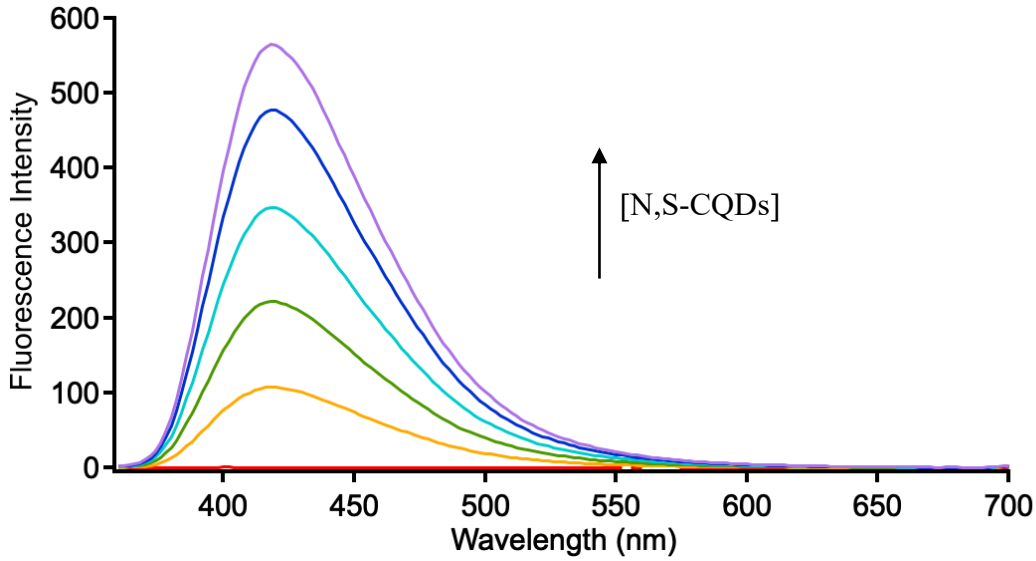

Figure 28. Fluorescence spectra of N,S-CQDs at different concentrations (Absorbance values: 0.00, 0.02, 0.04, 0.06, 0.08 and 0.10) for quantum yield calculation.

D. Fluorometry Experiments

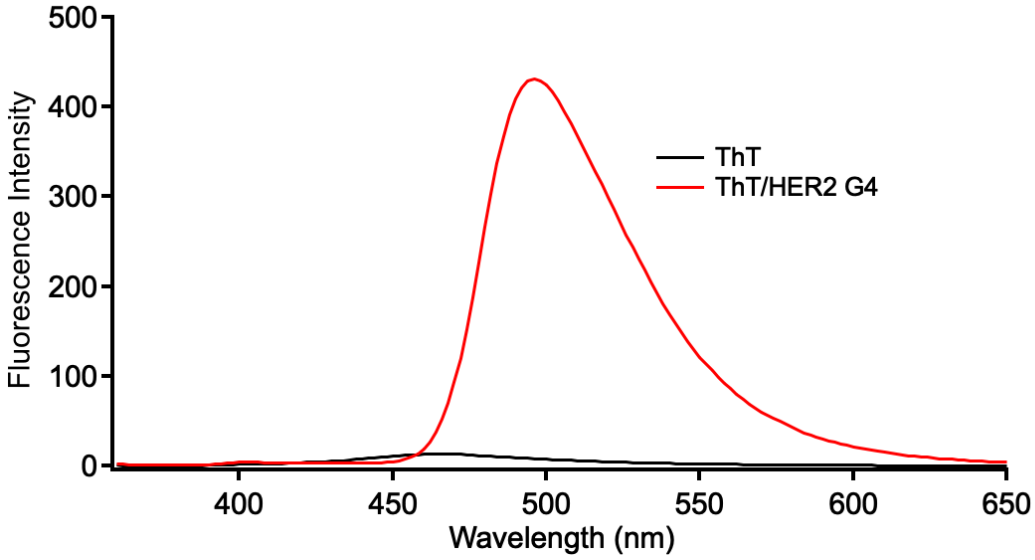

Figure 29. Fluorescence spectra of N,S-CQDs/ThT in the absence (final concentration 40.98 μM) and the presence of HER2 G4 (final concentration 7.38μM).

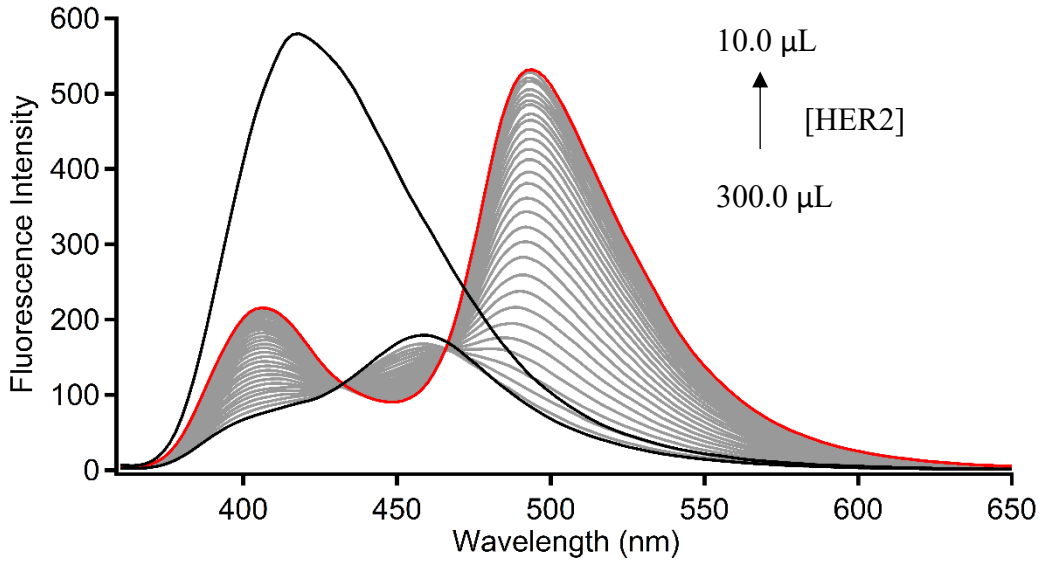

Figure 30. Fluorescence spectra of 2.5 ppm N,S-CQDs/ThT (final concentration 40.98 µM) probe upon the addition of different volumes (10.0 – 300.0 µL) of HER2 G4 stock solution (75 µM).

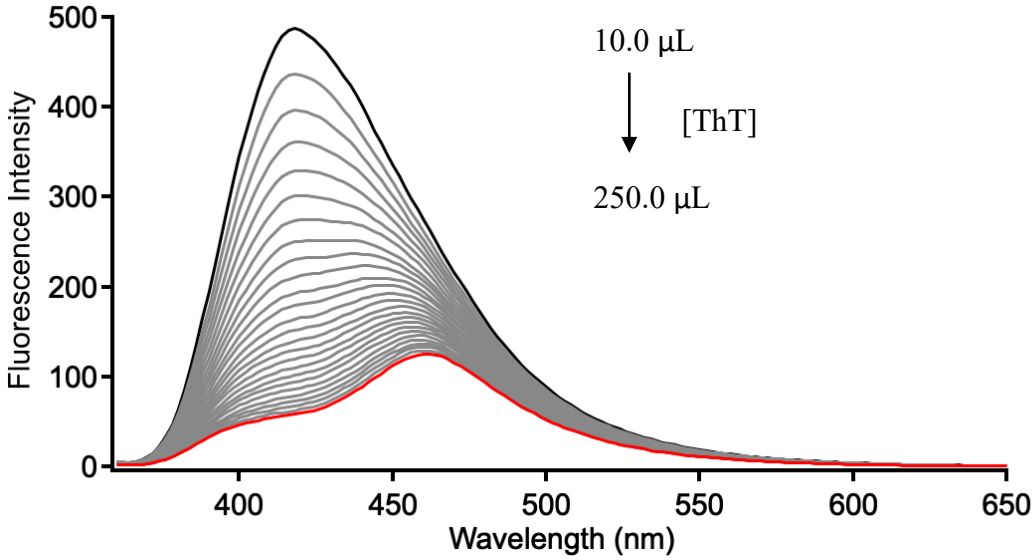

Figure 31. Fluorescence spectra of 2.5 ppm N,S-CQDs titrated with increasing volumes (10.0 – 250.0 µL) of $5.0x10^2$ µM ThT solution (1^{st} replication).

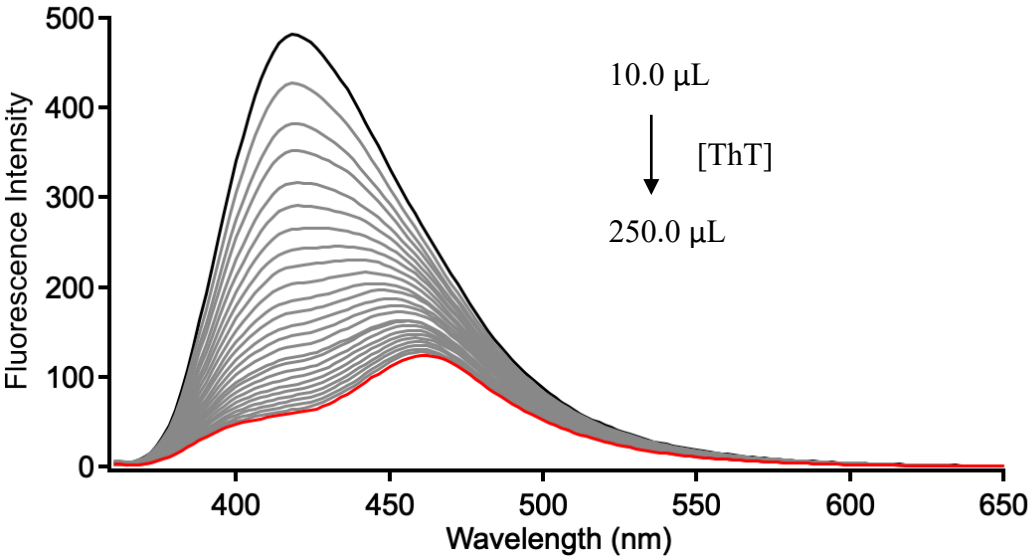

Figure 32. Fluorescence spectra of 2.5 ppm N,S-CQDs titrated with increasing volumes (10.0 – 250.0 µL) of 5.0x10^2 µM ThT solution (2nd replication).

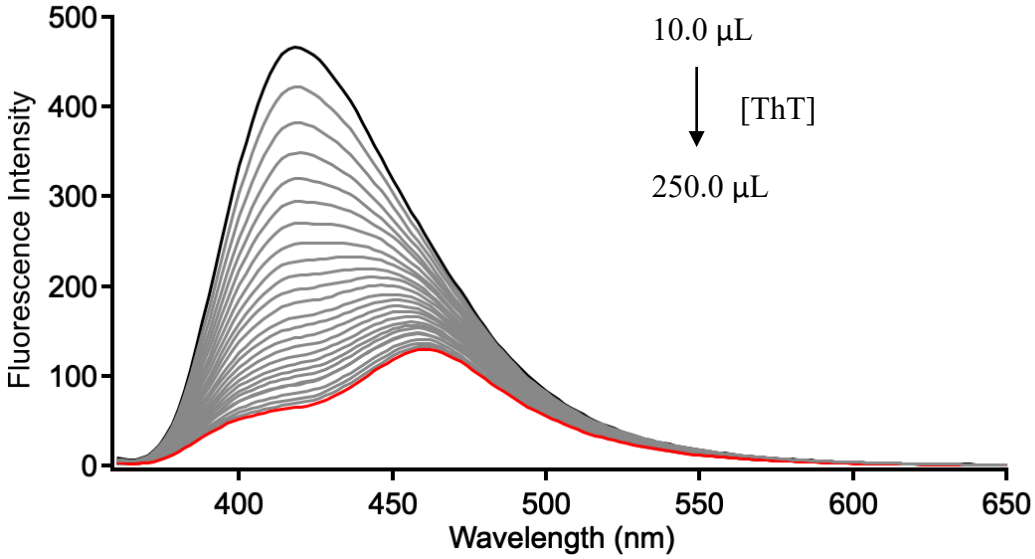

Figure 33. Fluorescence spectra of 2.5 ppm N,S-CQDs titrated with increasing volumes (10.0 – 250.0 µL) of 5.0x10^2 µM ThT solution (3rd replication).

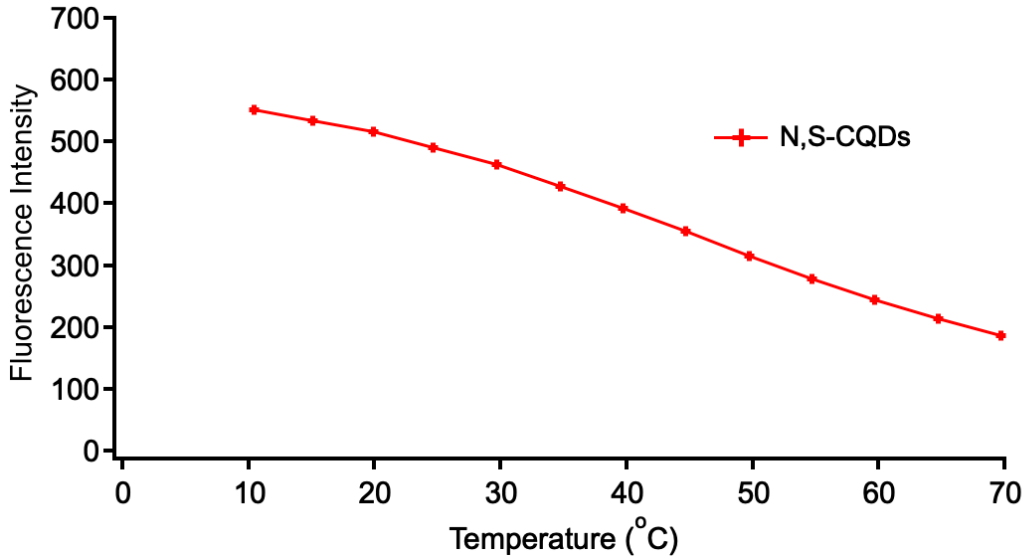

Figure 34. Fluorescence Intensity vs. Temperature (°C) graph of N,S-CQDs (2.5 ppm), at the emission wavelength of 406 nm.

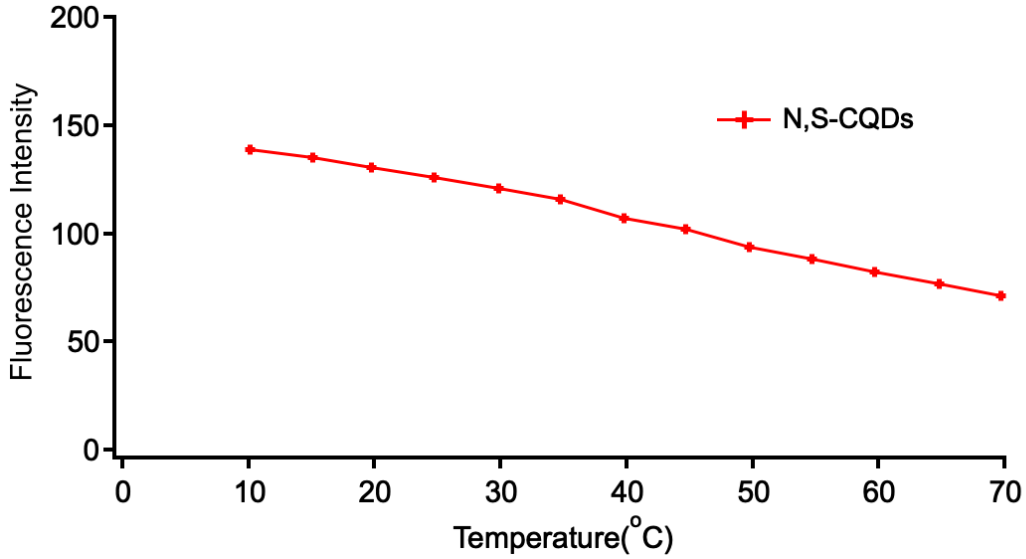

Figure 35. Fluorescence Intensity vs Temperature (°C) graph of N,S-CQDs (2.5 ppm), at the emission wavelength of 494 nm.